ALMA MATER STUDIORUM — UNIVERSITÀ DI BOLOGNA

SCUOLA DI SCIENZE
Corso di Laurea Magistrale in Astrofisica e Cosmologia
Dipartimento di Fisica e Astronomia

A Study of Extended Radio Galaxies in the Shapley Concentration Core

Tesi di Laurea Magistrale

Candidato:
Gabriella Di Gennaro

Relatore:
Chiar.mo Prof.
Daniele Dallacasa
Correlatore:
Dr.ssa Tiziana Venturi

Sessione III
Anno Accademico 2014-2015

This Thesis work was done as part of the research activity of the Osservatorio di Radioastronomia - Istituto Nazionale di Astrofisica (INAF) in Bologna.

“Failure
is always the best way to learn.”

Kings of Convenience

Abstract

Extended cluster radio galaxies show different morphologies compared to those found isolated in the field. Indeed, symmetric double radio galaxies are only a small percentage of the total content of radio loud cluster galaxies, which show mainly tailed morphologies (e.g. O'Dea & Owen, 1985). Moreover, cluster mergers can deeply affect the statistical properties of their radio activity.

In order to better understand the morphological and radio activity differences of the radio galaxies in major mergeing and non/tidal-merging clusters, we performed a multifrequency study of extended radio galaxies inside two cluster complexes, A3528 and A3558. They belong to the innermost region of the Shapley Concentration, the most massive concentration of galaxy clusters (termed *supercluster*) in the local Universe, at average redshift $z \approx 0.043$.

We analysed low frequency radio data performed at 235 and 610 MHz with Giant Metrewave Radio Telescope (GMRT) and we combined them with proprietary and literature observations, in order to have a wide frequency range (150 MHz to 8.4 GHz) to perform the spectral analysis. The low frequency images allowed us to carry out a detailed study of the radio tails and diffuse emission found in some cases.

The results in the radio band were also qualitatively compared with the X-ray information coming from XMM-Newton observations, in order to test the interaction between radio galaxies and cluster weather.

We found that the brightest central galaxies (BCGs) in the A3528 cluster complex are powerful and present substantial emission from old relativistic plasma characterized by a steep spectrum ($\alpha > 2$). In the light of observational pieces of evidence, we suggest they are possible re-started radio galaxies. On the other hand, the tailed radio galaxies trace the host galaxy motion with respect to the ICM, and our findings is consistent with the dynamical interpretation of a tidal interaction (Gastaldello et al. 2003). On the contrary, the BCGs in the A3558 cluster complex are either quiet or very faint radio galaxies, supporting the hypothesis that clusters mergers quench the radio emission from AGN.

This thesis work is organised as follows:

- in **chapter 1** an overview on the galaxy clusters is presented. We briefly introduce the current theory of cluster formation and then we focus on the description of their emission mechanisms, in the X-ray and in the radio band. The typical cluster radio sources are also presented;
- in **chapter 2** the Shapley Concentration Supercluster is introduced. We give an overview on the literature framework in the optical, X-ray and radio band of the two cluster complexes discussed in the present work, A3528 and A3558;
- in **chapter 3** the method used for the analysis of the GMRT data is discussed and the radio images of the two cluster complexes are shown;
- in **chapter 4** the sample of extended radio galaxies is described. We present a detailed discussion of their radio images at both low and high frequencies, producing a proper morphological calssification of each object;
- in **chapter 5** the spectral study of the radio galaxies is performed and their physical parameters are determined;
- in **chapter 6** we discuss the results of the spectral and morphological analysis. We compare the two cluster complexes, and suggest a possible explanation for the observed differences. Finally, an overview on the near future work on this project is outlined.

Throughout the present thesis a cosmology with $\mathrm{H_0} = 70$ km $\mathrm{s^{-1}}$ $\mathrm{Mpc^{-1}}$, $\Omega_\mathrm{m} = 0.3$ and $\Omega_\Lambda = 0.7$ is assumed.

Sommario

Le radio galassie estese all'interno degli ammassi di galassie mostrano morfologie diverse rispetto a quelle che si trovano isolate. Infatti negli ammassi, le radio galassie doppie e simmetriche rappresentano solo una piccola percentuale del contenuto totale, mentre è molto più frequente vedere radio galassie caratterizzate da code (O'Dea & Owen, 1985). Inoltre, le interazioni tra ammassi di galassie possono avere effetto sulle proprietà statistiche dell'attività in banda radio di questi stessi oggetti.

Per comprendere meglio le differenze morfologiche e di emissione in banda radio delle radio galassie all'interno di ammassi che hanno o meno subito un'interazione (frontale o mareale), è stato effettuato uno studio in multi-frequenza su radio galassie estese all'interno di due complessi di ammassi, A3528 e A3558. Questi complessi si trovono nelle regioni centrali della Concentrazione di Shapley, la più massiva concentrazione di ammassi di galassie (chiamato *superammasso*) nell'Universo locale, ad un redshift medio di $z \approx 0.043$.

Sono stati analizzati dati radio a 235 e 610 MHz ottenuti con il Giant Metrewave Radio Telescope (GMRT), i quali sono stati combinati con osservazioni di letteratura al fine di avere un ampio intervallo di frequenza (150 MHz to 8.4 GHz) per effettuare l'analisi spettrale. Le immagini a bassa frequenza hanno permesso un studio approfondito delle code delle radio galassie e dell'emissione diffusa osservata in alcuni casi.

I risultati ottenuti in banda radio sono stati confrontati in modo qualitativo con le infromazioni in banda X provenienti da osservazioni effettuate con XMM-Newton, in modo da studiare le interazioni tra le radio galassie e l'ambiente in cui esse si trovano.

Abbiamo trovato che le galassie centrali più brillanti (chiamate BCG, *bright central galaxy*) del complesso A3528 sono potenti in banda radio e hanno un contributo sostanziale da parte di emissione da plasma relativistico diffuso e vecchio, caratterizzato da uno spettro ripido ($\alpha > 2$). Dalle evidenze osservative, suggeriamo che queste possano essere radio galassie che hanno riattivato la loro emissione radio. D'altra parte, le radio galassie caratterizzate da code tracciano il moto delle galassie rispetto al mezzo intra-cluster, e i nostri risultati sono consistenti con l'interpretazione dinamica di un'interazione mareale (Gastaldello et al.

2003). Al contrario, le BCG nel complesso A3558 sono quiescienti o molto deboli in banda radio, e supportano l'ipotesi che le interazioni tra ammassi di galassie possano smorzare l'emissione radio degli AGN.

Questa tesi è così strutturata:

- nel **capitolo 1** viene presentata una panoramica sugli ammassi di galassie. Introduciamo brevemente le attuali teorie sulla loro formazione e ci concentriamo sui meccanismi con cui gli ammassi di galassie emettono, sia in bada radio che in banda X. Sono inoltre presentati anche i tipici oggetti radio che si trovano negli ammassi;
- nel **capitolo 2** viene introdotta la Concentrazione di Shapley. Viene fornita una panoramica sulle conoscenze in banda ottica, X e radio dei due complessi di ammassi studiati in questo lavoro, A3528 e A3558;
- nel **capitolo 3** viene discusso il metodo di riduzione e di analisi dei dati GMRT e vengono mostrate le immagini dei due complessi;
- nel **capitolo 4** viene descritto il campione di radio galassie estese studiato. Presentiamo una dettagliata discussione sulla loro morfologia a bassa ed ad alta frequenza e, in base a questa, forniamo una classificazione delle radio galassie;
- nel **capitolo 5** viene effettuato lo studio spettrale delle radio galassie e vengono determinati i parametri fisici che le caratterizzano;
- nel **capitolo 6** vengono discussi i risultati dell'analisi spettrale e morfologica. Confrontiamo i due complessi di ammassi e viene suggerita una possibile spiegazione per le differenze osservate. Infine, viene fornita una panoramica sul lavoro che verrà fatto immediatamente dopo questo lavoro di tesi.

Durante questa tesi, è stata utilizzata la seguente cosmologia: $\mathrm{H}_0 = 70$ km s^{-1} Mpc^{-1}, $\Omega_\mathrm{m} = 0.3$ and $\Omega_\Lambda = 0.7$

CONTENTS

CHAPTER 1

THE LARGE SCALE STRUCTURES

The most massive and largest structures in the local Universe are the superclusters, namely huge regions with a high concentration of clusters and groups of galaxies. Due to their very large size, these structures are not in a common potential well, but in the innermost regions merging phenomena and frequent interactions between clusters are taking place, thanks to the very dense environments. For this reason, the supercluster cores are the perfect regions to observe and to study a significant number of galaxies that are undergoing dynamical interaction for the first time.

1.1 The bottom-up scenario

According to recent theories on the evolution of the Universe, structure formation is thought to be a consequence of a hierarchical growth from density fluctuations produced by the cosmic inflation. Such variations are detected as temperature anisotropies of the order of $\frac{\delta T}{T} \approx 10^{-5}$ in the cosmic microwave background (CMB), mapping the surface of last scattering between matter and radiation. Today we observe very large structures, hence such fluctuations must have evolved with the cosmic time. Since the overdense regions have stronger gravitational potential than the general cosmic background density after the decoupling between matter and radiation, the fluctuations grow without the contrast of the radiation pressure, attracting the surrounding material and thus increasing the overdensity. Such gravitational instability proceeds until it causes the collapse to gravitationally bound objects.

Nowadays, it is assumed that the matter is formed by two constituents: the

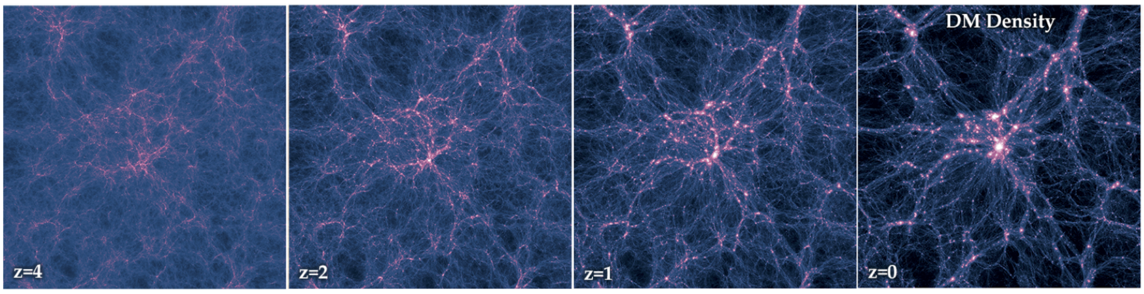

Figure 1.1: Numerical simulation of the dark matter distribution in the Universe with the ΛCDM cosmology. The brighter colours represent the higher density values while the black regions are the voids (credits: http://www.illustris-project.org).

baryonic component connected with the luminous matter, and the dark component, almost unknown because of the collisionless nature of its particles, whose existence is inferred only from its gravitational effects. Since it is collisionless and does not interact with the radiation, the dark matter oscillations are the first that grow up, forming the potential wells that will lead to the subsequent baryonic fluctuations growth. Although it is still unknown which kind of particles is the main consituent of the dark matter, the most accepted model of hierarchical clustering involves the non thermalized cold dark matter (CDM). According to the CDM the earliest structures were the smallest ones, characterized by masses of $10^5 \div 10^6$ $\mathrm{M}_\odot$, while the larger ones were built up in a second time, through merger phenomena. Such hierarchical clustering is called *bottom-up scenario*. Nowadays, the standard CDM model is improved with the introduction of the cosmological constant Λ, generating the ΛCDM model[1].

Since the larger the structures the higher the overdensities and hence the non-linearity, the only way to investigate the hierarchical clustering is via N-body simulations. They show that the mass accretion takes place along dense filaments (or sheets) and, on the large scale, the Universe has a large fraction of voids (figure 1.1).

The bottom-up scenario predicts that the large structures are formed only after the matter collapse into the potential well produced by the (cold) dark matter. Such hypothesis is confirmed by the fact that we do not observe galaxy clusters at very high redshift. Hence, it has been assumed that galaxy clusters form within filaments, or sheets, and move towards high density caustics, where they may merge and form the so-called superclusters, i.e. large concentration of galaxy clusters.

---

[1] In the ΛCDM cosmology $\Omega_\Lambda = 0.7$ and $\Omega_\mathrm{m} = 0.3$, where Ω_Λ and Ω_m are the density contrast of the cosmologic constant and of the matter, respectively.

Cluster mergers are the most energetic phenomena in the Universe. The kinetic energy released as a consequence of the merging depends on the mass of the clusters and on their relative velocity, and can reach the value of $10^{63} \div 10^{64}$ erg. However, it is still unkown how such energy is dissipated and which are the consequences on the environment and on the cluster members.

Mergers can be broadly classified into three groups:

- *major mergers*, where the colliding objects have almost equal masses and high impact factor. In this type of merger both objects are distrupted before they relax into a single big structure;
- *minor mergers*, where the colliding objects have different masses. During such processes, the smallest object is accreted onto the more massive one, which undergoes small changes;
- *tidal mergers*, where the colliding objects interact only mildly.

Despite our poor understanding of cluster mergers, correlations between observational quantities are found (section 1.3). Such correlations are probably related to a portion of the kinetic energy of the cluster merger which is converted into thermal energy and produces turbolence and heating by shock waves. Moreover, when the shock wave propagates into the medium, the magnetic field in the intracluster medium (ICM) is compressed and hence synchrotron non-thermal emission is enhanced (section 1.4.2). Finally, radio galaxies in clusters mergers have distorted morphologies (section 1.4.1).

1.2 Galaxy clusters

Clusters of galaxies are typically formed by hundreds of galaxies spread over a volume of the order of few Mpc^3. They are the most massive gravitationally bound structures in the Universe. In order to verify this last statement, we have to compare the Hubble time t_{H}, that is an indication of the age of the Universe, and the crossing time t_{cr}, i.e. the time that an object inside the cluster needs to cross the whole structure: in particular, to guarantee a dynamically relaxed structure it must be $t_{\mathrm{cr}} \ll t_{\mathrm{H}}$. The crossing time is expressed by the relation

$$t_{\mathrm{cr}} = \frac{R}{v} \approx 10^9 \frac{R}{1\mathrm{Mpc}} \left(\frac{\sigma}{1000 \text{ km s}^{-1}} \right)^{-1} \quad \mathrm{yr} \; , \tag{1.1}$$

where the cluster virial radius R and the velocity dispersion of the galaxy σ are normalized to the typical values for the galaxy cluster. Thus, $t_{\rm cr}$ is approximaly about 1 Gyr that is remarkably smaller than the Hubble time ($t_{\rm H} \approx 13.7$ Gyr). It means that a cluster had enough time to dinamically relax. It is clear that if the radius increases even of an order of magnitude, like in cluster concentrations, the two quantities become comparable and thus nothing about the dynamical state can be inferred.

Despite their large number in a cluster, galaxies represent only about 5% of the cluster mass and the smallest part of the baryon content ($f_{\rm baryons} \approx$10-15%). The main constituent of the cluster mass is indeed the dark matter ($f_{\rm DM} \approx$80-90%).

1.2.1 Abell classification

In the old days (up to the mid '50ies) the classification of galaxy clusters was particularly problematic: few were discovered on the basis of galaxy overdensities, and the definitions of the cluster center and cluster radius were rather uncertain. Moreover, another very important problem was the identification of the galaxies actually belonging to the cluster. The former issue was mainly solved by the survey made with the National Geographic Society-Palomar Observatory Sky Survey, which showed that galaxy clusters were far more numerous than previously thought.

The first classification of galaxy clusters was performed by Abell (1958) through the discovery of 2712 clusters in the northern sky[2], based on their richness, a parameter related to the numbers of galaxies in a cluster. His criteria, nearly indipendent of distance, were the following:

1. the cluster contains at least 50 galaxies in the magnitude range of m_3 and $m_3 + 2$, where m_3 is the magnitude of the third brightest galaxy;
2. the cluster radius is estimated by $R_{\rm A} = \frac{1.7}{z}$ arcmin, that corresponds to 3 $\rm h_{50}^{-1}$ Mpc, where $\rm h_{50}$ represents the normalization of the Hubble constant at 50 km $\rm s^{-1}$ $\rm Mpc^{-1}$;
3. the cluster redshift is in the range of $0.02 \leq z \leq 0.2$.

He defined five classes of richness, summarized in table 1.1, where the richness class 0 represents those galaxy clusters that do not satisfy the first criterium.

---

[2] In a second time the same analysis was made also for the clusters in the southern sky (Abell, Corwin & Olowin, 1989).

Richness class	# galaxies	# clusters
0	30-49	>1000
1	50-79	1224
2	80-129	383
3	130-199	68
4	200- 299	6
5	300>	1

Table 1.1: Abell richness classification; the lower limit of the richness 0 class is due to the fact that it is not a complete sample.

Abell (1965, 1975) classified the clusters also on the basis of their morphology, which can be divided into regluar and irregular. The former seem to have highly symmetric shape and a high concentration of galaxies in their center, while the latter have little symmetry and often show significant subclustering. These properties could be explained by considering a deep physical difference between the two types of galaxy clusters: the regular ones are classified as dinamically relaxed systems, while the irregular ones are possibly still in forming. Later, an intermediate morphological class was added.

The Abell catalogue is the most famous and used classification of galaxy clusters. However, other authors suggested different classification systems. Zwicky et al. (1961 and 1968) proposed richness criteria based on the determination of the surface density contours and the identification of the magnitude of the first brightest galaxy. This classification is much less strict than the Abell one, and as a result the Zwicky catalogue contains a huge fraction of poor clusters which are not included into the Abell catalogue. The same authors provided a morphological classification based on the galaxy concentration in the central region of the clusters, defining it as compact, medium compact, or open. In a quite similar way, Bautz & Morgan (1970) provided a cluster classification based on the morphology of the central galaxy, depending on whether the clusters are dominated by a central dominant (cD) galaxy (type I), by a galaxy that is intermediate between cD and normal giant elliptical (type II) or whether there is no a dominating cluster galaxy (type III).

Property	Regular	Intermediate	Irregular
Zwicky type	compact	medium-compact	open
Bautz-Morgan type	I, I-II, II	II, II-III	II-III, III
Galactic content	elliptical rich	spiral poor	spiral rich
Symetry	sherical	intermediate	irregular
Central concentration	high	moderate	low
Subclustering	absent	moderate	significant
Richness	rich	rich-moderate	rich-poor

Table 1.2: Properties of morphological classes of clusters with respect to the Abell classification.

1.3 X-ray emission from galaxy clusters

The first discovery of X-ray emission form galaxy clusters was made in the middle 1960s from the nearest and rich clusters, i.e. Virgo, Perseus and Coma (e.g. Byram et al. 1966, Fritz et al. 1971 and Meekins et al. 1971, respectively). Subsequent observations through the Uhuru satellite highlighted that the X-ray emission from galaxy cluster was not uncommon, and that it spreads over the whole size of the galaxy distribution in the clusters. The observed luminosities were very high ($L_{\mathrm{X}} \approx 10^{43 \div 45}$ erg s^{-1}), an order of magnitude larger than those of quasars. Moreover, galaxy clusters did not show evidence for low-energy photoabsorption, typical of emission from discrete sources, neither variable X-ray emission.

1.3.1 The intracluster medium

Although several emission mechanism were proposed, the lack of low-energy photoabsorpions in the X-ray spectra of galaxy clusters indicates that it is associated with thermal emission from a diffuse, ionized plasma, i.e. the intracluster medium (ICM). This gas represent approximately the 75% of the baryonic content and is characterized by a very high temperature, in the range of $T_{\mathrm{gas}} \approx 2 \times 10^7 \div 2 \times 10^8$ K, and by very low density, which is in the range $n_{\mathrm{e}} \approx 10^{-3} \div 10^{-4}$ cm^{-3}. At these high temperatures the matter is fully ionized and electrons and ions interact through their electric fields. Such interactions decelerate the electrons, causing the emission of X-ray photons, similar to a free-free scattering. This process is known as thermal Bremsstrahlung, where “thermal” is referred to the velocity distribution of electrons. The Bremsstrahlung emissivity, espressed in erg cm^{-3} s^{-1} Hz^{-1}, is given by:

$$\varepsilon_\nu \propto Z^2 n_\mathrm{e} n_\mathrm{Z} g_\mathrm{ff}(T_\mathrm{gas},\nu) T_\mathrm{gas}^{-1/2} e^{-\frac{h\nu}{k_\mathrm{B}T_\mathrm{gas}}} \tag{1.2}$$

where $g_\mathrm{ff}(T_\mathrm{gas},\nu)$ is the Gaunt factor that is of the order of the unity, Z is the charge of the ions, and h and k_B are the Planck and the Boltzmann constants[3], respectively. Hence, we expect to see a flat spectrum for $h\nu \ll k_\mathrm{B}T_\mathrm{gas}$ and an exponential decreese for $h\nu \gtrsim k_\mathrm{B}T_\mathrm{gas}$, that allows the accurate measurement of the temperature. The thermal Bremsstrahlung radiation has continuous spectrum. Moreover, the X-ray spectra are characterized by emission lines from highly ionized elements (figure 1.2). The higher the cluster temperature, the weaker the emission lines. The most prominent emission lines are due to the highly ionized metals, like Fe, C, O, S and Si. The measure of the equivalent width (EW[4]) of these lines provides the mean value of the iron abundance, equal to a third of the solar value for almost all clusters. Due to the very high gas metallicity, the origin of ICM is not cosmological, but it is likely that the primoridal gas is processed by galactic winds, supernovae explosion and AGN feedback.

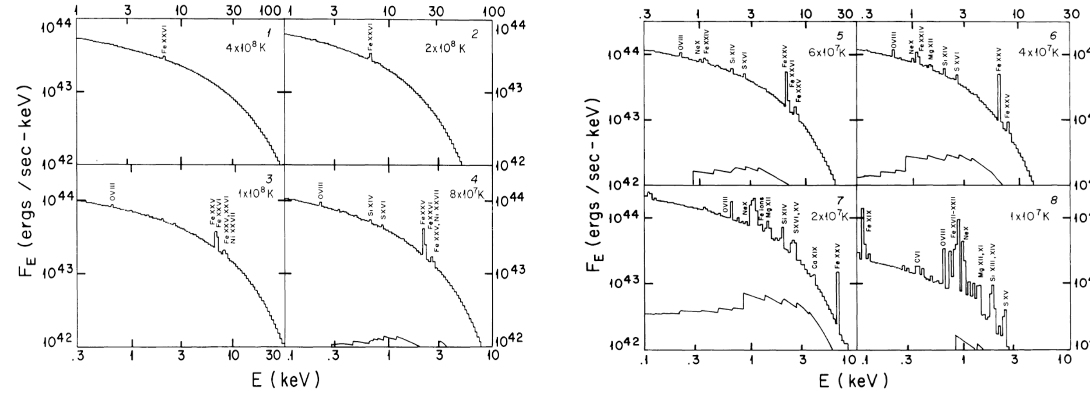

Figure 1.2: X-ray spectra of galaxy clusters from the highest temperature (left panel, top left) to the lowest one (right panel, bottom right) (Sararazin & Bahcall, 1977).

How the plasma is distributed is another important question. Cavaliere & Fusco-Femiano (1976, 1978) assumed that both gas and galaxies are in hydrostatic equilibrium in the potential well. This means that the sound-crossing time $t_\mathrm{sc} = \frac{2R_\mathrm{A}}{c_\mathrm{s}}$ must be much less than the lifetime of the galaxy cluster. It is verified since $t_\mathrm{sc} \approx 7 \times 10^8$ yr while $t_\mathrm{cl} \approx t_\mathrm{H}$. They also assumed a constant temperature for the whole system, and an isotropic velocity dispersion. From this analysis, they found a fitting formula

---

[3] $h \approx 6.63 \times 10^{-27}$ erg s while $k_\mathrm{B} \approx 1.38 \times 10^{-16}$ erg K^{-1}.

[4] EW$=\int \frac{I_\nu - I_\mathrm{c}}{I_\mathrm{c}} d\lambda$ gives an indication of the line strenght respect to the continuum I_c.

for the density profile that in most cases well describes the observed data, which is referred to as the β-model:

$$\rho_{\rm gas}(r) = \rho_{\rm gas,0}\left[1+\left(\frac{r}{r_{\rm c}}\right)^2\right]^{-\frac{3}{2}\beta} \tag{1.3}$$

where $\rho_{\rm gas,0}$ is the central value of the gas density and r_c is the core radius, i.e. a measure of the cluster core. The fit parameter $\beta = \frac{\mu m_{\rm p}\sigma^2}{k_{\rm B}T_{\rm gas}}$ is the ratio between the dynamical temperature, expressed by the velocity dispersion σ, and the gas temperature. It can be estimated from both the fit on equation 1.3 and its definition, obtaining $\beta_{\rm fit} \approx 0.65$ and $\beta_{\rm spec} \approx 1.2$, respectively. The fact that two different methods give two values for β, the so-called β-discrepancy, is still unresolved and it is probably due to the assumptions of the model, in particular the isothermal one. Better density profiles are given with a more complicated models (e.g. Vikhlinin et al. 2006) but they require a larger number of parameters.

The assumption of the isothermal ICM could be tested only in late '90s, after the launch of ASCA and Beppo-Sax satellites, when spatially resolved temperature measurements became observable. In earlier days only the global temperature value was available. The new X-ray satellites showed that the central region of some clusters is characterized by a temperature decrease. Initially this property led to the development of the so-called cooling flow model (e.g. Fabian & Nulsen, 1977), where the low temperature in the cluster centers was explained by the presence of dense gas that hydrodinamically cools in a short time (the cooling time is $t_{\rm cool} \propto n_{\rm e}^{-1}T^{-1/2}$) and is compressed by the overlying gas to preserve the pressure equilibrium. However, some pieces of evidence, such as the absence of recombination lines, the star formation rate lower than expected and the lower limit to the temperature (the so-called cooling flow problem) dismissed the simple cooling flow model in favour of a cooling model plus a heating source. For this reason the nomenclature was changed to cool-core (CC) clusters (figure 1.3). It is interesting to note that since the CC clusters have smaller cooling time in the central regions, they are associated to dynamically relaxed systems.

A possible explanation for the cooling flow problem is the heating provided by the active galactic nucleus (AGN) feedback from the central dominant cluster galaxy. This phenomenon indeed releases enough energy ($E \approx 10^{62}$ erg) to contrast the gas flowing into the central regions, without destroying the cool-core. However, how this feedback exactly works is still unknown. It is also seen that the central AGN can deeply affect the ICM, producing distorted X-ray emission or depressions, the

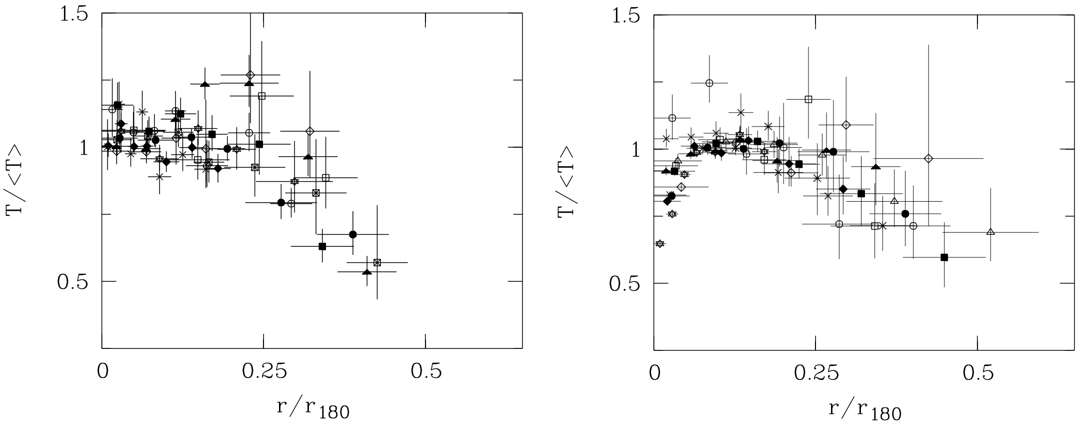

Figure 1.3: Temperature profiles (projected) for the non cool-core clusters (left panel) and the cool-core clusters (right panel), plotted against radii in unit of r_{180} (De Grandi & Molendi, 2002).

so-called cavities. X-ray cavities are present in almost 70% of cool-core clusters, even if this fraction could be a lower limit due to their difficult detectability (McNamara & Nulsen 2007, and Gitti, Brighenti & McNamara 2012, for reviews).

1.4 Radio emission from galaxy clusters

The radio emission is non-thermal and originates by the motion of ultrarelativistic electrons in magnetic fields, which produce the so-called synchrotron radiation. The radio emission in galaxy clusters may come from individual galaxies, typically in the form of AGN activity (1.4.1), or it may be associated with the ICM (section 1.4.2).

Given an ultra-relativistic particle with mass m and charge q into a magnetized medium $\vec{H}$, generally assumed constant, according to the Lorentz equation

$$\frac{d\vec{p}}{dt} = \frac{q}{c}\vec{v} \times \vec{H} \,, \tag{1.4}$$

the particle experiences a circular motion perpendicular to the magnetic field while it moves with constant velocity in the direction of the field lines. The resulting motion is elicoidal and the particle is affected by a centripetal acceleration that correspond to an emitting power equal to:

$$W = \frac{2}{3}\frac{q^4}{m^2c^3}\gamma^2 H^2 \tag{1.5}$$

by the Larmor equation. The parameter $\gamma = \left[1 - \left(\frac{v}{c}\right)^2\right]^{-1/2}$ is the Lorentz factor which is $\gg 1$ for an ultra-relativistic particle. From equation 1.5 it is clear that the electrons are the main responsible of the synchrotron emission: since $m_{\rm e} \ll m_{\rm p}$ and the emitting power depends on the inverse of the mass, the proton mass is negligible in the equation 1.5. Moreover, since $v \approx c$, the emitting power has not a classic dipole shape but half of the radiation is emitted within a cone of $\approx 1/\gamma$ width. Hence the synchrotron radiation from a single electron is impulsive and also nearly monochromatic, since its spectrum, i.e. the Fourier Transform of the received impulse, has a maximum for $\nu_{\rm m} = \nu_{\rm s}/3$, where $\nu_{\rm s\ GHz} \approx 4.2 \times 10^{-9}\gamma^2 H_{\mu{\rm G}}$ is the critical frequency linked to the impulse period.

The astrophysical events never involve a single electron but rather a population of relativistic electrons. Hence, in the absence of collective processes and/or absorption effects, i.e. the medium is optically thin, the synchrotron spectrum from a ultra-relativistic plasma is simply the superimposition of the contributions from the various electrons. If we assume an energy distribution for the electrons as $N(E) = N_0 E^{-\delta}$, as it is observed for the cosmic rays, the synchrotron specific emission, i.e. the monochromatic power per unit of volume per unit of frequency, is:

$$\varepsilon_\nu \propto N_0 H^{\frac{\delta+1}{2}} \nu^{-\frac{\delta-1}{2}} \propto N_0 H^{\alpha+1} \nu^{-\alpha}\,, \tag{1.6}$$

This is a power-law distribution, where $\alpha = \frac{\delta-1}{2}$ is the spectral index that only depends on the initial energy distribution of the electrons.

The typical synchrotron spectrum (top right panel in figure 1.4) may deviate from a single power law at low and high frequencies. In the bottom panel in figure 1.4, at low frequencies the spectrum increases with the frequency as $\nu^{5/2}$ since the radiation is absorbed by the synchrotron electrons themselves, i.e. the medium is optically thick. Hence, it is observed only in compact source. This phenomenon is known as synchotron self-absorption.

At the other end of the spectrum (at high frequencies) the synchrotron spectrum becomes steeper (top right panel) because of the radiative losses that are more important at high electron energies. The time of the last acceleration of particles is a measure of the source lifetime, and can be estimated by the break frequency $\nu_{\rm br}$, i.e. the frequency where the power law is broken and the steepening is observed:

$$t_{\rm br} \approx 1.65 \times 10^9 \left(\frac{H}{\mu{\rm G}}\right)^{-3/2} \left(\frac{\nu_{\rm br}}{\rm GHz}\right)^{-1/2} \quad {\rm yr}\,. \tag{1.7}$$

Another important characteristic of the synchrotron radiation is that it is polar-

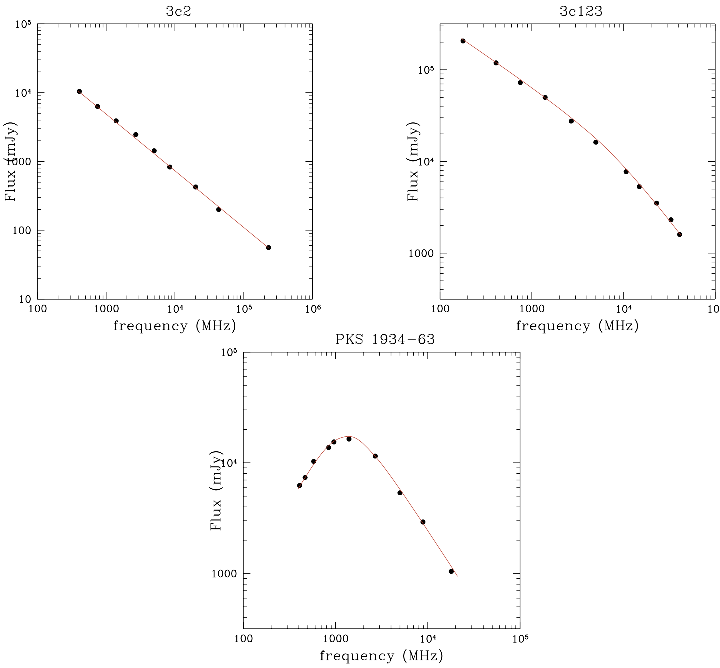

Figure 1.4: *Top panel, left*: typical synchrotron spectrum with $\alpha \approx 0.8$. *Top panel, right*: synchrotron spectrum characterized by radiative losses, with a steepening at high frequencies. *Bottom panel*: inverted shape of the synchrotron spectrum at short frequencies due to self-absorption.

ized and its strength is the best way to constrain the ordered magnetic field value of the radio source.

1.4.1 Discrete emission: radio galaxies

The first sources discovered emitting via synchrotron radiation are the radio galaxies. They can be either compact or extended structures, and their sizes spread over many orders of magnitude, from few pc to Mpc. Unlike the diffuse radio sources that will be described in the next section, they have an optical counterparter, which is usually an elliptical galaxy with a supermassive black hole $M_{\mathrm{BH}} \approx 10^7 \div 10^9$ $\mathrm{M}_\odot$ in the center.

Radio galaxies belong to a sub-class of the active galactic nuclei (AGNs), the radio loud AGN characterized by a ratio between the radio flux at 5 GHz and the optical B band flux ≥ 10 (Kellerman et al. 1989). The reason why this class of AGN has a very strong radio emission, in contrast to the radio quiet AGN, is still debated. Recently Chiaberge et al. (2015) proposed a scenario in which the radio emissivity is turned on by major BH merging events.

Fanaroff & Riley (1974) classified two types of radio galaxies on the basis of their radio power: the Fanaroff-Riley type I (FRI), which are characterized by a radio power of $P_{1.4\ \mathrm{GHz}} \lesssim 10^{24.5}$ Watt HZ^{-1}, and the Fanaroff-Riley type II (FRII), with $P_{1.4\ \mathrm{GHz}} \gtrsim 10^{24.5}$ Watt HZ^{-1}. This separation reflects a different morphology (figure 1.5). The main components of a radio galaxy can be summarized as following:

- *core*: compact region which hosts the central engine of the radio source (the SMBH) and coincident with the nuclear region in the optical host galaxy. Its linear size is $< 1 \div 100$ pc, and by definition it represent the turning point where the jets become optically thin and therefore its position is frequency dependent. Its overall radio spectrum is generally flat ($\alpha \approx 0$).
- *jets*: collimated structures with a continuous or a knotty morphology that transport radiation, particles and magnetic fields from the central SMBH to the outer parts of the radio galaxy. They are explained by the model of continuous production of relativistic plasma by the SMBH and their typical spectral index is $\alpha \approx 0.7$;
- *hot spots*: roughly spherical structures with diameter of the order of the kpc. They originate as a consequence of the interaction between the jets and the external medium that produce a strong shock wave, where the relativistic plasma coming from the nucleus and transported by the jets is re-accelerated. Hence their emission is bright, with luminosity that can be a high fraction of the total luminosity. They are located at the edge of the whole structure. The spectral index of the hot spots is about $\alpha \approx 0.5$, typical of a young population of particles;
- *lobes*: extended structures, generally approximated to ellipses, with low surface brightness but with a substantial contribution to the total luminosity. Their size can spread from tens of pc (compact sources) to few Mpc (giant radio galaxies). Their spectrum is steeper than the hot spots ($\alpha \gtrsim 1$), hence they contain the oldest population of electrons.

FRI radio galaxies do not show either hot spots or well-defined lobes. The most luminous components of this class of radio galaxies are indeed the jets, which appear morphologically continuous, symmetric and less collimated than in FRII (the so-called plumes), and the core. Hence, they are also called edge darkened radio galaxies. On the contrary, FRII radio galaxies show all the components described previously. In general, the hot spots are the brightest regions, the lobes are well approximated to ellipses, and the jets and the core are less dominant. Due to their morphology, they are also called edge brightened sources. Since the more luminous the jets the higher the radiative losses, the radiative transport in FRII radio galaxies is more efficient. Two examples of FRI and FRII radio galaxies are shown in figure 1.5.

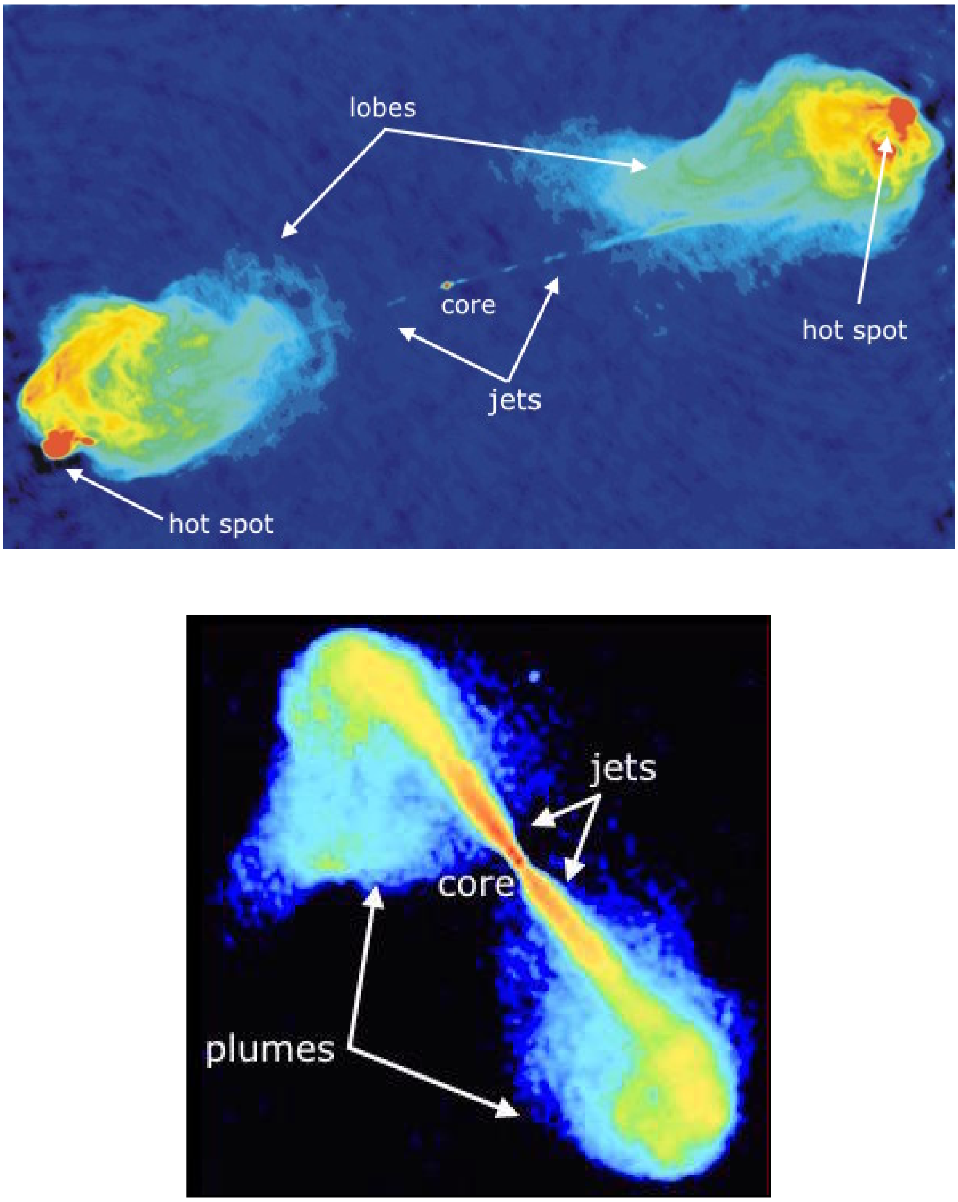

Figure 1.5: VLA image in false colour of a typical FRII radio galaxy, Cygnus A (top) and of a typical FRI radio galaxy, 3C 296 (bottom); the different components of the two types of morphologies are pointed out.

Tailed radio galaxies

The symmetric morphologies described above, the so-called double galaxies, are typical of isolated radio galaxies. In galaxy clusters, only $\approx 30\%$ of the extended radio galaxies (FRI and FRII) keep their symmetry, while the majority typically show distorted morohologies (e.g. O'Dea & Owen, 1985). Their classification varies from wide-angle tails (WATs) to narrow-angle tails (NATs) to head-tail sources (HTs), depending on the angle φ between the two jet. Generally, WATs have $\varphi \geq 10°$, while the dichotomy between NAT and HT sources is more problematic and probably depends on both the jet projection and angular resolution. The three types of tailed radio galaxies are shown in figure 1.6 and are classified as distorted FRI or FRI/FRII sources.

At the beginning of their discovery, such peculiar morphologies were thought to be due to the interaction between these radio galaxies respect with the dense ICM. In fact, the NATs are never associated with the dominat cluster galaxy, nearly at rest in the bottom of the potential well. On the contrary, they are in rapid motion in the gravitational potential of the cluster. The ram pressure of the gas could hence be able to affect the typical radio galaxy morphology, bending the jets from the lobes down to a very small angle (e.g. Miley et al. 1972, Miley 1980), up to 90° from their original orientation. More recently, it has been found that the host galaxies of NATs do not have, on average, velocities higher than the other cluster radio galaxies, in contrast to the ram pressure scenario. Therefore, Bliton et al. (1998) proposed that a combination of galaxy velocity and cluster–subcluster mergers could be a possible explanation to this peculiar morphology.

In contrast to NATs, WAT sources are characterized by larger angles between tails, and are often asymmetric in shape (e.g. 3C 465, bottom panel in figure 1.6). Moreover, they are usually associated with the dominant galaxy located at the center of the cluster. Hence, they are generally moving very slowly ($v < 100$ km s^{-1}), with velocities that are not high enough to justify their shape by simple ram pressure. It has been thought that a combination of bulk motion of the ICM as consquence of cluters mergers and accretion could be at least partly responsable for the observed morphologies (Burns 1998).

Since WATs and NATs are found only in galaxy clusters, they can be used as traces to select galaxy clusters in radio surveys, as it has been succesfully done in a number of cases (e.g. Giacintucci & Venturi 2009, Mao et al. 2010).

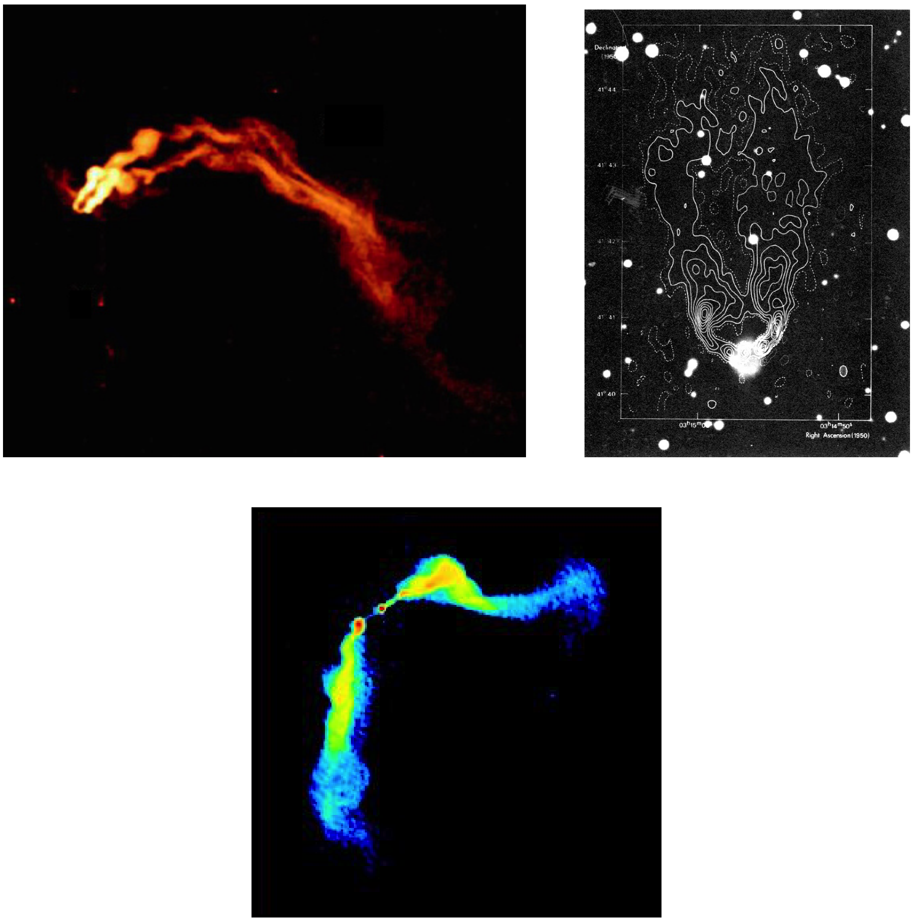

Figure 1.6: Examples of tailed radio galaxies. *Top panel, left*: 330 MHz VLA image of 3C 129, an head-tail radio galaxy (Lane et al. 2002). *Top panel, right*: 5 GHz contours superimposed on the optical image of NGC 1256, a narrow-angle tail radio galaxy (Wellington et al. 1973). *Bottom*: 1.4 GHz VLA image of 3C 465, a wide-angle tail (Eilek, Burns, O'Dea & Owen 1984)

1.4.2 Diffuse emission: halos, relics and mini-halos

After the discovery of a diffuse giant halo at the center of the Coma cluster (Large et al. 1959) many other diffuse radio sources emitting via synchrotron radiation with no optical counterparter were found. They are the best evidence of the presence of magnetic fields spread over very large volumes within galaxy clusters. Such cluster-scale structures are characterized by very steep spectrum and very low surface brightness, and are classified based on their size and location inside the galaxy cluster, into three different categories: halos, relics and mini-halos (figure 1.7).

Halos

Radio halos are large diffuse sources ($R \gtrsim 1$ Mpc) located at the center of galaxy clusters. They have a fairly regular morphology, low polarization percentage and by a surface brightness of $\approx 1-0.1\ \mu$Jy arcsec^{-2} at 1.4 GHz. Their size and morphology usually show a good correlation with the X-ray emission of the underlying ICM. The spectral studies of these sources are challenging, mainly due to the difficulties in their detection at $\nu > 1.4$ GHz, and in the subtraction of the contribution of the embedded individual radio sources. Despite these issues, their spectral index is always $\gtrsim 1$, that is a typical value of aged radio sources. Since the radiative lifetime is too short to allow the particle diffusion throughout the cluster volume (the so-called slow diffusion problem), it is thought that the emitting electrons must be re-accelerated locally, probably by merging events. As a matter of fact, primary re-acceleration models based on the idea of merger induced turbolence in the ICM (e.g. Brunetti et al. 2001; Brunetti & Jones 2014 for review) are now supported by observational evidence. In particular Cassano et al. (2010) found that all halo clusters have been affected by merging events, while Brunetti et al. (2009) found a different behaviour of the radio power and X-ray luminosity correlation between radio halo and non radio halo clusters that supports the clusters different evolutionary state.

Relics

Relics are diffuse radio sources with linear size, spectral index and surface brightness similar to those of halos but, in contrast to them, they are characterized by high polarization percentage and they are located in peripherical cluster regions. Furthermore, unlike radio halos, they exhibit a variety of different morphologies, the most common being elongated and roundish structures. The former are the classical relics with little substructures, located roughly perpendicularly to the cluster radius. Their formation models suggest that they are related to outgoing shock waves produced during cluster mergers, in good agreement with their location, shape and polarization properties. Some theories involve the possibility that the relativistic electrons come from old AGN radio lobes that are no longer visible because of the radiative losses, and that are re-started by a shock wave (e.g. Randall et a., 2010). Another theory has been proposed by Mathews & Brighenti (2008) who stressed the possibility that the radio bubbles, that are thought to produce also the radio cavities at cluster center, could rise to the cluster periphery and be impacted by cosmic rays, producing synchrotron emission. In addition to the different formation

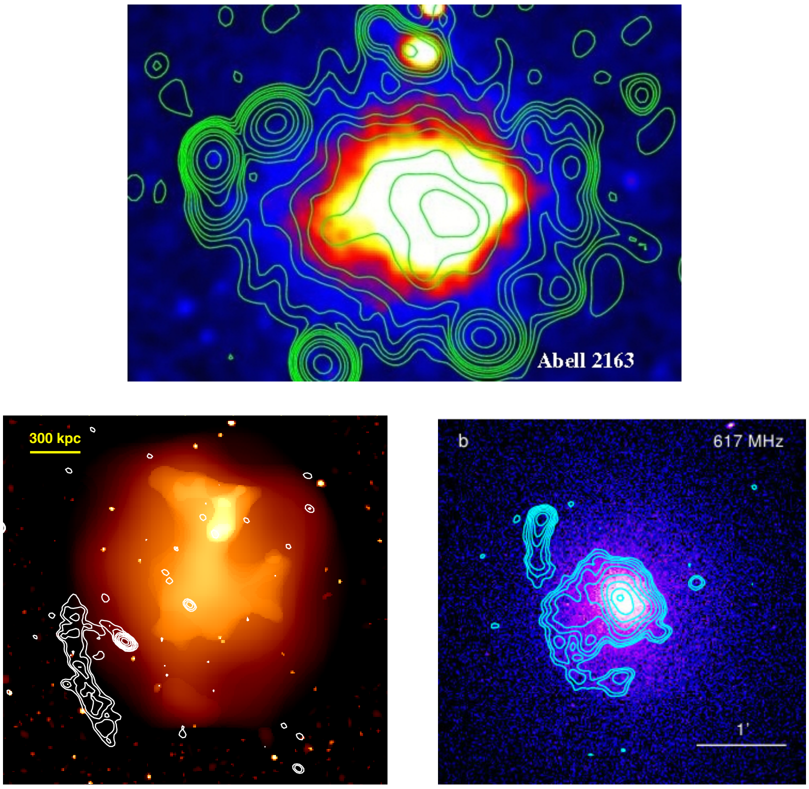

Figure 1.7: Examples of the three classes of diffuse radio sources in galaxy clusters. Radio contours (green, white and cyan) are superimposed on the X-ray image (clolours). *Top panel*: radio halo in A2163 (Feretti et al. 2001). *Bottom panel, left*: relic in A521 (Giacintucci et al. 2008). *Bottom panel, right*: mini-halo in RXC J1720.1+2638 (Giacintucci et al. 2014).

theories, roundish relics are also closer to the cluster center, smaller in linear size and steeper in spectral index than elongated ones. A correlation between the relic radio power at 1.4 GHz and the cluster X-ray luminosity was found, regardless the different morphologies (Feretti et al. 2012). Such correlation has a similar behaviour of that found for the radio halos and it supports the suggestion that both relics and halos trace cluster mergers.

Mini-halos

Mini-halos are diffuse radio sources that extend on a scale of the order of hundreds kpc. Their surface brightness is similar to that of relics and halos but, unlike them, they are found only in cool-core clusters. The origin of the radio emission is still unclear, but one possibility is that it is due to the re-acceleration of the relativistic particles by magnetohydrodynamic (MHD) turbulence, with the addition of the gas compression due to the cooling flow (Gitti et al. 2002). Cassano et al. (2008) found that the synchrotron emissivity of mini-halos is of a factor ≈ 50 higher than that of radio halos, which could be explained if the central AGN provides a continuous injection of electrons.

More recently, Mazzotta & Giacintucci (2008) pointed out the correlation between the size of mini-halos and the presence of cold fronts in the inner cluster regions, and suggest that sloshing motion of the ICM could be a source of re-acceleration for the radiating electrons.

CHAPTER 2

THE SHAPLEY CONCENTRATION

The Shapley Concentration is the richest nearby supercluster and it is located in the Southern sky. It lies behind the Hydra-Centaurus supercluster and it includes a number of galaxy clusters higher than the other big concentration near the Local Group, the Great Attractor. The redshift of the whole structure is in the range of $0.033 \lesssim z \lesssim 0.06$ (Quintana et al. 1995, 1997), corresponding to a distance of 30 $\mathrm{h}^{-1} \div$ 200 h^{-1} Mpc. It is considered the most massive concentration of galaxy clusters in the local Universe.

2.1 Historical background

The Shapley Concentration was discovered in 1930 by Harlow Shapley (Shapley 1930) who noted a large concentration of galaxies, which he called "cloud", in the Centaurus constellation. He identified the center of this cloud at $\alpha_{\mathrm{J1900}} = 13^{\mathrm{h}}23^{\mathrm{m}}06^{\mathrm{s}}$ and $\delta_{\mathrm{J1900}} = -31^{\mathrm{d}}01^{\mathrm{m}}00^{\mathrm{s}}$, and its extensions roughly 2.8° by 0.8° for an area of about 2.2 square degrees. Comparing this cloud with the Coma-Virgo one, he discovered that the former was about ten times as crowded, and that its members were 5.7 magnitudes fainter. From this analysis he discovered also that such cloud should have a distance of approximately 45 Mpc. Thus the linear size of the structure should be 2.2×0.6 Mpc, about three times bigger that the Coma-Virgo cloud.

Only later, through deeper studies on the distribution of the galaxy clusters in the concentration (Scaramella et al. 1989, and Vettolani et al. 1990), on the distribution of the optical galaxies (Raychaudhury 1989) and on the density excess with respect to the field (Zucca et al. 1993), it became clear that the cloud observed by Shapley was only the innermost part of the whole concentration. It was discovered that the true dimension of the concentration spread over $\approx$ 300 square degrees and that it is located at a distance ranging from 30 h^{-1} to 200 h^{-1} Mpc, toward the Centaurus region.

The denser region of the supercluster is located at a distance of about 140 h^{-1} Mpc and, according to Zucca et al. (1993), it is dominated by three cluster complexes: A3558-A3556-A3562 in the inner core, A3528-A3530-A3532 westwards and A3571-A3572-A3575 eastwards, in a volume of $32 \times 55 \times 100$ h^{-1} Mpc^3, approximately. These condensations at low density contrast ($f \geq 2$, where f is the ratio between the local and the mean cluster density) are connected through a large cloud of clusters of radius of 25 h^{-1} Mpc, reaching a total number of 25 members. However, it is still visible increasing the density contrast to $f \geq 100$ (which correspond to a radius of 6 h^{-1} Mpc). In addition to the high density of galaxies in the optical, the center of the Shapley Supercluster is also exceptional in X-ray band, containing six very bright clusters of the sky (Edge et al. 1990). Moreover, Raychaudhurry et al. (1991) found a large number of X-ray multiple clusters. The estimate of the mass of the structure is problematic. Ettori et al. (1997) calculated it as sum of each cluster masses and found a gravitational mass of about $M \approx 3.5 \div 8.5 \times 10^{15}$ $M_\odot$ inside a scale of 50 Mpc and $M > 10^{16}$ $M_\odot$ for larger scales, by estrapolation. Hence, they argued that the structures are bound in the inner region of the supercluster, while they are still in formation in the the outermost one.

All these pieces of evidence stress the possibility that the innermost region of the Shapley Concentration is dynamically active and that is the perfect place to investigate cluster evolution and cluster-cluster mergers.

2.1.1 The Shapley Concentration as cosmological tool

Due to its relatively small distance from the Local Group, the Shapley Concentration was initially studied in order to verify its possible influence on thepeculiar velocity of the Local Group with respect to the cosmic microwave background (CMB). The first study in this sense was made by Melnick & Moles (1987), but their conclusion was that the mass of the Shapley Concentration was smaller at least by one order of magnitude than that required to match this effect. A few years later, Scaramella et al. (1991) pointed out that the Shapley Concentration could be responsable for $\approx 30\%$ of the perturbation of the Hubble flow, together with the Great Attractor. Accordingly, Raychaudhury et al. (1991) and Plionis & Valdardini (1991) suggested

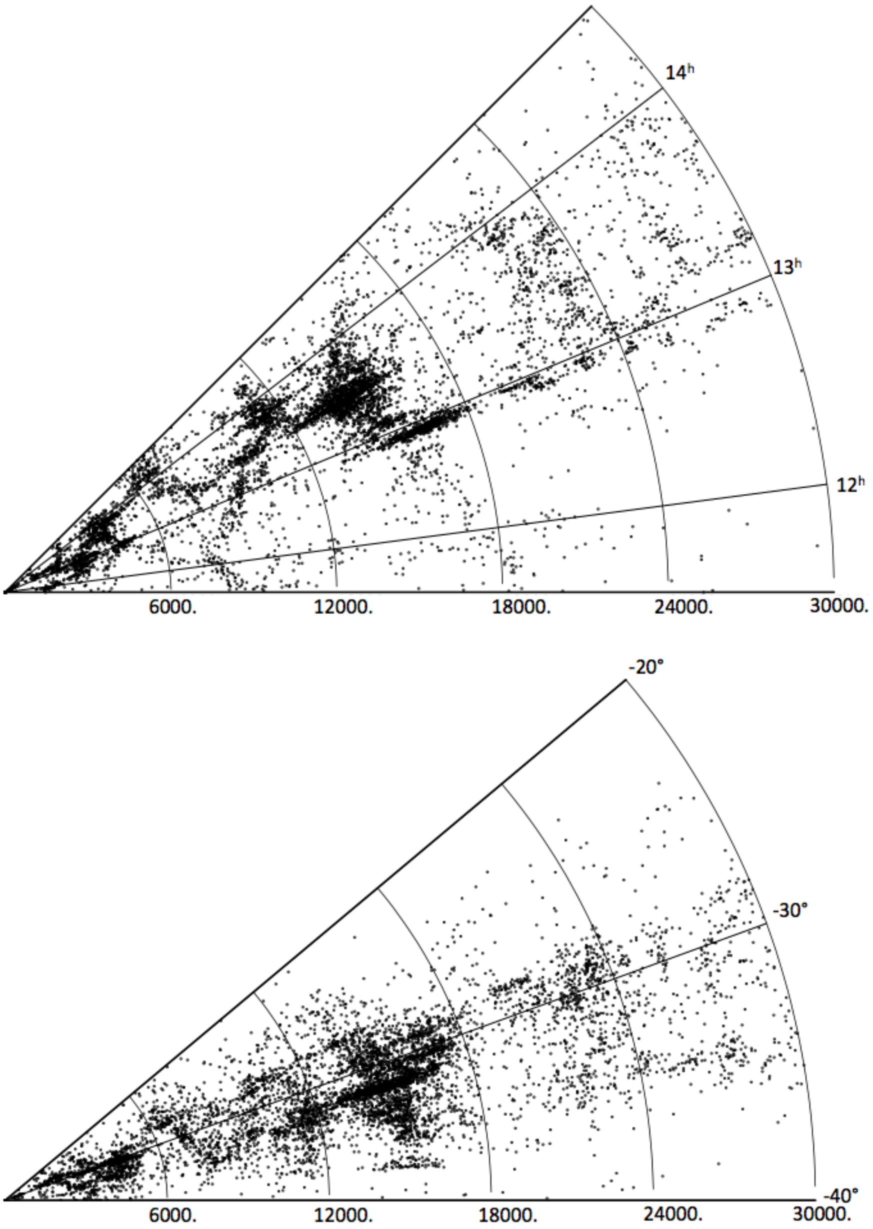

Figure 2.1: Cone diagram in RA (top panel) and DEC (bottom panel) of the galaxies observed in the area of the Shapley supercluster up to a recession velocity of 30000 km s^{-1} (Proust et al. 2006). The largest overdensity of the concentration is located at $v \lesssim 20000$ km s^{-1}, where it is located the Shaplet Concentration Core.

that if the anisotropy with respect to the CMB reflects the peculiar motion of our Galaxy, then the Shapley Concentration could be responsble for up to 20% of that observed. Another hypothesis was made by Tully et al. (1992) who proposed that the Local Group, the Shapley Concentration and the Great Attractor could be a single large structure with a linear size of about 450 Mpc. Raychaudhury et al. (1991) also found that the Shapley Concentration produce a deviation to the CMB temperature fluctuation of $\approx 2.8 \times 10^{-5}$.

In addition to the study on the CMB anisotroy, another important cosmological test provided by the study of the size and the mass distribution of the Shapley Concentration is related to the formation and evolution of the density fluctuations formed in the early Universe. According to numerical simulation, the Shapley Concentration is consistent with the prediction of the ΛCDM or open CDM cosmology (Bardelli et al. 2000).

2.2 The Shapley Concentration Core

The most interesting region of the Shapley Concentration is the central one, whose coordinates are $\alpha_{\mathrm{J2000}} = 13^{\mathrm{h}}05^{\mathrm{m}}57.8^{\mathrm{s}}$ and $\delta_{\mathrm{J2000}} = -33^{\mathrm{d}}04^{\mathrm{m}}03^{\mathrm{s}}$, at redshift $z = 0.043$. It is formed by three cluster complexes which include more than 20 ACO clusters[1] that produce an overdensity of galaxies of $\frac{N}{\langle N \rangle} = 11.3 \pm 0.4$ on a scale of 10 h^{-1} Mpc (Bardelli et al. 2000).

In this thesis we focus on the A3558 and the A3528 cluster complexes. The summary of the main characteristics of the galaxy clusters studied here is reported in table 2.1.

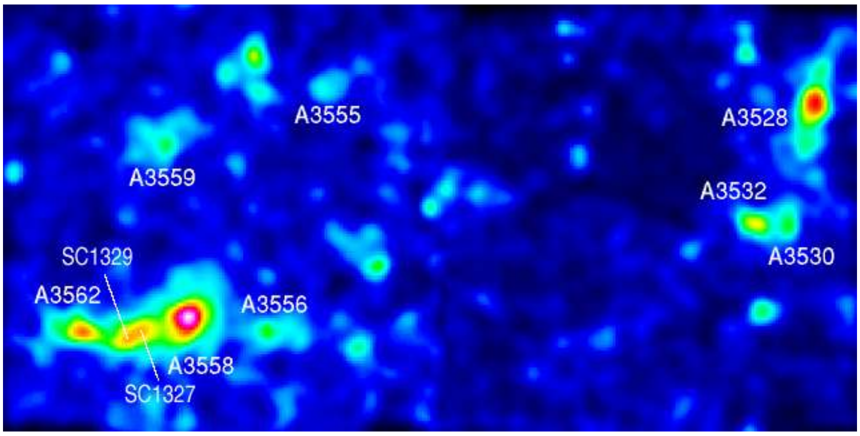

Figure 2.2: Optical image of the central region of the Shapley Concentration (Bardelli et al. 2000). The two cluster complexes are clearly visible: in the inner core of the concentration there is the A3558 complex, while westward there is the A3528 one.

---

[1] Classification of galaxy clusters in the southern sky provided by Abell, Corwin & Olowin (1989).

2.2.1 The A3558 complex

The A3558 complex is a chain formed by three ACO galaxy clusters (A3556, A3558 and A3562) and two poor groups (SC 1329-313 and SC 1327-312). It elongates about 3° in the east-west direction, with a comoving size of about 7.5 h^{-1} Mpc. It is coincident with the cloud initially discovered by Shapley.

Optical emission

The cluster complex lies in a velocity range $12000 \lesssim v \lesssim 18000$ km s^{-1}, with an average value of $v = 14248$ km s^{-1} and a gaussian velocity dispersion of $\sigma = 1083$ km s^{-1} (Bardelli et al. 1994). The large velocity dispersion suggests that this cluster complex may not be in a dynamically relaxed state. In addition to that, the isodensity contours displayed in the left panel of figure 2.3 show that the three galaxy clusters are connected to each other in a very complicated structure. The complex is visible also in the the velocity distribution analysis of the galaxies: the structures aligned perpendicularly to the cluster complex alignment, the so-called fingers-of-God, and sub-groups between A3558 and A3562 are visible in the wedge diagramm (right panel in figure 2.3).

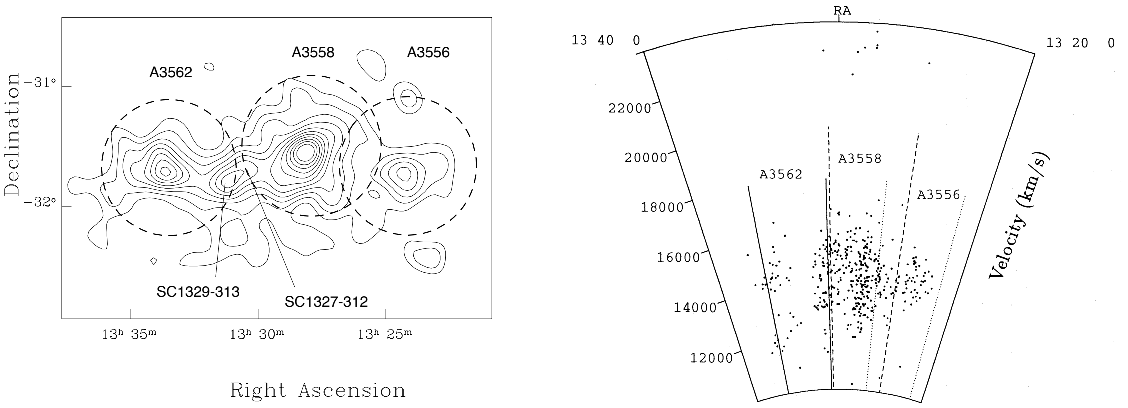

Figure 2.3: *Left panel*: isodensity contours for galaxies with $b_J \leq 19.5$; the dotted circles indicate the cluster Abell radii. *Right panel*: wedge diagram of the cluster complex; the dotted, solid and dashed lines represent the projected Abell radii for A3558, A3562 and A3556, respectively. (Bardelli et al. 1998).

The most massive cluster of the complex is A3558 which is dominated by a cD galaxy. It was classified as a richness class 4 cluster by Abell, Corwin & Olowin (1989), but then it has been rescaled to a richness class 2 by Metcalfe, Godwin & Peach (1994). Such an overestimate was probably due to the contamination of the nearby A3556 cluster. Indeed, the two clusters have a projected distance less than their Abell radii ($R_A = \frac{1.7}{z}$ arcmin, chapter 1), thus an interaction between them can not be ruled out. The estimate of the average velocity of this cluster is controversial and strongly dependent on the choice of the cluster radius: Bardelli et al. (1998) obtained an average velocity of $v = 14262^{+75}_{-82}$ km s^{-1} and $\sigma = 992^{+85}_{-60}$.

A3556 is a poor (richness class 0) cluster dominated by two giant ellipticals. The average velocity is $v = 14357 \pm 76$ km s^{-1} and $\sigma = 643^{+53}_{-43}$. The velocity distribution is characterized by two peaks, centered on the two dominant galaxies. Moreover, the galaxy density profiles differ from bright and faint galaxies, which is probably due to the presence of the substructures found in the dynamical analysis.

The third cluster of the complex is A3562, a richness class 2 cluster dominated by a cD galaxy. The average velocity is $v = 14492^{+225}_{-286}$ km s^{-1} and $\sigma = 913^{+189}_{-96}$: the velocity dispersion is high, probably due to the presence of filamentary structures, the fingers of God, and of two subcondensations located between it and A3558, namely SC 1327-312 and SC 1329-313.

The filamentary structures and the subcondensations present in the cluster complex strongly suggest that we are observing a region in a dynamically active state, where cluster formation is generated by merger events, as predicted by the bottom-up scenario. In particular, the A3558 cluster complex could be the result of a cluster-cluster collision seen after the first core-core encounter. The effects of such interaction are clearly visible in the X-ray and in the radio bands, as it will be discussed below.

X-ray emission

The X-ray emission from the cluster complex has been studied by many authors, and observations were performed by several instruments such as ROSAT, Beppo-Sax, ASCA, XMM-Newton and Chandra. As seen in the optical band, the X-ray emission shows an elongated and filamentary shape of the complex. The brightest feature is A3558, but A3562 and the two subcondensation, SC 1327-312 and SC 1329-313 are clearly visible too. On the contrary, the A3556 cluster is rather faint in this band (figure 2.4).

The X-ray surface brightness of A3558 is described by two component that are well fitted by a Gaussian and an elliptical King profile (Bardelli et al. 1996). The former coincides with the central region, which is dominated by the optical galaxy, even if the authors found that it is shifted by 1.3' with respect to the centroid of the

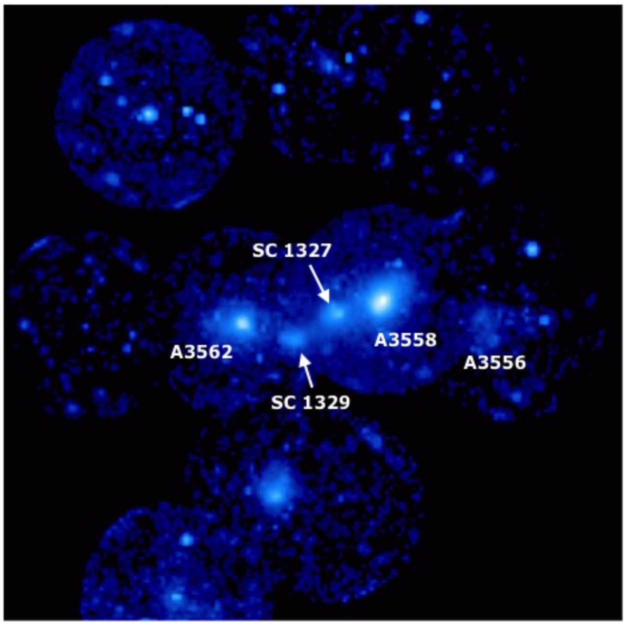

Figure 2.4: ROSAT image of the A3558 cluster complex (Ettori et al. 2000).

sourronding cluster, while the latter is associated with the ICM. The temperature analysis of the cluster was performed with several instruments, which provide results in good agreement with each other, considering their different characteristics. The average temperature found by Markevitch & Vikhlinin (1997) with the ASCA satellite is $5.5^{+0.3}_{-0.2}$ keV. The temperature profile is roughly constant in the inner region, while it decreases at larger radii. This agrees with the prevoius results found by Bardelli et al. (1996) with ROSAT observations: indeed, the two profiles differ only in the central region, where the latter decreases (left panel in figure 2.5). Such discrepancy is probably due to the different energy range of the two instruments.

A3562 has a behaviour similar to A3558. Observations with ROSAT, ASCA and Beppo-Sax (Ettori et al. 2000) found a discrepancy of the temperature values that could be explained by different calibration problems. Such idea is confirmed by the fact that comparing two similar instruments like ASCA and Beppo-Sax, the temperature values agree approximately well. The X-ray emission of the cluster shows a deviation from the symmetric distribution typical of a relaxed system: A3562 has elongated emission in east-west direction, pointing towards A3558 and the SC 1329-313 group. As for A3558, the radial temperature profile (right panel, figure 2.5) decreases toward the outer part of the cluster.

The X-ray emission of SC 1327-312 is simmetric and roundish, while SC 1329-313 has a comet-like shape, with the peak centered on its dominant galaxy and the tail

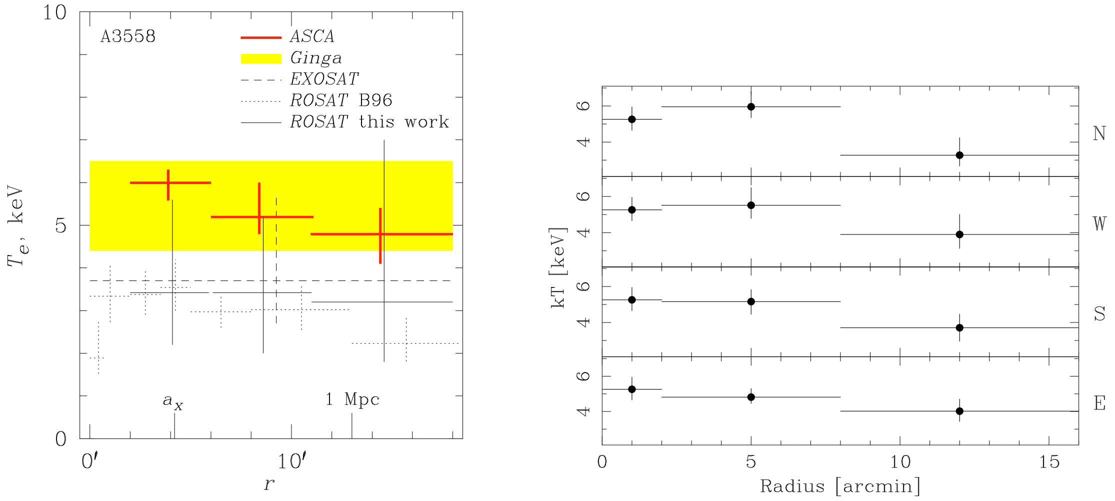

Figure 2.5: *Left panel*: projected temperature profiles of A3558 obtained by different instruments (Markevitch & Vikhlinin, 1997). *Right panel*: radial temperature profiles of A3562 in different directions obtained by Beppo-Sax observation (Ettori et al. 2000).

which elongates eastwards. Such shape is consistent with the hypothesis of a merger event which has involved the whole region. This is supported also by the X-ray emissivity coming from the filaments which connect SC 1327-312 and SC 1329-313 with A3558. The temperature values found with ASCA for SC 1329-313 and SC 1327-312 are $4.2^{+0.15}_{-0.23}$ and 3.8 ± 0.13, respectively (Hanami et al. 1999).

Radio emission

Another important piece of evidence supporting the merger events in the A3558 cluster complex is given by the analysis of the radio emission. Indeed, as we have seen in chapter 1, in addition to an enhancement of the intensity of the X-ray emission, a merger event can deeply affect the radio emission at many levels. Here we deal with the statistical properties of the radio galaxies and with the diffuse cluster-scale emission.

The statistical analysis presented by Venturi et al. (2000) suggests that in the A3558 cluster complex there is no difference between the count of sources of the complex and the source of the background. Such result implies that the optical overdensity found by Bardelli et al. (1998) does not reflect into an overdensity of the radio sources. Furthermore, by the comparison between the local optical density and the ratio between the radio and optical flux, the same authors found that the radio galaxy in the cluster complex are distribuited indipendent of the local density,

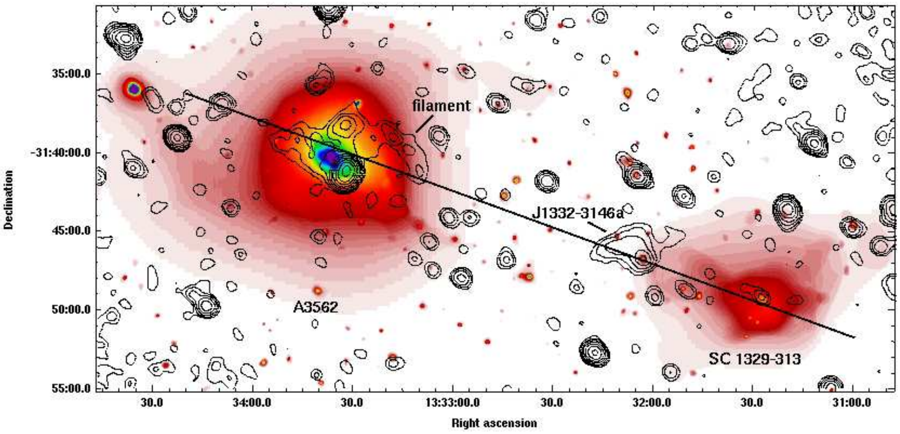

Figure 2.6: VLA contours at 1.4 GHz of A3562 and SC 1329-313 superimposed on XMM-Newton mosaic in the 0.8-2 keV band (Giacintucci et al. 2005). The solid line show the alignement between the A3562, SC 1329-313 and J1332-3146, according to the merger scenario.

and thus that the merging environment does not affect the statistical properties of the radio galaxy emissivity. Moreover, Venturi et al. (2000) show that the radio luminosity function of the radio galaxies in this complex is lower than the typical one found in the cluster galaxies (Ledlow & Owen, 1996). This means that the probability that an elliptical galaxy of given magnitude develops a radio galaxy in this region is not only indipendent on the optical overdensity (as thought by Fanti 1984, and Ledlow & Owen 1996), but it is also lower than in a typical cluster environment.

Giacintucci et al. (2004) found that the outskirts of the chain, A3556 and A3562, contain the largest fraction of radio galaxies in the cluster complex, while A3558 does not show any radio galaxy. This suggests that A3558, which led the merger, is the the main responsable of the decrement of radio galaxies noted by Venturi et al. (2000). Furthermore, it is also the cluster which is mostly affected by the interaction, quenching almost completely its radio galaxy activity. A detailed description of the radio galaxy contents will be given in chapter 4.

The diffuse radio emission is instead clearly seen only in the A3562 cluster (Venturi et al. 2003). A3562 has a one of the smallest and less powerful radio halo known so far, with a linear size of about 470 kpc and a radio power of $P_{1.4\ \mathrm{GHz}} \approx 1.1 \times 10^{23}$ W Hz^{-1}. Its morphology is not roundish as the typical halos, but it is elongated in north-east direction. A filamentary structure extending from the radio halo towards west has been detected. It is unclear if it is a relic or a feature of the radio halo.

The radio halo encompasses a head-tail radio galaxy, J1333-3141, which is a good candidate to provide the relativistic particles in the cluster center. The two possible interpretations for the low radio halo emission are either a modest re-acceleration phase or an advanced stage of a re-acceleration process. A possible merger scenario was proposed by Giacintucci et al. (2005), who suggested that the filament (figure 2.6) is pointing toward the poor cluster SC 1329-313, whose extended radio source, J1332-3146a, elongates also in direction of A3562. The almost perfectly aligned emission seen in figure 2.6 gives a further support to the scenario of cluster merger between A3562 and SC 1329-313. It is interesting to note that very recent observations at low frequencies point out the possible presence of two elongates structures, located approximately at $\alpha_{\rm J2000} = 13^{\rm h}30^{\rm m}45^{\rm s}$ and $\delta_{\rm J2000} = -31^{\rm d}43^{\rm m}00^{\rm s}$ and $\alpha_{\rm J2000} = 13^{\rm h}30^{\rm m}50^{\rm s}$ and $\delta_{\rm J2000} = -31^{\rm d}48^{\rm m}00^{\rm s}$ (figure 2.7). The nature of these two sources is still unclear. The latter has no optical counterpart, and could be a relic of linear size of about 350 kpc; the former is a possible residual radio galaxy. The connection of these peculiar sources and the dynamics of the A3558 complex is under investigation (Venturi et al., in preparation).

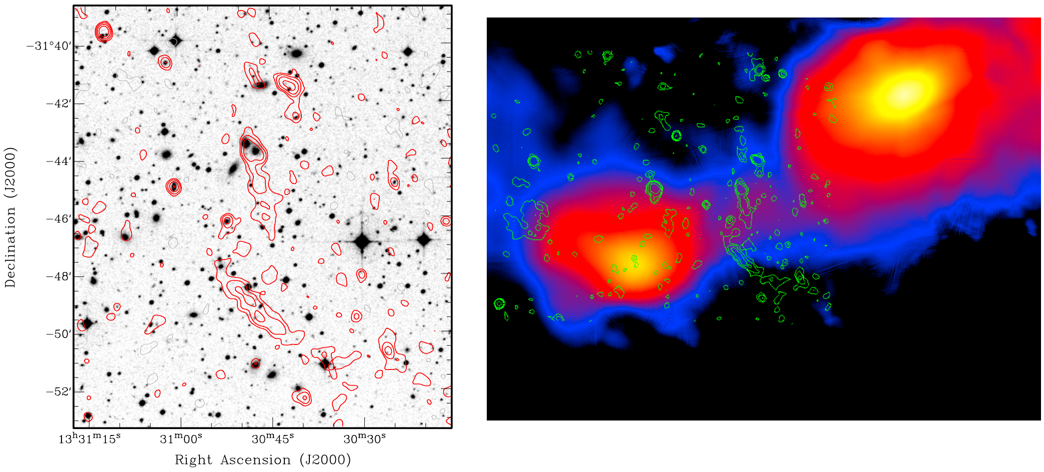

Figure 2.7: *Left panel*: GMRT radio contours at 325 MHz superimposed with the optical image of the west region of A3562 (Venturi et al., in preparation). The levels are ±0.3×(2, 4, 8...) mJy/beam. *Right panel*: radio/X-ray superimposition (Chandra image: courtesy of Prof. Mazzotta).

2.2.2 The A3528 complex

The A3528 complex is a chain of four ACO clusters (A3528, A3530, A3532 and A3535) located at a projected distance of approximately 19 h^{-1} Mpc north-west of

A3558 (see figure 2.2) at a mean redshift of $z \approx 0.0535$. It elongates about 3° in the north-south direction and about 1.7° in west-east, with a comoving size of about 7.5 h^{-1} Mpc in lenght and of about 5 h^{-1} Mpc in width.

Optical emission

The cluster complex lies in a velocity range that spread over $13000 \lesssim v \lesssim 24000$ km s^{-1}. The isodensity contours displayed in the left panel in figure 2.8 show that A3528 is aligned along the north-south direction, pointing toward the A3530-A3532 pair, which extends in the west-east direction. Since the distance of the two latter components is less than their Abell radii, the two clusters are interacting. This is also suggested by the wedge diagram, where the A3530-A3532 pair looks compressed in a single structure, and the finger-of-God features are clearly displayed (right panel in figure 2.8).

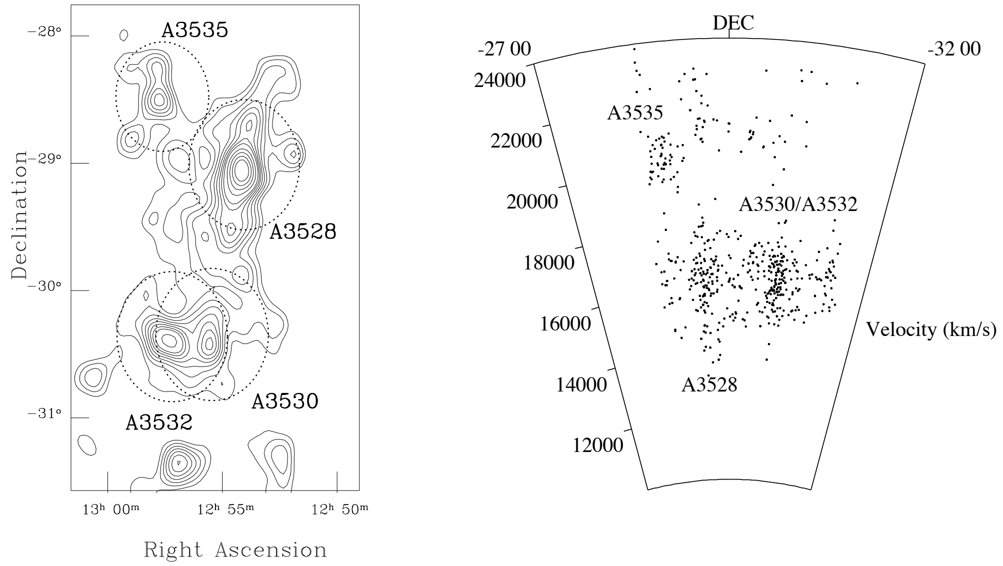

Figure 2.8: *Left panel*: isodensity contours for galaxies in the magnitude range $17 \leq b_{\rm j} \leq 19.5$; the dotted circles indicate the cluster Abell radii. *Right panel*: wedge diagram of the cluster complex; the plotted coordiate is the declination in order to have a better visualization of the whole complex. (Bardelli et al. 2001).

A3528 is the dominant cluster of the complex and it is classified as richness class 1. The average velocity and the velocity dispersion of the system are $v = 16332^{+72}_{-116}$ km s^{-1} and $\sigma = 955 \pm 86$ km s^{-1}, respectively (Bardelli et al. 2001). Although it is well approximated by a single Gaussian distribution, the velocity distribution is characterized by several peaks suggesting the possible presence of substructures (figure 2.9). The bi-dimensional analysis seems to confirm this scenario. The cluster is dominated by two bright galaxies, which are located in correspondence of the two peaks in the velocity distribution.

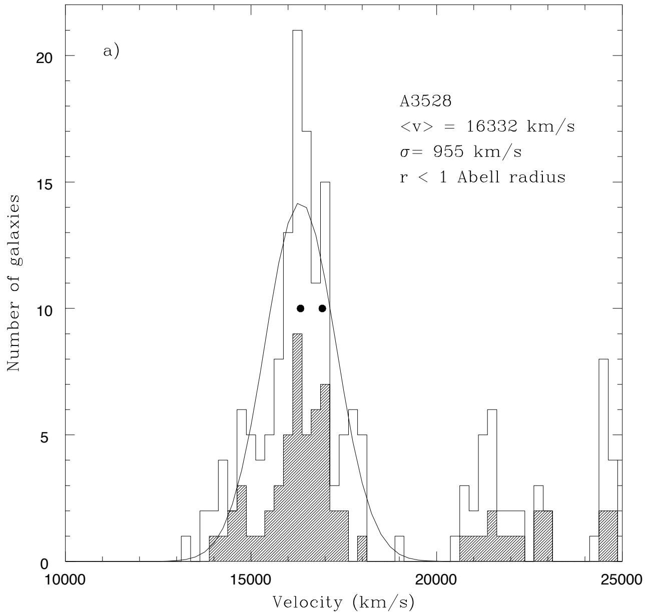

Figure 2.9: Velocity histogram for A3528 superimposed by the Gaussian distribution (Bardelli et al. 2001).

The A3530-A3532 pair is formed by two richness class 0 clusters. Due to their small distance, it is impossible to obtain information on the velocity distribution of the two separate systems without contamination of the other. For this reason, Bardelli et al. (2001) restricted the analysis into the very central region of both clusters. The resulting values are $v = 16274^{+78}_{-110}$ km s^{-1} and $\sigma = 730^{+143}_{-53}$ km s^{-1} for A3530, and $v = 16605^{+76}_{-161}$ km s^{-1} and $\sigma = 618^{+158}_{-28}$ km s^{-1} for A3532. The former is dominated by two bright elliptical galaxies, while the latter has a dumb-bell galaxy in its center.

X-ray emission

According to Raychaudhury et al. (1991) who pointed out the presence of many double and multiple clusters in the core of the Shapley Concentration, ROSAT observations first (Schindler et al. 1996) and XMM-Newton observation later (Gastaldello et al. 2003, figure 2.10) show that A3528 is characterized by two subclumps in the X-ray band, aligned in north-south direction and named A3528N and A3528S

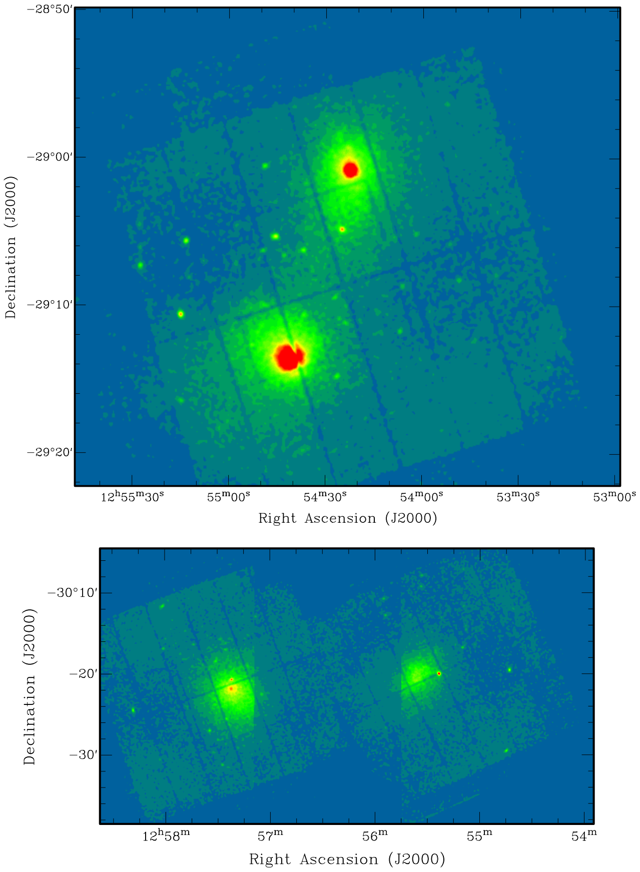

Figure 2.10: *Top panel*: XMM-Newton image of A3528; the two bright spot coincide with A3528N and A3528S. *Bottom panel*: XMM-Newton image of A3530, on the right, and A3532, on the left (Credits: Gastaldello et al. 2003).

respectively. These two peaks are separated by 13.5 arcmin (corrisponding to a projected distance of 0.9 h_{70}^{-1} Mpc at the cluster redshift) and are centered on the two dominant galaxies of the cluster. Moreover, the X-ray emission show that they are connected by a faint diffuse bridge, where Schindler at al. (1996) measured a slight increase of the gas temperature. Such temperature enhancement was explained by the same authors as the presence of shock as a consequence of an interation between A3528N and A3528S.

Using XMM-Newton observations, Gastaldello et al. (2003) revised this interpretation. They found that the gas temperature of the region between the subclusters is consistent with A3528N and A3528S (about of 4.05 keV, 4.14 keV and 4.29 keV respectively), thus the hypothesis of heated gas by shock due to a major merging event was rejected. This conclusion is also confirmed by evidence in both subclusters of cool-cores and steep positive gradients in metal abundance, which are typical of

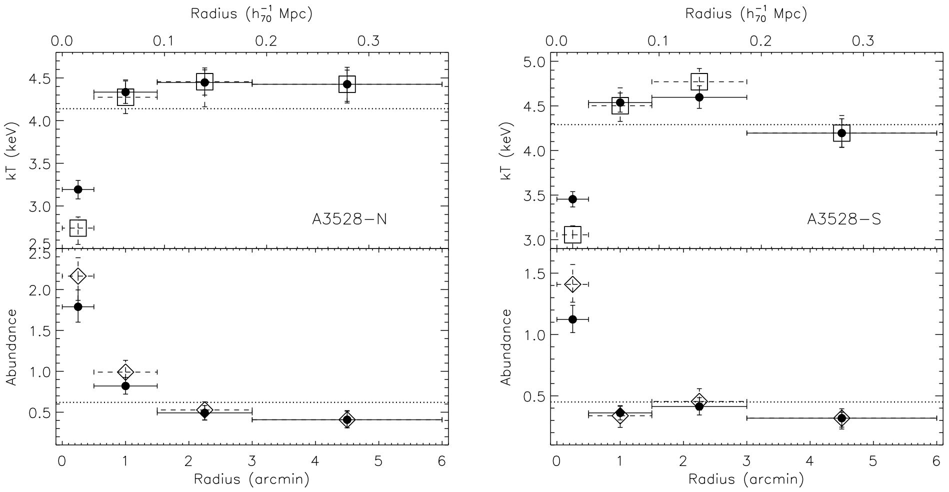

Figure 2.11: Temperature (upper panels) and metal abundance (lower panel) profiles for A3528N and A3528S (Gastaldello et al. 2003). The circles show the best-fit results, while the squares the de-projected values. The dotted lines indicate the temperature value from a spatially integrated fit.

dynamically relaxed system (figure 2.11). Moreover, the authors found that the surface brightness has a significant excess in the north-west direction of A3528N and in the north-east direction of A3528S. Hence, they suggested a scenario in which the two subcluster are orbiting around each other, as a consequence of an off-axis post-merger event.

The X-ray emission peak associated with the A3530-A3532 pair shows that the two clusters are connected by diffuse emission, as for the A3528N and A3528S (Lakhachaura et al. 2013). Thus, it is a further evidence of interaction between these two clusters. The analysis of the temperature and metal abundance profiles are performed with XMM-Newton and Chandra, even if the latter was available only for A3532. The results, plotted in figure 2.12, show that the two clusters are different: A3532 is a typical non cool-core cluster, with no gradient in metal abundance and a flat temperature profile in the inner regions; on the contrary, A3530 show a slight indication of decreasing temperature and a negative gradient of the metal abundance. Such profiles are explained by considering that the interaction is still marginal and that the temperature enhancement in the central region of A3532 is possibly due to a feedback of the dumb-bell galaxy.

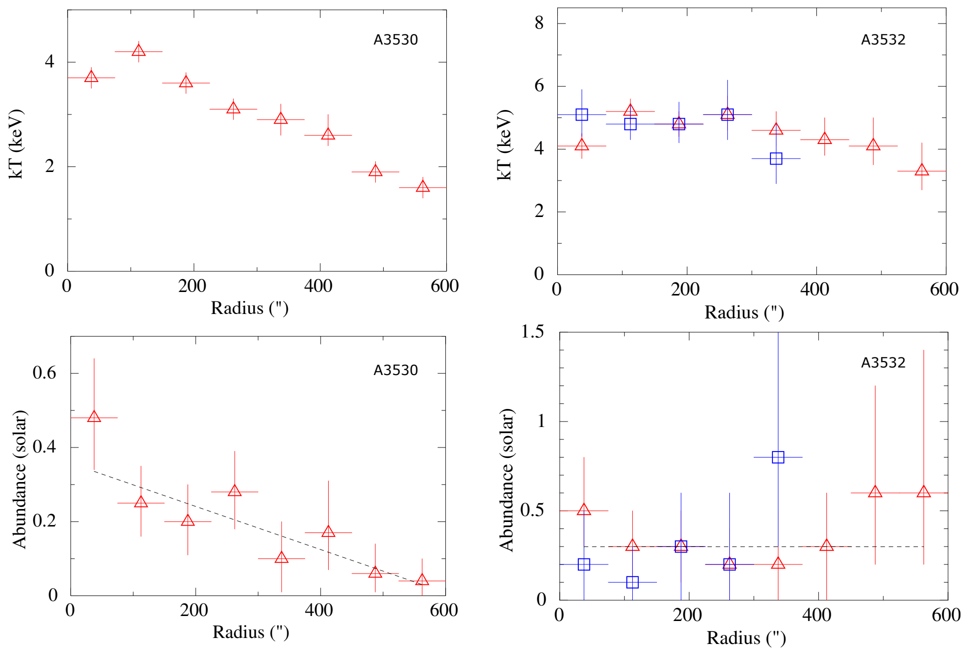

Figure 2.12: Projected temperature (upper panels) and metal abundance (lower panel) profiles for A3530 (left) and A3532 (right). The red and blue points represent the XMM-Newton and Chandra observations, respectively (Lakhachaura et al. 2013).

Radio emission

A statistical analysis on the radio emission properties of the galaxies was performed for the A3528 complex (Venturi et al. 2001). Also in this case, the comparison between the source counts in this region and in the background shows that the optical and radio overdensities are not correlated. This confirms the idea that in an overdense region, like the Shapley Concentration Core, there is the same probability to observe radio galaxies as in the field. Unlike A3558, the radio luminosity function of the A3528 complex is in agreement with the one found by Ledlow & Owen (1996). A possible explanation is proposed by Venturi et al. (2001), who claimed that the advanced merging state of the A3558 complex could inhibit the probability of radio activity. Hence, it was suggested that the different stage of the merging could influence the radio luminosity function of the ellipticals.

In radio band the A3528 complex is dominated by the extended emission from radio galaxies with distorted morphologies. Most of them are placed in the A3528 cluster and few are observed in A3532 and in its periphery. On the contrary, A3530 shows no radio emission, even if it has a pair of ellipticals in its center. The properties of these radio galaxies will be discussed in the chapter 4.

Finally, no radio halos, relics or mini-halos have been observed in the complex. Such diffuse emission could indeed be lacking, but it could also be undetectable with the current instruments.

2.3 The aim of this thesis

The aim of this thesis is to investigate the different morphologies and activity states of the extended radio galaxies belonging to the two cluster complexes. The purpose is to have a better understanding of the dynamical state of the A3528 complex and whether it can be described as an early merger or a tidal one. On the other hand, the comparison with the A3558 complex, which has already undergone the first core-to-core encounter, will lead to a better understanding of the effects that cluster mergers may have on the radio galaxies and on the formation of cluster-type radio sources, such as radio relics and halos.

In order to do so, the high frequency literature studies are combined with the low frequency observations at 235 and 610 MHz, provided with the Giant Metrawave Radio Telescope (GMRT) and reduced with the AIPS package. The low frequency observations emphasise the diffuse structures, while the high frequency ones provide the indentification of the break frequency, which gives the ages of the sources, or at least a lower limit value. The wide frequency range (150 MHz $\div$ 8.4 GHz) provide a good extimation of the spectral properties of the radio galaxies in the A3528 and the A3558 complexes, which will be compared to each other and will be discussed in the light of thier dynamical state.

This will be the starting step of a following study, whose purpose is to understand the effect of the intracluster medium (ICM) on the non-thermal emissions.

Cluster's name	RA (J2000)	DEC (J2000)	z	richness class	R (arcmin)	R_{500} (Mpc)	$M_{500}/10^{14}$ ($\mathrm{M}_\odot$)	T (keV)	$L_{\mathrm{bol}}/10^{44}$ (erg s^{-1})
A3528	$12^{\mathrm{h}}54^{\mathrm{m}}34^{\mathrm{s}}$	$-29^{\mathrm{d}}08^{\mathrm{m}}30^{\mathrm{s}}$	0.0528	1	12.24	-	-	$4.0^{(a)}$	2.95
A3528N	$12^{\mathrm{h}}54^{\mathrm{m}}22^{\mathrm{s}}$	$-29^{\mathrm{d}}00^{\mathrm{m}}46^{\mathrm{s}}$	0.0528	-	6.01	1.65	7.23	$3.4^{(a)}$	1.13
A3528S	$12^{\mathrm{h}}54^{\mathrm{m}}40^{\mathrm{s}}$	$-29^{\mathrm{d}}13^{\mathrm{m}}44^{\mathrm{s}}$	0.0528	-	6.33	-	-	$3.1^{(a)}$	1.31
A3530	$12^{\mathrm{h}}55^{\mathrm{m}}31^{\mathrm{s}}$	$-30^{\mathrm{d}}19^{\mathrm{m}}53^{\mathrm{s}}$	0.0537	0	9.7	1.40	4.69	$3.2^{(b)}$	1.04
A3532	$12^{\mathrm{h}}57^{\mathrm{m}}22^{\mathrm{s}}$	$-30^{\mathrm{d}}22^{\mathrm{m}}03^{\mathrm{s}}$	0.0554	0	11.4	1.55	6.38	$4.4^{(a)}$	2.99
A3556	$13^{\mathrm{h}}24^{\mathrm{m}}06^{\mathrm{s}}$	$-31^{\mathrm{d}}39^{\mathrm{m}}45^{\mathrm{s}}$	0.0479	0	7.1	1.29	3.63	$3.8^{(c)}$	0.17
A3558	$13^{\mathrm{h}}27^{\mathrm{m}}55^{\mathrm{s}}$	$-31^{\mathrm{d}}29^{\mathrm{m}}24^{\mathrm{s}}$	0.0480	2	13.1	1.94	12.18	$5.5^{(d)}$	6.68
A3562	$13^{\mathrm{h}}33^{\mathrm{m}}30^{\mathrm{s}}$	$-31^{\mathrm{d}}40^{\mathrm{m}}00^{\mathrm{s}}$	0.0490	2	14.0	1.54	6.12	$5.1^{(e)}$	4.3
SC 1327-312	$13^{\mathrm{h}}29^{\mathrm{m}}47^{\mathrm{s}}$	$-31^{\mathrm{d}}36^{\mathrm{m}}29^{\mathrm{s}}$	0.0495	-	11.4	1.36	4.27	$3.8^{(c)}$	1.27
SC 1329-313	$13^{\mathrm{h}}31^{\mathrm{m}}36^{\mathrm{s}}$	$-31^{\mathrm{d}}48^{\mathrm{m}}46^{\mathrm{s}}$	0.0446	-	7.2	1.07	2.05	$4.2^{(c)}$	0.52

Table 2.1: Summary of the properties of the galaxy clusters that lie in the core of the Shapley Concentration (De Filippis et al. 2005). The virial radii and masses are taken by Ettori et al. (1997), with $\mathrm{H}_0 = 50$ km s^{-1} Mpc^{-1} assumed. Temperature references: (*a*) Schindler et al. (1996); (*b*) Ettori et al. (1997); (*c*) Hanami et al. (1999); (*d*) Markevitch (1998); (*e*) Ettori et al. (2000).

CHAPTER 3

DATA ANALYSIS

The great advantage of observing at radio wavelenghts is that the atmonsphere has a very low impact on the radiation, unlike the optical band which is strongly dependent on the weather condition, or the X-ray band where the atmosphere is totally opaque to the radiation (figure 3.1). In particular, there is a frequency range in the electromagnetic spectrum, called *radio window*, that extends roughly from 30 MHz to 300 GHz where the atmosphere is totally transparent to the radiation and, for this reason, this radio emission is observable from the ground. The frequency range limits are due to the absorption of the free electrons in the ionosphere, at low frequencies and to the absorpion of the water vapour at high frequencies. On the other hand, the main issues for the radiation detection at these wavelenghts are the human interference and the weakness of the radio source signal.

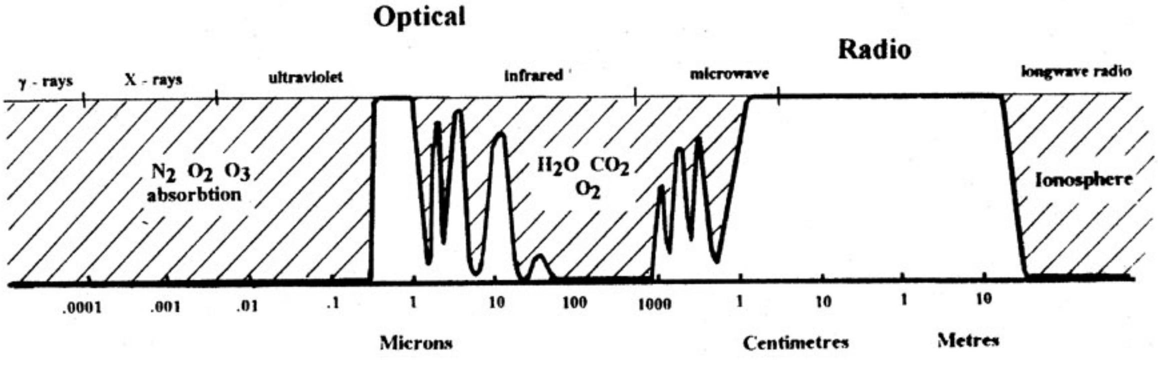

Figure 3.1: Radiation tasmission in the atmosphere: the white zones describe the wavelenghts at which the atmosphere is trasparent.

In this chapter I will be present the main characteristics of the instruments allowing the radio emission detection (sections 3.1 and 3.2) and the data reduction procedure (section 3.3).

3.1 Radio Telescopes

Radio telescopes are the instruments that allow the radio emission detection. They are generally made up of a parabolic dish, called antenna and acting like a mirror, that reflects the radio wave to the focus, and a reciever system that detects the signal and amplifies it.

Since the signal from radio sources is extremely weak, the radio telescopes need to be as large as possible. Despite that, the angular resolution ϑ of a single dish, i.e. the smallest angular distance for which it is possible to distinguish two point-like sources as two different objects, is very low:

$$\vartheta = \frac{\lambda}{D} \tag{3.1}$$

where λ is the radio wavelenght, D is the antenna diameter and ϑ is expressed in radians. The problem is that, even if the antenna is large, the typical radio wavelenghts are large too: if we consider the largest circular radio telescope built to date, the Arecibo radio telescope, with $D \approx 300$ m, and a typical radio wavelenght, e.g. $\lambda = 20$ cm, we obtain $\vartheta \approx 2$ arcminutes, that is worse than the angular resolution of the human eye ($\vartheta \approx 1$ arcmin). This problem is solved by the interferometry (section 3.2). On the other hand, at large radio wavelenghts ($\lambda > 1$ m), the reflector surface can be formed by a wire mesh.

Other important parameters relevant for the characterization of an antenna include aperture efficiency, pointing accuracy, beam circularity, sidelobe levels and noise temperature. The effective collecting area $A(\nu, \theta, \phi)$ depends on the frequency ν and on the sky coordinate of the radio source, θ and ϕ. If the radio source sky brightness is $I(\nu, \theta, \phi)$, then the power recived by the antenna in bandwidth $\Delta\nu$ from element of solid angle $\Delta\Omega$ is

$$P = A(\nu, \theta, \phi) I(\nu, \theta, \phi) \Delta\nu \Delta\Omega \,. \tag{3.2}$$

The normalized antenna pattern P_{n} is defined as $P_{\mathrm{n}}(\nu, \theta, \phi) = P(\nu, \theta, \phi)/A_0$, where A_0 is the power recieved at the center of the antenna, i.e. $A(\nu, 0, 0)$. The beam solid angle Ω_{A} of the power pattern is given by

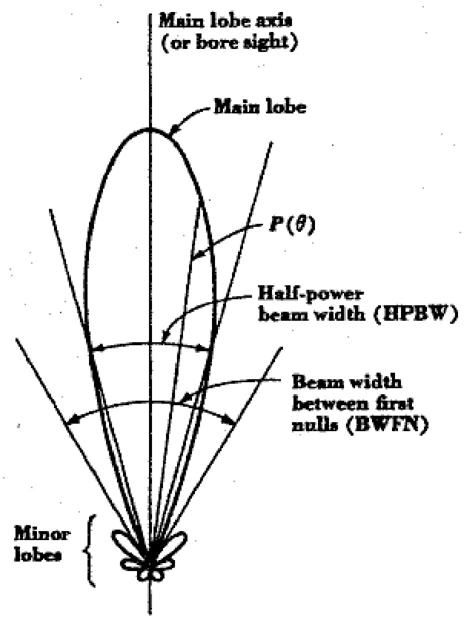

Figure 3.2: The power pattern of an antenna.

$$\Omega_{\mathrm{A}} = \int\int_{4\pi} P_{\mathrm{n}}(\theta, \phi) d\Omega \tag{3.3}$$

and it is the measure of the field of view (FOV) of the telescope. The beam, or power pattern, describes the recieving pattern of the antenna and is characterized by a large main lobe, called main beam, and a series of less prominent secondary sidelobes (figure 3.2). A very useful measure of the main beam is the half power beam width (HPBW) which describes its width.

The ratio between the physical and effective area represents the efficiency η of the antenna that depends on a lot of loss parameters, like the reflector surface efficiency, the reflector blockage and other effects that can reduce the performace of the radio antenna. Another limit to the maximum usable frequency is the antenna pointing accuracy. It involves geometrical and physical factors, such as the structural design of the antenna that can be affected by gravitational force, wind and thermal change, that can not be calibrated.

The total power recieved by the antenna from a given brightness distribution $B(\nu, \theta, \phi)$ per unit of bandwidth is equal to

$$W_{\nu} = mA_0 \int\int_{\Omega} B(\nu, \theta, \phi) P_{\mathrm{n}}(\theta, \phi) d\Omega \tag{3.4}$$

and it coincides with the real radio source flux $S(\nu)$ only if its angular size is much smaller than beam one. The parameter m takes into account polarization, and its value is $m = 1$ in the modern radio telescopes.

Finally, a radio antenna is characterized by an antenna temperature T_{A} that is the temperature radiated by a resistance with a power equal to the one recieved by the antenna, $W_\nu = kT_{\mathrm{A}}$. It is related to the radio source flux density, $T_{\mathrm{A}} = S(\nu)G$, through the gain parameter G that measures the antenna capability to reveal the signal. Thus, the antenna temperature actually is an indicator of the power collected rather than a real temperature.

The sensitivity of a radio telescope is the lowest emission that can be detected by an antenna and it is expressed in terms of signal to noise ratio:

$$\frac{S}{N} = \frac{\alpha T_{\mathrm{A}}}{T_{\mathrm{sys}}} \sqrt{\Delta\nu\Delta\tau} \tag{3.5}$$

where α is a coefficient that depends on the reciever type (order of unity), $\Delta\tau$ is the integration time (s), $\Delta\nu$ is the reciever bandpass and $T_{\mathrm{sys}} = T_{\mathrm{A}} + T_{\mathrm{R}}$ is the system temperature. The latter parameter is calculated by considering the contribution of the antenna temperature and the termal noise T_{R}, called the reciever noise temperature, which is generally at least one order of magnitude or even two larger than T_{A}.

3.2 Radio interferometry

The interferometry technique was developed for the first time in 1940s to address the angular resolution problem of radio observations. The basic radio interferometer is formed by two antennas (figure 3.3) observing simultaneously and at the same frequency. The incoming radiation does not reach the antennas simultaneously, and for this reason it is necessary to take into account the geometric delay τ_{g} when combining the two signals. It depends on the distance between the antennas and on the apparent source position on the sky, which is continuosly changing. In this way the two antennas perform like a full aperture with a diameter equal to their distance, called baseline. Since it can be much longer than the antenna diameter, it results on an improvement of the angular resolution. In fact, if we recall the equation 3.1 and we replace the antenna diameter D with a baseline of few thousands km (as it is the case of VLBI) we obtain an angular resolution of about few milliarcsecond, that is several orders of magnitude better than that achieved by single dish.

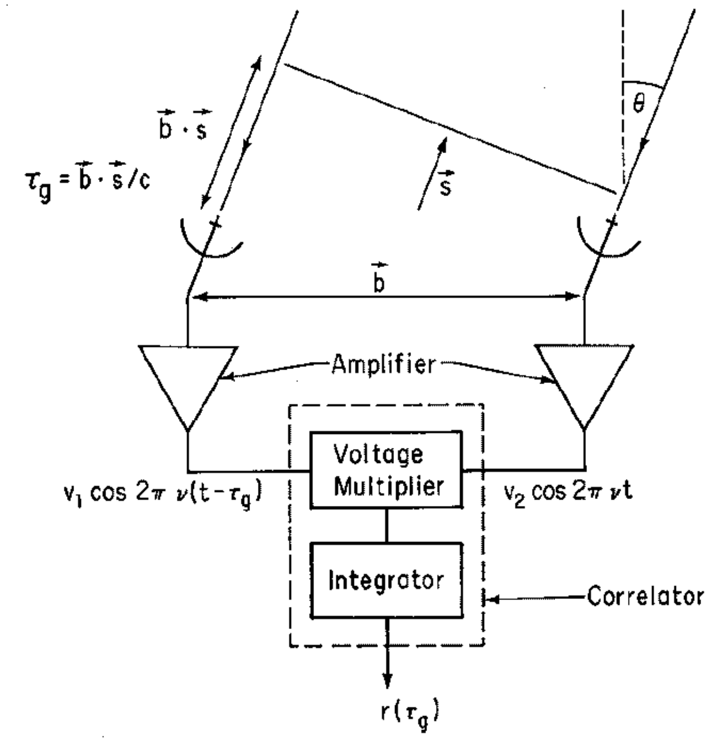

Figure 3.3: Semplified block diagram of a two-element interferometer.

As seen in figure 3.3, the signal collected by the two antennas passes through amplifiers where the filters necessary to select the frequency band $\Delta\nu$ centered on frequency ν are placed. Then the signals V_1 and V_2 are multiplied and time averaged by a dedicated computer known as correlator: the output signal oscillates as the cosine of $2\pi\nu\tau_{\rm g}$ that represents the motion of the source through the interferometer frame, called the fringe pattern. Thus, the output signal represents the correlation of the source brightness distribution I_ν as measured by the instrument, and it is termed visibility funcion:

$$V_\nu(u,v) = \int\int I_\nu(l,m) e^{-2\pi i(ul+vm)} dl dm\,, \tag{3.6}$$

where (u,v) are the coordinates on the fringe visibility plane and (l,m) are the coordinates on the sky of a given point where there can be emission (but this is not necessary). A single interferometer samples the visibility function in a single point determinated by the baseline lenght and orientation. As the geometry changes due to the apparent motion of the source in the sky, the sampled point describes an elliptical track in the u-v plane. The brightness distribution of the source is obtained from the visibility data by inversion of the Fourier Transformation of this last equation:

$$I_\nu(l,m) = \int\int V_\nu(u,v)e^{2\pi i(ul+vm)}dudv\,. \tag{3.7}$$

A modern radio interferometer is generally composed by $N > 2$ antennas that can be combinated into $\frac{N(N-1)}{2}$ baselines. Since the visibility function is only sampled in corrispondence of the baseline position in the u-v plane, to obtain the best possible reconstruction of I_ν it is necessary that the u-v plane is sampled in an optimal way. The maximum length of the u-v coverage, i.e. the longest baseline, provides the angular resolution of the array (equation 3.1), while the smallest baseline provides the largest angular scale which is actually sampled by the interferometer and, than, that can be recovered in the image plane.

Finally, in addition to the baseline lenght, the single dish diameter is another important parameter of a radio interferometer because it provies the FOV of the array, according to the equation 3.1: that means that when the antenna is large, the FOV is small. Furthermore, the sensitivity is maximum at the pointing center and than progressively declines at larger and larger angular distance. An antenna of a diameter of 25 m has a FOV (primary beam) of about 30 arcmin.

3.2.1 The GMRT array

The Giant Metrewave Radio Telescope (GMRT) is an array located in India, about 110 km east of Mumbai and 80 km north of Pune. The site co-ordinate are:

- latitude = 19°05”48’ north;
- longitude = 74°03”00’ east;
- altitude = 650 m.

The location has been chosen because of the combination of a lot of advantages such as the low man-made radio noise, the vicinity with the most important infrastructures, and the quiet ionosphere at this latitude. The array has been in operation since 2000 and it operates at five different frequencies ranging form 150 to 1450 MHz. A major upgrade to provide a full coverage of the band from 50 MHz to 1750 MHz is currently in progress (uGMRT). The interferometer consists on thirty 45 m diameter antennas spread over distances up to 25 km, in a hybrid configuration. Fourteen antennas are randomly distributed in a compact central array with a

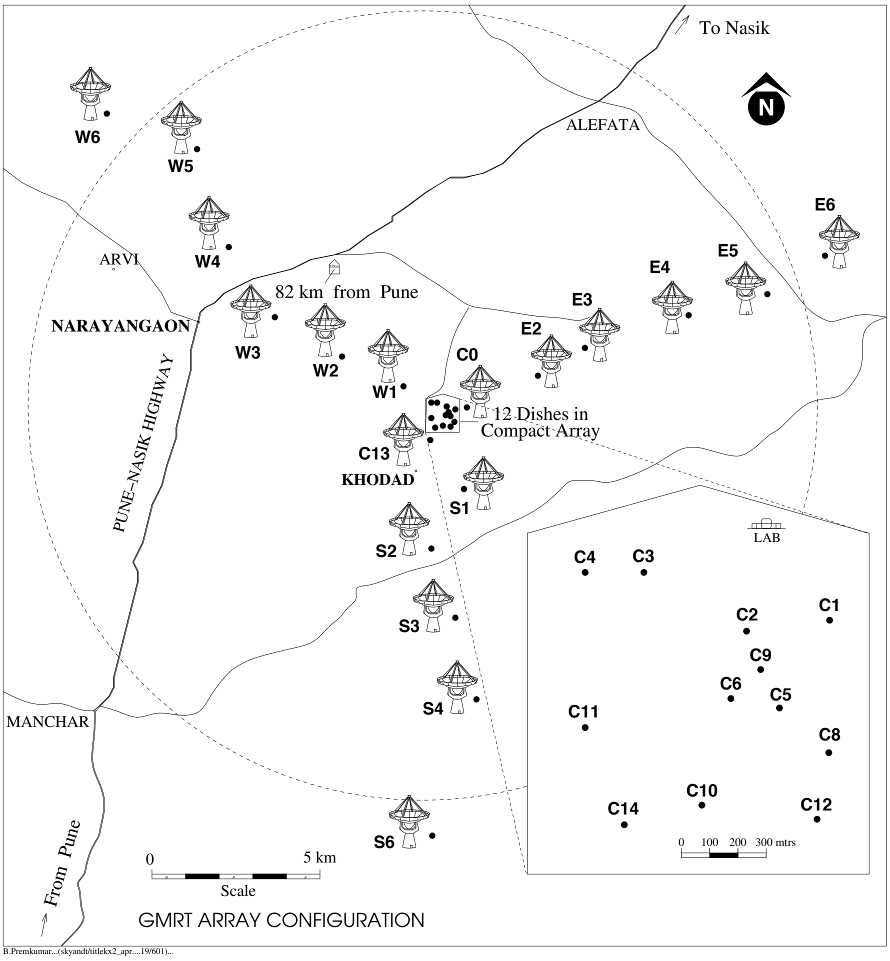

Figure 3.4: GMRT antennas' configuration.

diameter of about 1 km, while the remaining ones are deployed on Y-shaped configuration composed by three arms, called “east”, “west” and “south”, whose length is approximately 14 km. This design is very useful: the central array provides a large number of relatively short baselines (the shorter is about 60 m, projected) that guarantees imaging of large extended sources; on the other hand, since the arms have a 25 km maximum baseline, the observation of small sources, for which high angular resolution is required, is possible too. Hence, a single GMRT observation guarantees a good u-v coverage (figure 3.5), yelding informations on very different angular scales. The main system parameters of the array are summarized in table 3.1.

The GMRT antennas are fully steerable alt-azimuth mounted parabolic dishes, with a focal lenght f equal to 18.54 m. The elevation limit guarantees a declination coverage from $-53°$ to $+90°$, i.e. observations of whole northern sky and a most of

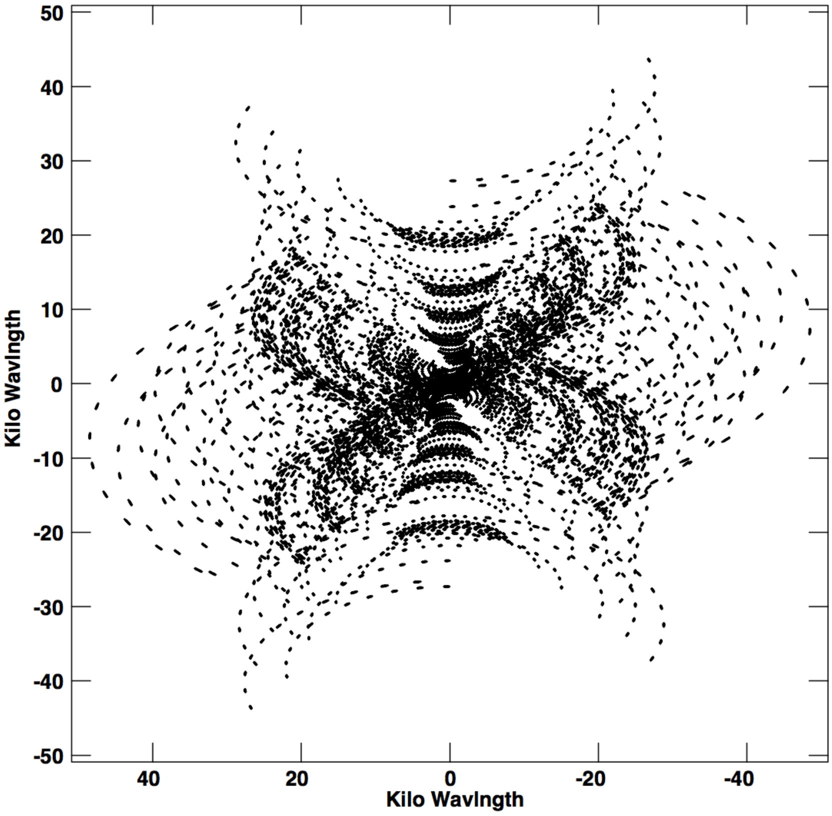

Figure 3.5: GMRT u-v coverage at 610 MHz.

southern one. The reflecting surface of each antenna is a wire mash: it made the project much less expensive and at same time it offers a low resistence to the wind, even if the antennas are not operated when its velocity is higher than 50 m/s. The grid size is 10×10 mm in the central part of the dish and 20×20 mm in the outer ones and that makes it the lightest antenna of its size.

The GMRT operates at five bands centered at 151, 325, 610/235 and the 1000-1420 MHz; the latter reciever is formed by a number of dipoles, while the other bands are formed by circular feeds. They are mounted on the four faces of a rotating turret placed at the focus of the antenna. The 610/235 MHz feed is particularly peculiar: it consists on a dual concentric coaxial cavity in which both the feeds are mounted on the same face, so it is possible to select any of them with both polarization or both of them but with single polarization for each frequency. The feed output is then amplified and converted in intermediate frequency (IF). The correlator allows of a total observable bandwidth of 32 MHz which is divided into two 16 MHz wide blocks, the upper side band (USB) and the lower side band (LSB). It produces a maximum of 512 spectral channels for each of two polarization for each baseline.

Because of its large collecting area and wide frequency coverage, the GMRT allows to reach a lot of different scientific goals, ranging from the studies of the Solar System to the investigations of the formation of the structure in the Early Universe. In particular, the low frequencies make the GMRT the perfect instrument to study the diffuse emission from extended sources like radiogalaxies and galaxy clusters.

	151 MHz	235 MHz	325 MHz	610 MHz	1420 MHz
Primary beam (HPBW, arcmin)	186±6	114±5	81±4	43±3	$(24\pm2)\times(1400/f)$
Reciver temperature (T_R, K)	295	106	53	60	45
Typical T_{sky} (K)	308	99	40	10	4
Typica T_{ground} (K)	12	32	13	32	24
T_{system} ($=T_R+T_{sky}+T_{ground}$, K)	615	237	106	102	73
Antenna gain (K Jy^{-1} $Antenna^{-1}$)	0.33	0.33	0.32	0.32	0.22
Synthesized beam (FWHM)					
- Full array (arcsec)	20	13	9	5	2
- Central square (arcsec)	420	270	200	100	40
Large detectable structure (arcmin)	66	44	32	17	7
Usable frequency range					
- observatory default (MHz)	150-156	236-244	305-345	580-640	1000-1450
- allowed by electronics (MHz)	130-190	230-250	305-360	570-650	1000-1450
Best rms sensitivies achieved (mJy)	0.7	0.25	0.04	0.02	0.03
Typical dynamic range achieved	>1500	>1500	>1500	>2000	>2000

Table 3.1: Main mesured system parameter of the GMRT.

3.3 Data reduction

The data analysis of the GMRT observations (section 3.3.1) was performed using the Astronomical Image Processing Software package (AIPS). In section 3.3.2 I will briefly introduce the a-priori calibration procedure while in the section 3.3.3 I will describe the cleaning and the self-calibration procedure. Finally, in section 3.4 I will explain how the final images were obtained.

3.3.1 The GMRT observations

This thesis work is based on observations performed in 2004, from April 3th to 6th and on 9th April, at the frequencies of 610/235 MHz and 325 MHz. Unfortunately, among the many days of observations, only the observations taken on April 5th and

6th were good enough to be analysed, and for this reason the data of the dual band at 610/235 MHz were the only which provided a valuable scientific output. The set up used RR polarization at 610 MHz and LL polarization at 235 MHz. The bandwidths associated with these two frequencies are $\Delta\nu_{610\ \mathrm{MHz}}$=16 MHz and $\Delta\nu_{235\ \mathrm{MHz}}$=8 MHz, and the central frequencies were 614 MHz and 244 MHz respectively.

As we can see in table 3.1, the primary beam for each frequencies does not cover the wide sky area of the whole complex ($\approx 3\times2$ deg^2). For this reason, three pointings were used, centered on A3528N, A3528S and A3532. Furthermore, a fourth pointing was used during the observation but since it was centered on A3556, which belongs to the neighbourgh A3558 complex, it will not discussed here. The pointing coordinates are shown in table 3.2. During the observations we switched among the four pointings every $4-6$ minutes to ensure an u-v coverage as uniform as possible. The total time on each target was in the range of $\approx 50-70$ minutes.

Field (#)	RA (J2000)	DEC (J2000)	time (min)
1	$12^h54^m20^s$	$-29^d02^m30^s$	6
2	$12^h55^m00^s$	$-29^d40^m00^s$	4
3	$12^h56^m30^s$	$-30^d30^m00^s$	6
4	$13^h24^m00^s$	$-31^d38^m00^s$	6

Table 3.2: Coordinates of the pointings and the on-source times.

In addition to the four pointings, 3C286 and 3C283, the primary and secondary calibrator of the observation respectively (see table 3.3), have been observed. The former was observed at the beginning and at the end of the whole observing session while the latter was observed after the fourth pointing, as part as the duty cycle of 30 minutes.

calibrator	source's name	RA (J2000)	DEC (J2000)	time (min)
primary	3C286	$13^h31^m08.29^s$	$+30^d30^m32.96^s$	10
secondary	3C283	$13^h11^m39.33^s$	$-22^d16^m41.75^s$	6

Table 3.3: Coordinates of the primary and secondary calibrators and the on-source times.

3.3.2 Introduction to Calibration

The quantity measured by an interferometer is called visibility function, $V_{\mathrm{ij}}^{\mathrm{obs}}$, a complex number which is the true visibility V_{ij}^{true} multiplied by a gain factor, defining the antenna response:

$$V_{\mathrm{ij}}^{\mathrm{true}} = V_{\mathrm{ij}}^{\mathrm{obs}} G_{\mathrm{i}} G_{\mathrm{j}}\,. \tag{3.8}$$

G_{i} and G_{j} are the complex gains for the antenna i and j respectively which can be spitted into two terms, one for the amplitude and one for the phase. Hence, for a single gain we can write

$$G_{\mathrm{i}} = A_{\mathrm{i}} e^{i\theta_{\mathrm{i}}}\,. \tag{3.9}$$

The aim of the a-priori calibration is to find the values for G_{i} and G_{j} in order to determine $V_{\mathrm{ij}}^{\mathrm{true}}$ and, since they depend on the individual antenna or antenna pairs, the correction must be applied to the visibility data before they are Fourier inverted into an image. The initial amplitude and phase errors are corrected by means of a point-like source with constant and known flux, called primary calibrator, while the time-dependent phase fluctuations are tracked and corrected by a point-like source located in the sky near the target source, called secondary calibrator. The latter is usually observed many times during the observation because of the possible phase variation due to atmospheric turbolence.

3.3.3 Imaging and Self-Calibration

The initial image is given by the Fourier transformation of the a-priori calibrated fringe visibilities, and it is called dirty image I_{ν}^{D} because it includes secondary and grating lobes which can obscure the fainter sources or not resolve neighbouring ones. They are generated by the PSF as a result of the incomplete u-v plane sampling. For these reasons it is necessary to clean the image, in order to remove the image degradation brought by the PSF profile. This takes place with a iterative procedure known as *clean and restore*. The dataset of the target source is initially calibrated with the phase solutions of the secondary calibrator. They are measured in a nearby direction prior and after the scan on the target. The phase variation during the scan on the target can be corrected with *self-calibration* in which the model visibilities are taken from the Fourier transformation of the clean component. Now these two processes will be described in better detail.

The dirty image represents the sky brightness I_ν convolved with the point spread function (PSF) of the observation, called synthesized (or dirty) beam B:

$$\begin{aligned} I_\nu^{\mathrm{D}}(l,m) &= I_\nu * B \\ &= \int_{-\infty}^{\infty}\int_{-\infty}^{\infty} S(u,v)V(u,v)e^{2\pi i(ul+um)}dudv \end{aligned} \tag{3.10}$$

where $*$ denotes convolution and $B = \int_{-\infty}^{\infty}\int_{-\infty}^{\infty} S(u,v)e^{2\pi i(ul+um)}dudv$ is simply the Fourier transform of the (u,v) sampling of the observation S(u,v).

The images are sampled in pixels whose angular size that is a fraction of the half power beam width (HPBW). According to the Nyquist sampling theorem, the fraction is chosen to be less than 1/2. The image size depends on the sky surface brightness and on the field of viewof the instrument. In order to know the value of $I_\nu(l,m)$ and to obtain the clean image, we have to deconvolve equation 3.10. The clean algorithm provides one solution to this problem by representing the sky brightness distribution with a number of point sources. It is based on the Clark Clean, which proceeds as follows:

1. it finds the peak $(x_{\mathrm{i}}, y_{\mathrm{i}}, S_{\mathrm{i}})$ in the dirty image. At that position $(x_{\mathrm{i}}, y_{\mathrm{i}})$ it subtracts the dirty beam convolved by 10% (loop gain) of the peak intensity S_{i}. This step is known as Högbom Clean and this operation is repeted several times iteratively;

2. it calculates the FT of the point-like components found in the step 1), called clean components (CC), to obtain the model visibilities V^{mod};

3. it subtracts them to the observed visibilities and find $V^{\mathrm{obs}} - V^{\mathrm{mod}} = V^{\mathrm{res}}$;

4. it calculates the FT of residual visibilities V^{res} to obtain the residual dirty map;

5. the cycle is repeated from the step 1).

Since it calculates the FT of the δ-component, the advantage of Clark clean is that it works on the whole sky and not only on the image like the Högbom one does.

At the end of the cleaning, the algorithm proceedes with the restore procedure: each CC is convolved with the clean beam, that is the PSF with the main lobe only, and it is placed back into its position $(x_{\mathrm{i}}, y_{\mathrm{i}})$ on the residual image.

In AIPS, the clean and restore iterative method is carried out by the task IMAGR. Very important parameters that characterize this task are `imsize` and `cellsize`: they represent the size in pixels of the image and the angular size of each pixel in arcseconds, respectively. We chose a `cellsize` values of 1.2” for the 610 MHz observation and 2.5” for the 235 MHz one (the restoring beams at both fequencies are listed in table 3.7). Another important parameter is `niter` which indicates the numbers of iterations, namely clean components, before the cleaning stops.

Since each field of the A3528-A3532 complex (table 3.2) occupies a very large sky area both at 235 MHz and 610 MHz, it was necessary to use the wide-field cleaning: we divided each field into a number of facets and cleaned them in a parallel way, starting from that with the brightest source. In this case, we divide the map into 25 sub-fields, which cover a field of view in the range $\approx 1.5^2$ or 3^2 deg^2, for 610 MHz and 235 MHz respectively. Furthermore, we costrained the cleaning to circular boxes, to force the research of the CC only inside the selected sky area. This procedure is very useful both to focus the cleaning on the brightest sources, which have the most powerful sidelobes, and also to speed up the procedure.

After one clean cycle the image has still a lot of phase and amplitude errors. In order to correct them, a self-calibration procedure is necessary. As decribed in section 3.3.2, the standard calibration procedure is based on frequent observations of radio sources of known flux and position in order to determine the corrections for instrumental factors and weather conditions. The main problem of this procedure arises from atmospherical variations which can cause different delays to the wavefront before it reaches the telescopes. These variations generally have timescales shorter than that considered for the ordinary calibration, so the self-calibration represent a sort of second order approximation for the resolution of phase and amplitude errors.

The procedure begins with the phase self-calibration and it works by comparing the observed visibilities with the model produced by the clean components found by the task IMAGR. In fact, the observed phases are linked to the model ones according to the equation

$$\theta_{\mathrm{ij}}^{\mathrm{obs}} = \theta_{\mathrm{ij}}^{\mathrm{mod}} + \delta\theta_{\mathrm{i}} - \delta\theta_{\mathrm{j}} \tag{3.11}$$

where the correction factors $\delta\theta_{\mathrm{i}}$ and $\delta\theta_{\mathrm{j}}$ are progressively deleted considering a loop of three baselines formed from elemets i, j and k

$$\theta_{\rm ij}^{\rm obs} + \theta_{\rm jk}^{\rm obs} + \theta_{\rm ki}^{\rm obs} = \theta_{\rm ij}^{\rm true} + \theta_{\rm jk}^{\rm true} + \theta_{\rm ki}^{\rm true} \, . \tag{3.12}$$

This equation is called closure phase. Generally, more than one phase self-calibration is necessary to determine the correction that must be applied to obtain the final image. Each output file from this method becomes the new input file for a next clean cycle. When the convergence is reached, that is when phase solutions are centered on 0 with a very little scatter, the phase self-calibration is over and we can carry on the amplitude self-calibration to correct for residual amplitude errors. This procedure is quite similar to the previous one, but in this case four antennas are needed to define the closure amplitude relation:

$$\frac{\mid V_{\rm ij}^{\rm obs} \mid\mid V_{\rm kl}^{\rm obs} \mid}{\mid V_{\rm ik}^{\rm obs} \mid\mid V_{\rm jl}^{\rm obs} \mid} = \frac{\mid V_{\rm ij}^{\rm true} \mid\mid V_{\rm kl}^{\rm true} \mid}{\mid V_{\rm ik}^{\rm true} \mid\mid V_{\rm jl}^{\rm true} \mid} \, . \tag{3.13}$$

Both the phase and amplitude self-calibration are performed by the task CALIB. One of its most important parameters is `solint` which determines the time interval, expressed in minutes, over which the correction computed. The `solint` values we chose are: 2 minutes (twice), 1 minute and 16 second, i.e. the integration time of the observation, for phase self-calibration; 600 and 15 minutes, namely the whole observation time and the time of each scan respectively, for amplitude and phase self-calibration.

A very important step during the cleaning and self-calibration procedure is the data editing. It consists on deleting bad data and it acts at two different steps of analysis. After the first cycle of phase self-calibration, it is useful to check the plot of the amplitude of visibilities versus time. In almost every case, the presence of bad data was clear, for each antenna, at the beginning of each scan: these are probabily due to adjustments of the instrument during the transition from one pointing to the others. In this case, the editing procedure has been carried out with the task WIPER. A second editing step was made before the amplitude self-calibration, thanks to the combination of tasks UVPRM and UVLIN: the first gives us the noise for each channel while the second deletes the data whose noise exceedes a given threshold. The reason for that is based on the idea that if a baseline shows very high residual in one or more channels then we can consider it contaminated and hence it should be flagged. We chose to ignore the data whose residual flux is above 10σ.

Finally, at the very end of these procedures, we checked the validity of the model with task VPLOT and SNPLT: the first compares our model to the real data while the second gives us the final amplitude and phase solutions of the calibration procedure.

3.4 Final images

The cleaning and self-calibration procedures were made for each dataset, that is the three pointings at both 235 and 610 MHz for the two days. However, at the end of these procedures we only have, for each of them, the best images for each 25 sub-fields. For this reason, we use the task FLATN several times, to obtain the final mosaic with the best noise possible (figures 3.6 and 3.7; in figures 3.8 and 3.9 the zooms on the single fields are presented).

To obtain the final images we first combined the 25 sub-fields together to produce the image of the whole field of view of each pointing at each frequency. Then, for each pointing we combined the dataset of the two different days, to improve the noise by a factor $\sqrt{2}$ (tables 3.4 and 3.5).

Field (#)	noise day 1 (mJy/beam)	noise day 2 (mJy/beam)	noise comb (mJy/beam)
1	1.41	1.63	1.26
2	1.32	1.64	1.19
3	0.93	1.02	0.76

Table 3.4: Noise of the three pointings at 235 MHz for both days and for their combination.

Field (#)	noise day 1 (mJy/beam)	noise day 2 (mJy/beam)	noise comb (mJy/beam)
1	0.28	0.29	0.21
2	0.16	0.17	0.12
3	0.14	0.14	0.14

Table 3.5: Noise of the three pointings at 610 MHz for both days and for their combination.

Then we make the final mosaic. Each telescope in the synthesis array has its own beam response, the so called primary beam, hence the image we have produced is the sky multiplied by the primary beam. The shape of the primary beam can be approximated by a gaussian, so the sensitivity of our observations decreases as we move away from the pointing center. To correct for this we divided the image by the primary beam. In doing this, we assume that the primary beam is the same for each telescope, and that it is circularly symmetric. The so called primary beam correction is done in AIPS using the task PBCOR that uses an eighth order polynomial to fit the beam:

$$1 + \frac{a}{10^3}x^2 + \frac{b}{10^7}x^4 + \frac{c}{10^{10}}x^6 + \frac{d}{10^{13}}x^8 \tag{3.14}$$

where x is the distance from the pointing position in arcminutes multiplied by the frequency in GHz while a, b, c and d are the coefficients which depend on the observation frequency, as we see in table 3.6.

frequency (ν) (MHz)	a	b	c	d	HPBW (arcmin)
235	-3.366	46.159	-29.963	7.529	118.5
610	-3.486	47.749	-35.203	10.399	44.4

Table 3.6: PBCOR parameters for GMRT.

As a consequence of the primary beam correction, the image noise radially increases, but the flux densities of each source are now corrected. At this point we use again the task FLATN to produce the final mosaic for both frequencies.

The main characteristics of the mosaics at both frequencies (convolution size, position angle and mean noise) are shown in table 3.7.

frequency (ν) (MHz)	convolution size (Θ) (arcsec^2)	position angle (degrees)	mean noise (mJy/beam)
235	16.3×11.9	9.5	1.07
610	6.8×4.7	29	0.16

Table 3.7: Main characteristics of the mosaics at 610 MHz and 235 MHz; the mean noises are taken from the image before applying the primary beam correction.

Images of the A3558 complex

The data reduction of the A3558 cluster complex was performed by Venturi et al. (in preparation) following the same approach described in the previuos section. Here, the final image at 325 MHz (figures 3.10) and the zooms on the single fields which will be used in this thesis (figures from 3.11 to 3.13) are presented. The 325 MHz observations presented here are part of another proposal and were taken in 2013.

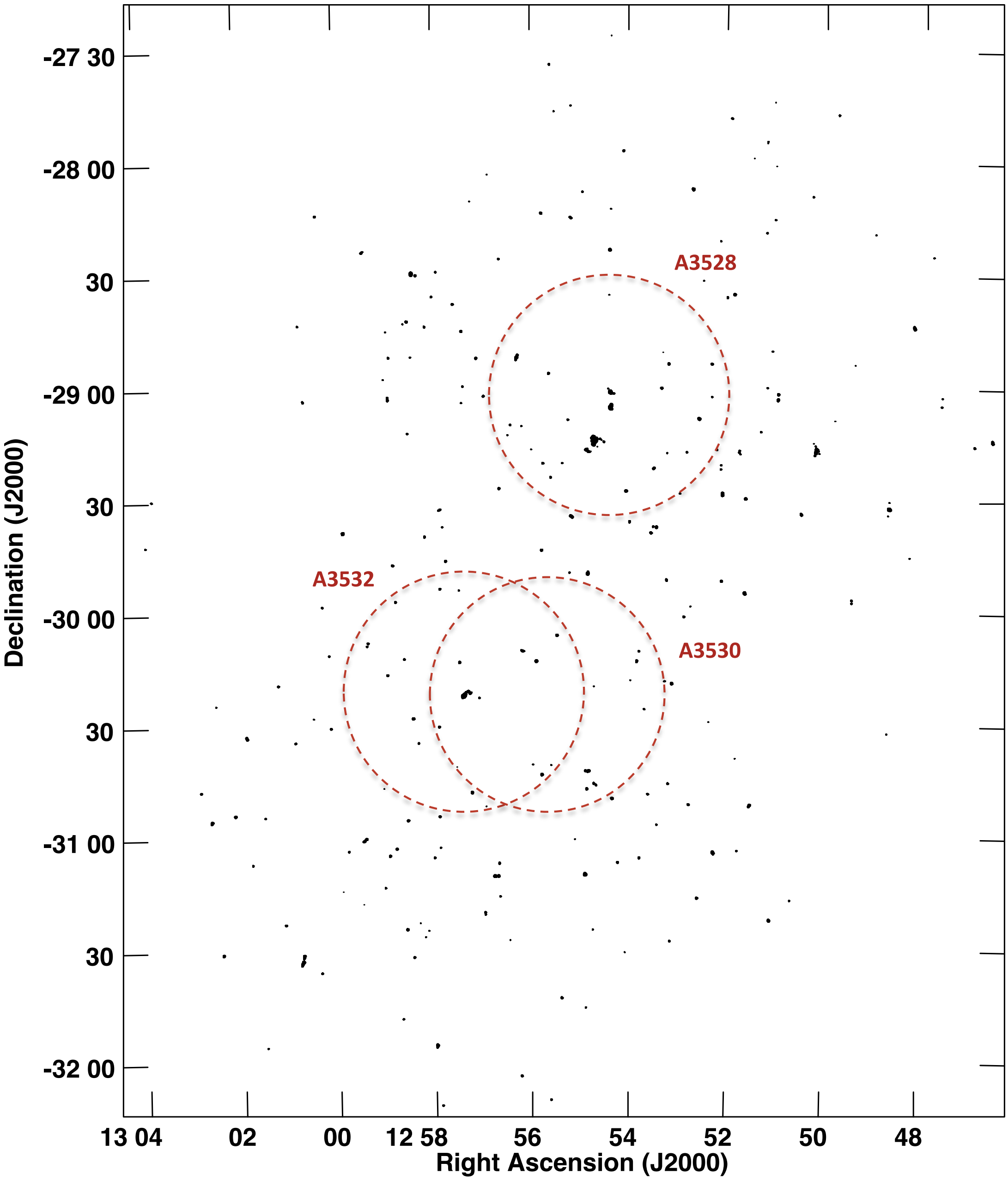

Figure 3.6: Radio contours of the A3528 complex at 235 MHz. The restoring beam is 16.3 × 11.9 arcsec^2, PA equal to 9.5° and the rms ≈ 1.07 mJy/beam. The levels are $7\sigma\times(\pm1, 2, 4, 8, 16, 32, 128)$. The dotted circles represent their Abell radii.

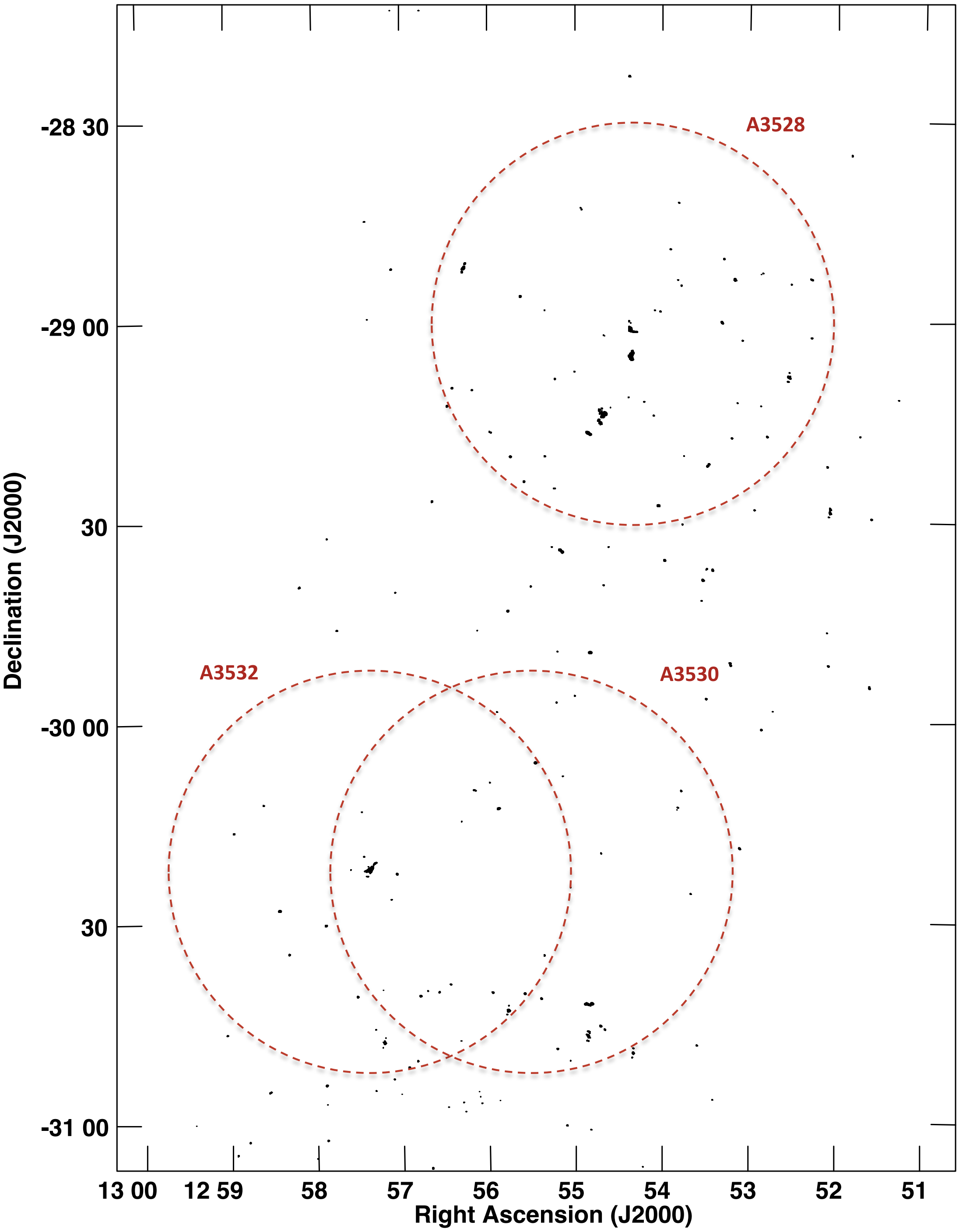

Figure 3.7: Radio contours of the A3528 complex at 610 MHz. The restoring beam is 6.8×4.7 arcsec^2, PA equal to 29° and the rms ≈ 0.16 mJy/beam. The levels are $7\sigma\times(\pm1, 2, 4, 8, 16, 32, 128)$. The dotted circles represent their Abell radii.

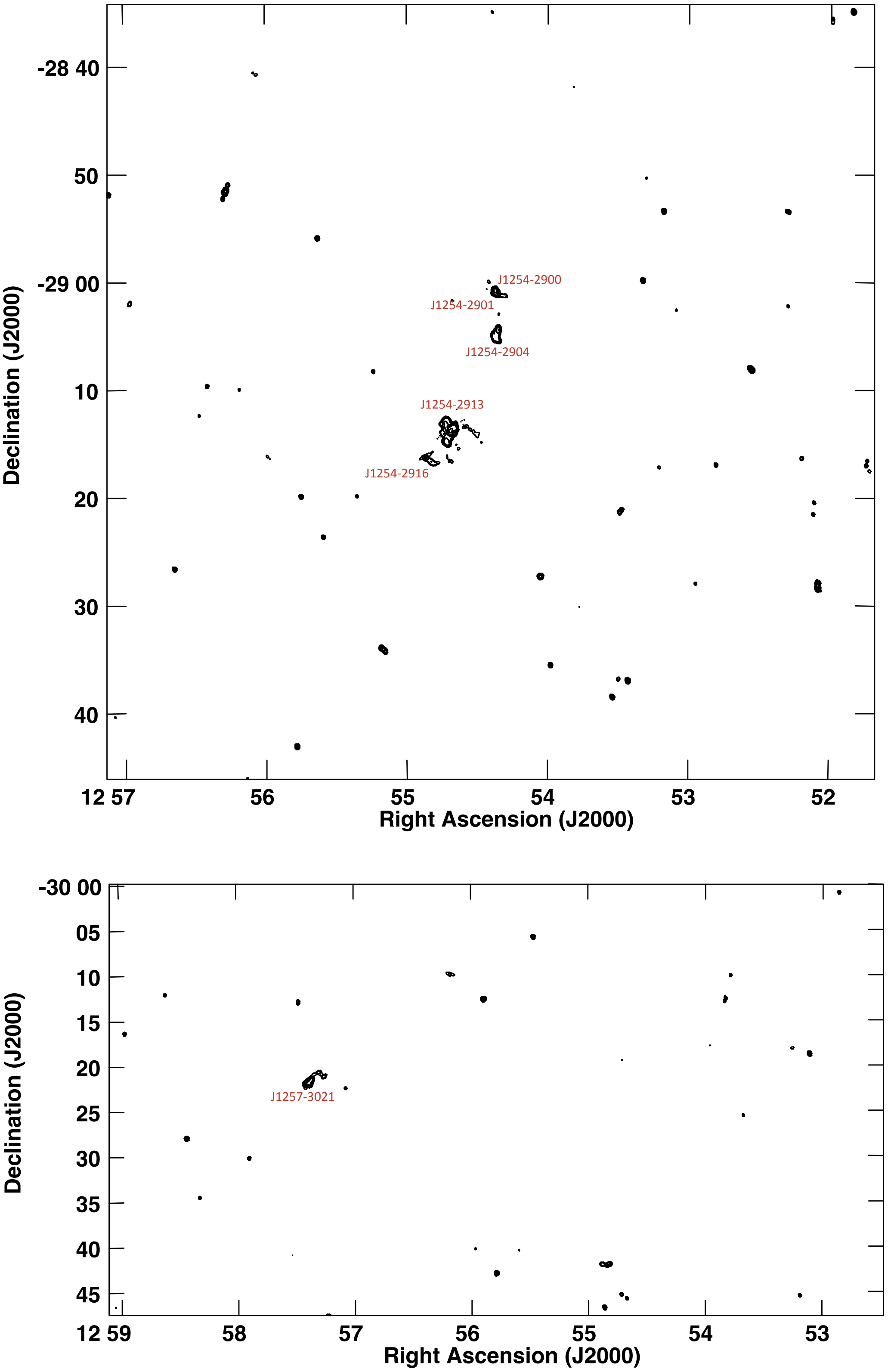

Figure 3.8: *Top panel*: radio contours of the A3528 cluster at 235 MHz. The mean noise of the field is rms ≈ 1.26 mJy/beam. *Bottom panel*: radio contours of the A3530-A3532 pair of clusters at 235 MHz. The mean noise of the field is rms ≈ 0.76 mJy/beam. The levels are $7\sigma\times(\pm1, 2, 4, 8, 16, 32, 128)$.

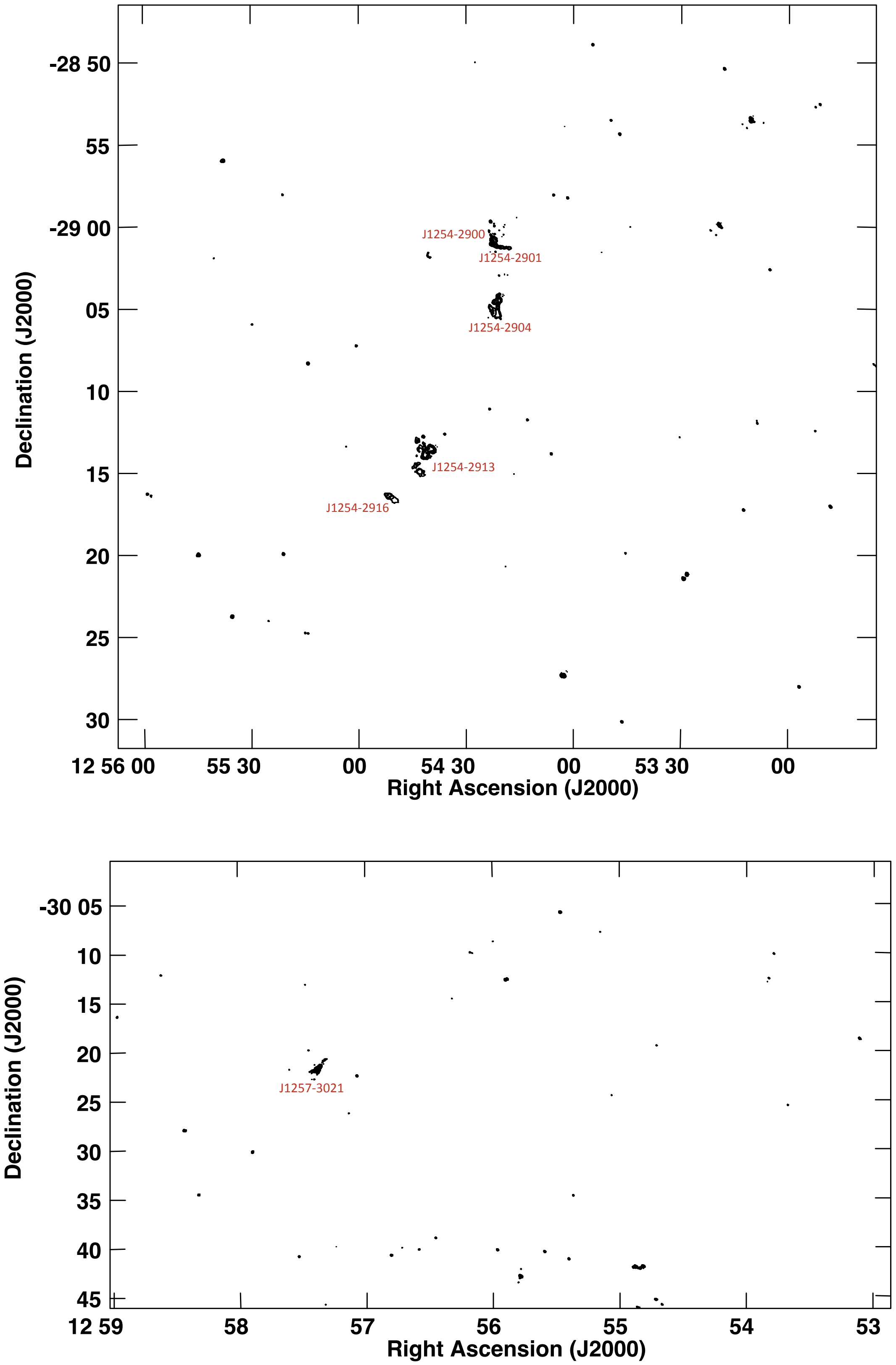

Figure 3.9: *Top panel*: radio contours of the A3528 cluster at 610 MHz. The mean noise of the field is rms ≈ 0.21 mJy/beam. *Bottom panel*: radio contours of the A3530-A3532 pair of clusters at 610 MHz. The mean noise of the field is rms ≈ 0.14 mJy/beam. The levels are $7\sigma\times(\pm1, 2, 4, 8, 16, 32, 128)$.

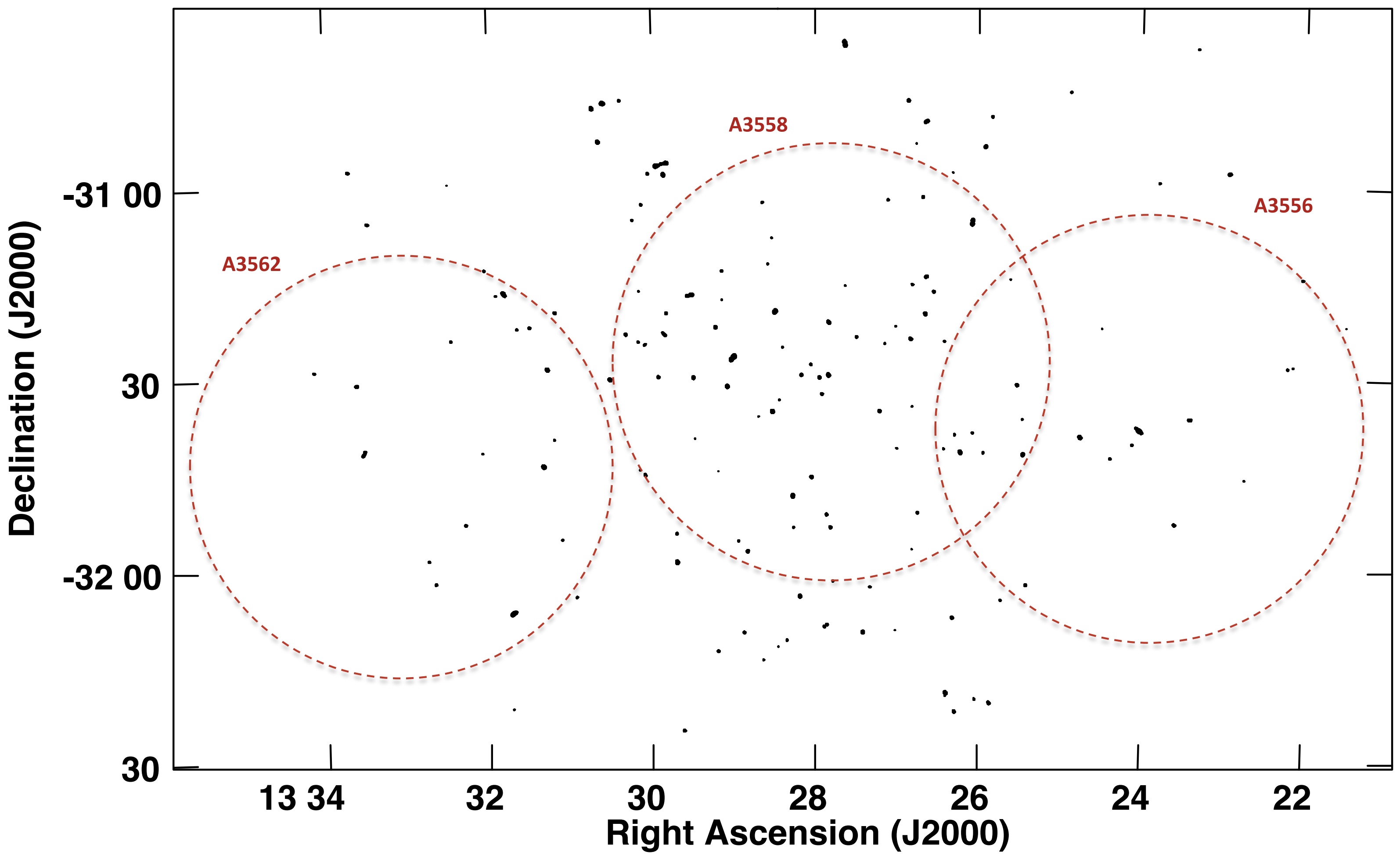

Figure 3.10: Radio contours of the A3558 complex at 325 MHz. The restoring beam is 14.05×9.53 arcsec^2, PA equal to 18.39° and the rms ≈ 0.95 mJy/beam. The levels are $7\sigma\times(\pm1, 2, 4, 8, 16, 32, 128)$. The dotted circles represent their Abell radii (Venturi et al., in preparation).

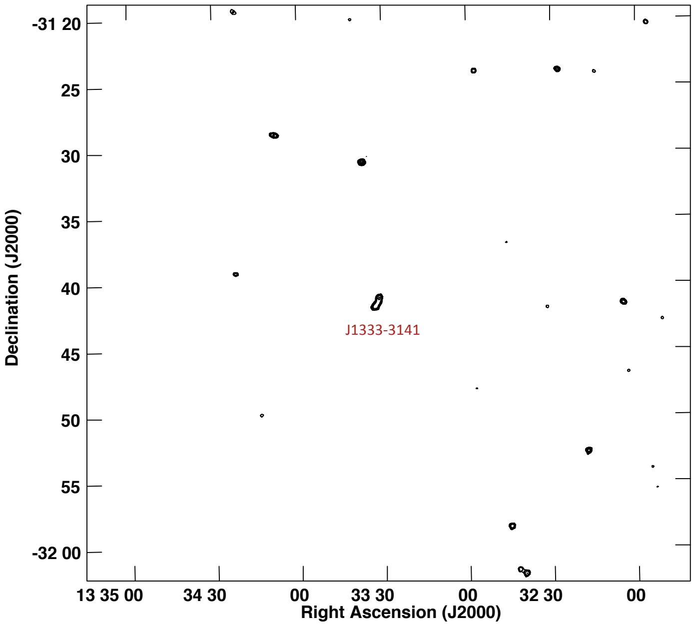

Figure 3.11: Radio contours of the A3562 cluster at 325 MHz. The mean noise of the field is rms ≈ 0.08 mJy/beam.The levels are $7\sigma\times(\pm1, 2, 4, 8, 16, 32, 128)$.

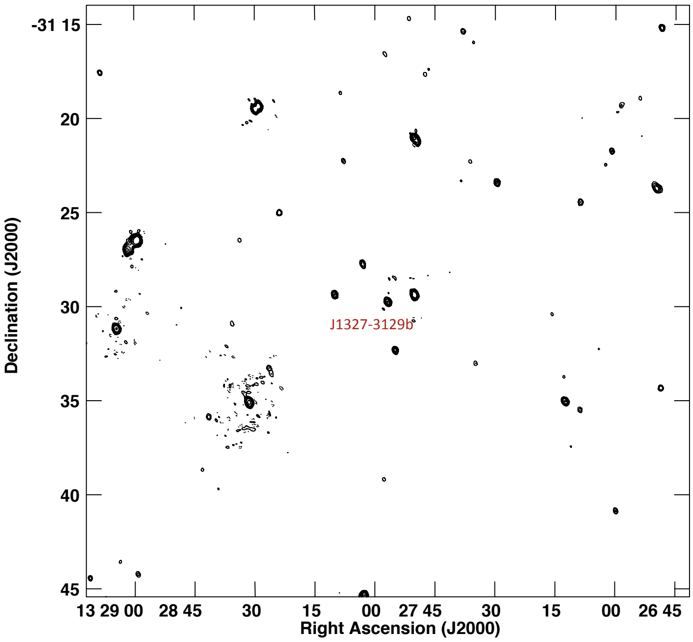

Figure 3.12: Radio contours of the A3558 cluster at 325 MHz. The mean noise of the field is rms ≈ 0.16 mJy/beam.The levels are $7\sigma\times(\pm1, 2, 4, 8, 16, 32, 128)$.

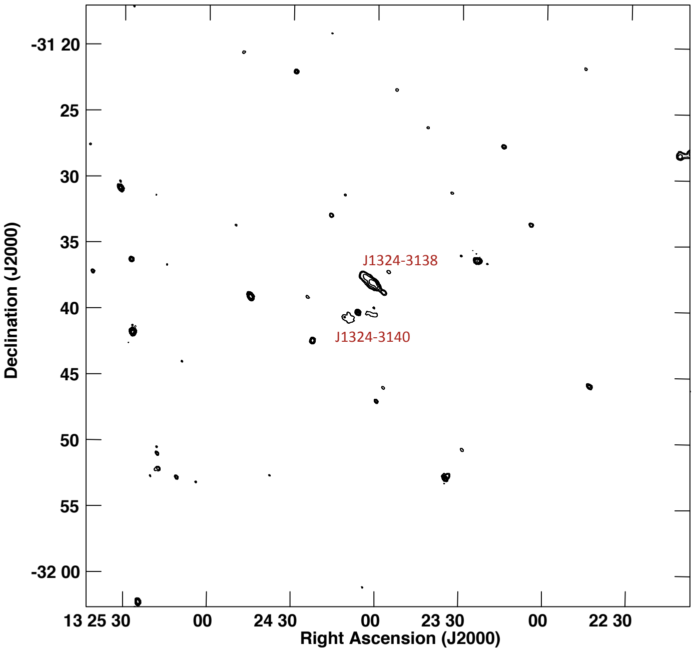

Figure 3.13: Radio contours of the A3556 cluster at 325 MHz. The mean noise of the field is rms ≈ 0.08 mJy/beam.The levels are $7\sigma\times(\pm1, 2, 4, 8, 16, 32, 128)$.

CHAPTER 4

SAMPLE OF THE EXTENDED RADIO GALAXIES

From the point of view of the radio galaxy content, the two chains of the Shapley Concentration Core, the A3528 and A3558 complexes, are completely different (chapter 2). The purpose of this thesis is to address the origin of such difference, and discuss it in the framework of the dynamical state of each complex. As described in chapter 2 the A3558 complex is thought to have undergone its first core-core encounter, while the A3528 one is considered a “younger” structure, where only the northern and the southern components of A3528 are interacting (Bardelli et al. 1998, 2001).

In this chapter, I will introduce the sample of extended radio galaxies, whose main optical and radio properties are summarized in table 4.1. Then, the spectral properties will be presented and discussed in the next chapter. In particular, the images obtained by the GMRT data reduction presented in chapter 3 are combined with previous proprietary data obtained with the Austalia Telescope Compact Array (ATCA) and the Very Large Telescope (VLA), for a multiband spectral study in the frequency range 235 MHz ÷ 8.4 GHz.

4.1 Radio galaxies in the A3528 complex

The A3528 complex hosts six extended radio galaxies. Three of them are associated with the BCGs in A3528N (J1254-2900) and A3532 (J1257-3021). Moreover we found an extended radio galaxy, J1254-2904 at the outskirts of the two X-ray peaks of A3528 and two tailed radio galaxies, one just south of the BCG in A3528N (J1254-2901) and the other just south of the BCG in A3528S (J1254-2016).

4.1.1 J1254-2900 and J1254-2901

Low frequency images

J1254-2900 and J1254-2901 are placed at the center of A3528N. The radio-optical overlay is shown in figure 4.1. The radio contours at 235 and 610 MHz are displayed in figure 4.2 (top and bottom, respectively). Due to the large resolution of the observation at 235 MHz (16.3×11.9 arcsec^2), the two radio galaxies are not individually resolved at this frequency. Nevertheless, their different morphologies are clearly seen in the image at 610 MHz. J1254-2900 coincides with the optical central dominant galaxy (BCG) of A3528N, and it looks like a mini double radio galaxy (figure 4.1). Based on its radio power (table 4.1), it is classified as a FRI/FRII.

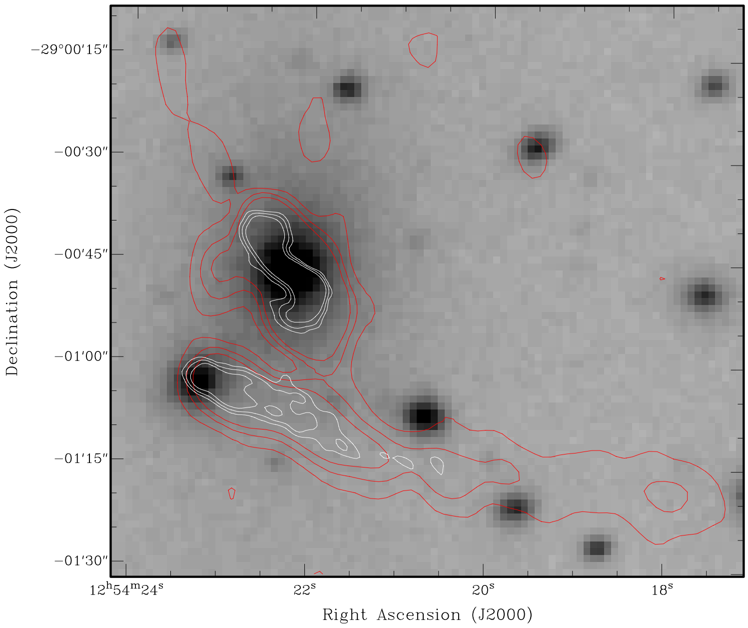

Figure 4.1: Radio-optical overlay of J1254-2900 and J1254-2901 at 610 MHz (red) and 8.4 GHz (white). The levels are $3\sigma\times(2, 8, 16)$ at 610 MHz and $3\sigma\times(1, 2, 4, 8)$ at 8.4 GHz.

J1254-2901 is located southward of the BCG and it is clearly a head-tail radio galaxy, whose angular size is approximately 1.3 arcmin at 610 MHz (80 kpc at source redshift). A possible explanation for the long size of the tail could be that the effect of strong effect of the ram pressure as consequence of the radio galaxy motion into a very dense medium. We note that the head-tails are usually located away from the cluster center, but projection effects could play a role.

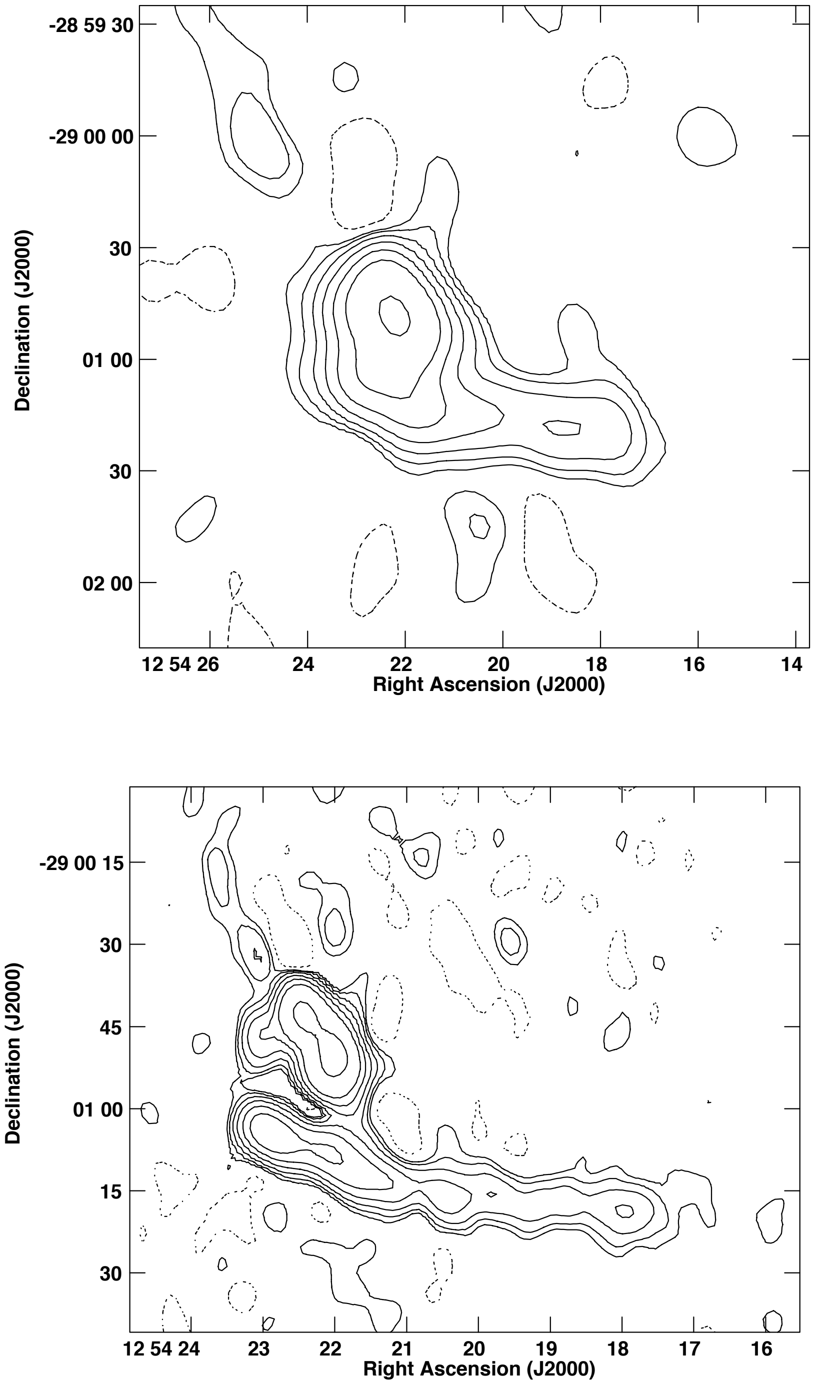

Figure 4.2: J1254-2900 and J1254-2901. *Top panel*: radio contours at 235 MHz; the restoring beam is 16.3×11.9 arcsec^2, PA = 9.5° and rms ≈ 1.26 mJy/beam. *Bottom panel*: radio contours at 610 MHz; the restoring beam is 6.8×4.7 arcsec^2, PA = 29° and rms ≈ 0.21 mJy/beam. The levels are $3\sigma\times(\pm1, 2, 4, 8, 16, 32, 128)$ mJy/beam.

High frequency images

The two radio galaxies were observed also at high frequencies with the ATCA (at 1.4 and 2.4 GHz) and the VLA (at 8.4 GHz). The radio contours at 2.4 and 8.4 GHz are displayed in figure 4.3. The lenght of the tail of J1254-2901 is much shorter at high frequencies with respect to figure 4.2, likely due to combination of a steep spectral index (typical in head-tail radio galaxies) and a decreased sensitivity to low surface brightness emission. At 8.4 GHz, J1254-2900 is characterized by an S shape, while the tail of J1254-2901 becomes slightly resolved perpendicularly to the tail direction. It is interesting to note that in both sources the core remains unresolved also at these high frequencies.

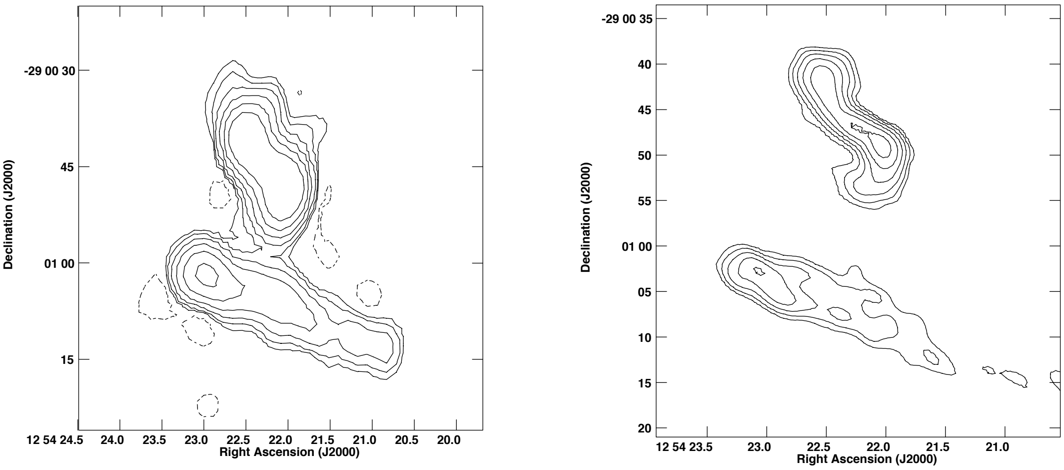

Figure 4.3: J1254-2900 and J1254-2901. *Left panel*: radio contours at 2.4 GHz; the restoring beam is 5.73×3.62 arcsec^2, PA = 1.99° and rms $\approx$ 0.13 mJy/beam. *Right panel*: radio contours at 8.4 GHz; the restoring beam is 2.76×1.59 arcsec^2, PA = 49.82° and rms $\approx$ 0.05 mJy/beam. The levels are $3\sigma \times (\pm 1, 2, 4, 8, 16, 32, 128)$ mJy/beam.

4.1.2 J1254-2904

Low frequency images

J1254-2905 belongs to A3528N, and it is located at $\approx$ 4 arcmin south-west of from the cluster center (i.e. $\approx$ 250 kpc, at the radio galaxy redshift). The radio-optical overlay is shown in figure 4.4. According to Schindler (1996), the radio galaxy position coincides with the region where a shock front due to the interaction between A3528N and A3528S is expected. The radio contours at 235 and 610 MHz are plotted in figure 4.5 (top and bottom, respectively) and suggest a narrow-angle tail morphology. However, the two bending tails are not individually resolved at 235 MHz, while at 610 MHz they become slightly visible.

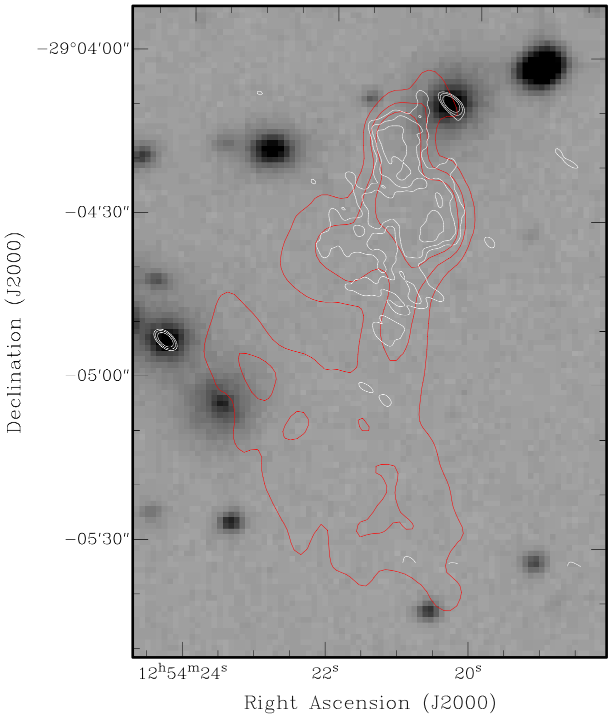

Figure 4.4: Radio-optical overlay of J1254-2904 at 610 MHz (red) and 8.4 GHz (white). The levels are $3\sigma\times(2, 8, 16)$ at 610 MHz and $3\sigma\times(1, 2, 4, 8)$ at 8.4 GHz.

High frequency images

The radio contours at high frequencies with the ATCA (at 1.4 and 2.4 GHz) and the VLA (at 8.4 GHz) confirm the morphological classification of the radio galaxy. As for the 610 MHz image, the radio contours at 2.4 and 8.4 GHz (figure 4.6) show that the radio galaxy is asymmetric with two tails bent in the south direction. The observation at 8.4 GHz (right panel) shows the presence of the radio core in the northern edge of the radio emission at the position of an optically bright galaxy (figure 4.4).

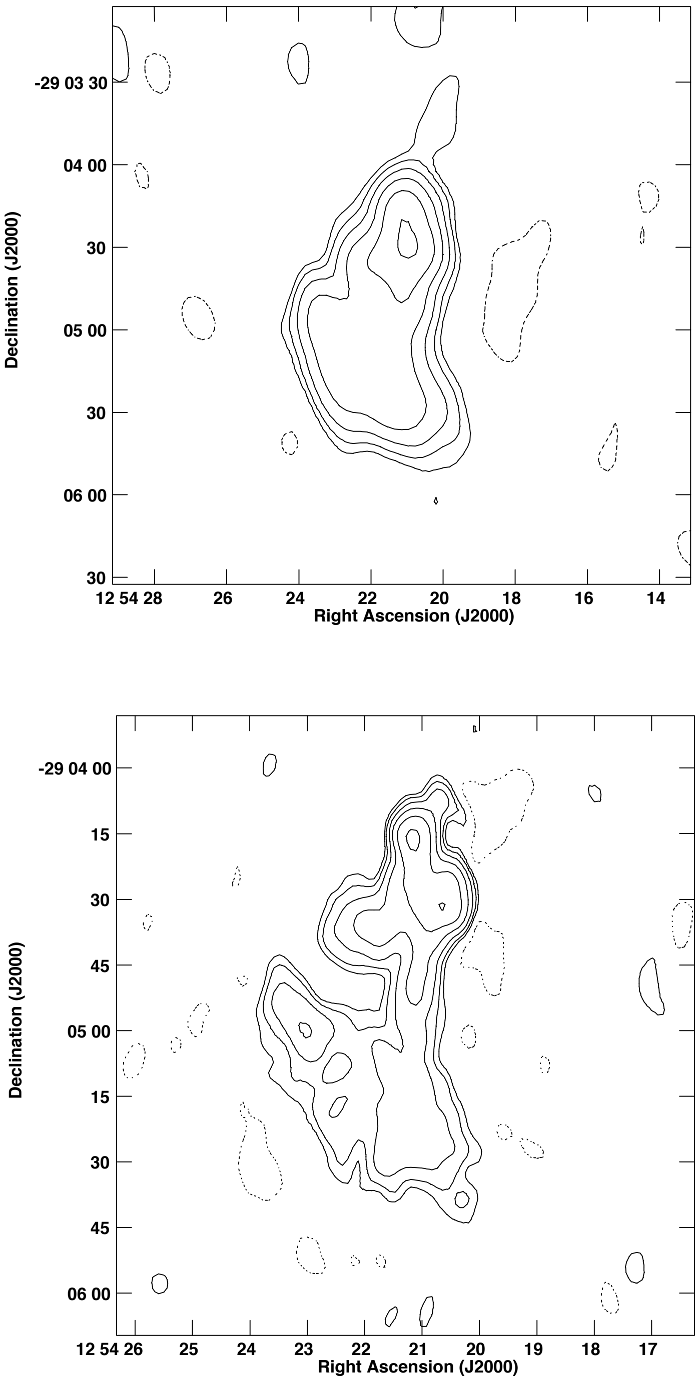

Figure 4.5: J1254-2904. *Top panel*: radio contours at 235 MHz; the restoring beam is 16.3 × 11.9 arcsec^2, PA = 9.5° and rms ≈ 1.26 mJy/beam. *Bottom panel*: radio contours at 610 MHz; the restoring beam is 6.8 × 4.7 arcsec^2, PA = 29° and rms ≈ 0.21 mJy/beam. The levels are $3\sigma\times(\pm1, 2, 4, 8, 16, 32, 128)$ mJy/beam.

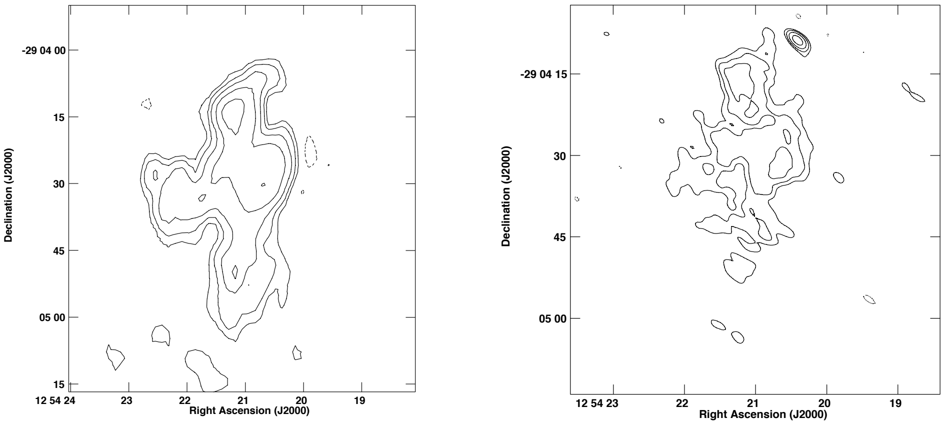

Figure 4.6: J1254-2904. *Left panel*: radio contours at 2.4 GHz; the restoring beam is 5.73 × 3.62 arcsec^2, PA = 1.99° and rms ≈ 0.13 mJy/beam. *Right panel*: radio contours at 8.4 GHz; the restoring beam is 2.83 × 1.54 arcsec^2, PA = 48.58° and rms ≈ 0.05 mJy/beam. The levels are $3\sigma\times(\pm1, 2, 4, 8, 16, 32, 128)$ mJy/beam.

4.1.3 J1254-2913 and J1254-2916

Low frequency images

J1254-2913 and J1254-2916 are located at the center of A3528S. The radio-optical overlay is shown in figure 4.7. The radio contours at 235 and 610 MHz are displayed in figure 4.8 (top and bottom, respectively). J1254-2913 is associated with the BCG and the images at these two frequencies show that it is formed by a strong component which is surronded by diffuse emission. The brighter part could be classified as a wide-angle tail radio galaxy.

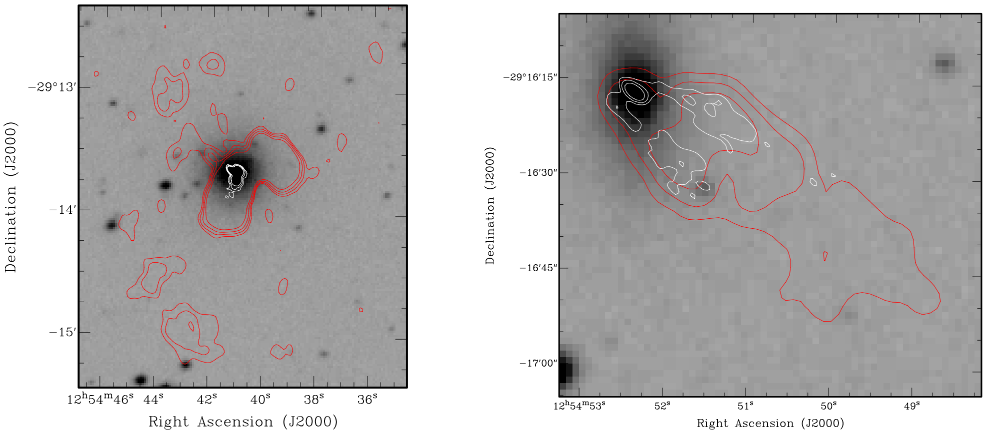

Figure 4.7: Radio-optical overlay of J1254-2913 (left panel) and J1254-2916 (right panel) at 610 MHz (red) and 8.4 GHz (white). The levels are $3\sigma\times(1, 2, 8, 16)$ at 610 MHz and $3\sigma\times(1, 2, 4, 8)$ at 8.4 GHz.

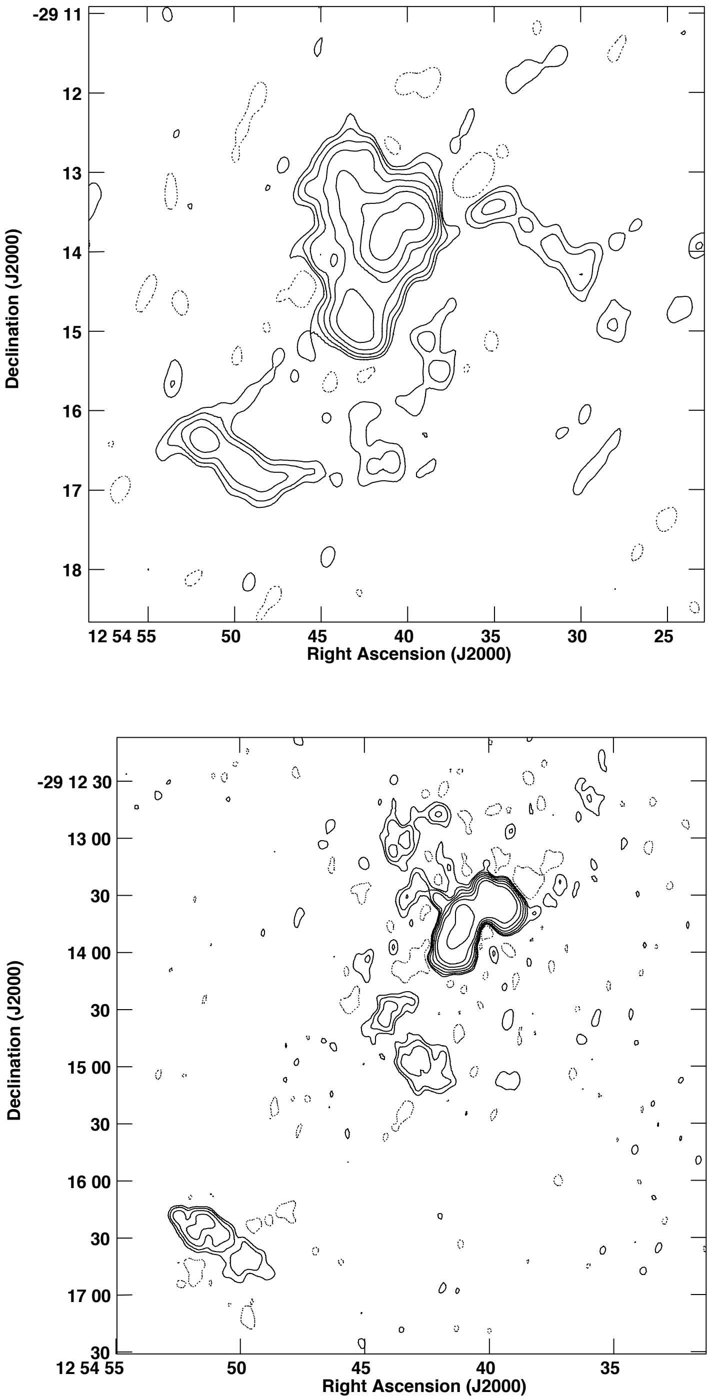

Figure 4.8: J1254-2913 and J1254-2916. *Top panel*: radio contours at 235 MHz; the restoring beam is 16.3 × 11.9 arcsec^2, PA = 9.5° and rms ≈ 1.26 mJy/beam. *Bottom panel*: radio contours at 610 MHz; the restoring beam is 6.8 × 4.7 arcsec^2, PA = 29° and rms ≈ 0.21 mJy/beam. The levels are $3\sigma\times(\pm1, 2, 4, 8, 16, 32, 128)$ mJy/beam.

In both images, the radio emission is bent in the south-west direction, which could indicate the direction of motion of the BCG. The surrounding diffuse emission of J1254-2913 is much better visible at 235 MHz, while it is partially resolved out at 610 MHz. Its properties will be discussed in chapter 5.

J1254-2916 is another head-tail associated with a galaxy south of the BCG. At low frequencies, the tail is considerably longer than at high frequencies and it is pointing to almost the same direction of the J1254-2913 ones.

High frequency images

The high frequency images of the two radio galaxies are plotted in figure 4.9, while the zooms on each radio galaxy are dislpayed in 4.10, in order to properly show their morphologies. The ATCA observation at 2.4 GHz is displayed in figure 4.10 (left panels). On the top, the radio contours of J1254-2913 show the compact component of the radio galaxy, confirming its wide-angle tailed morphological classification. At the bottom, the radio contours of J1254-2916 reveal a faint radio core and show two almost simmetric peaks in the tail. The VLA observation at 8.4 GHz is displayed on the right panel of the same figure. At this frequency, we probably see the inner region of J1254-2913 (top panel). On the contrary, the radio core of J1254-2916 (bottom panel) becomes evident thanks to its flat spectrum (chapter 5), as well as the two strongly bent tails.

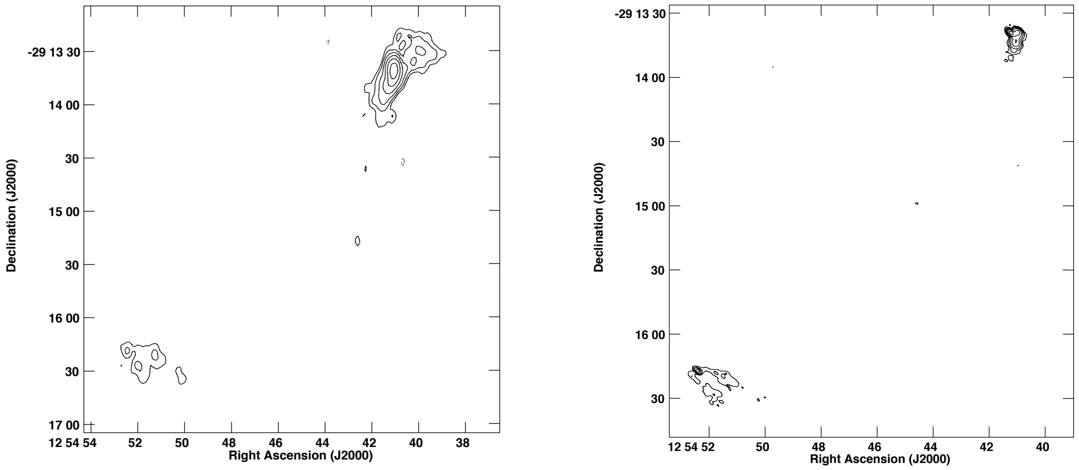

Figure 4.9: J1254-2913 and J1254-2916. *Top panel*: radio contours at 2.4 GHz; the restoring beam is 6.59 × 3.58 arcsec^2, PA = 2.28° and rms ≈ 0.11 mJy/beam. *Bottom panel*: radio contours at 8.4 GHz; the restoring beam is 2.28 × 1.46 arcsec^2, PA = 51.58° and rms ≈ 0.12 mJy/beam. The levels are $3\sigma\times(\pm1, 2, 4, 8, 16, 32, 128)$ mJy/beam.

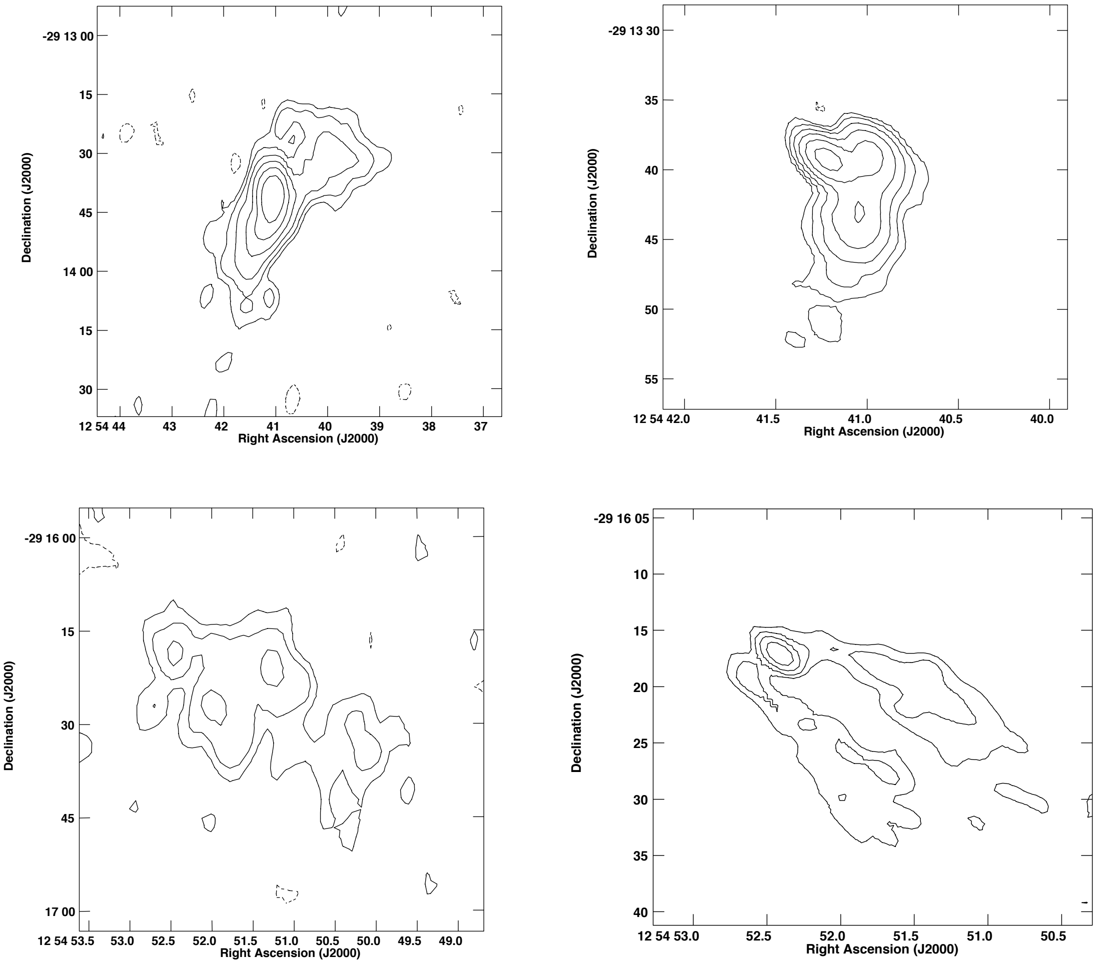

Figure 4.10: Zoom on the individual radio galaxies at 2.4 GHz (left) and at 8.4 GHz (right) . J1254-2913 is plotted on the top, while J1254-2916 on the bottom. The contours levels are the same of those in the previous figure, but the noises are measured near each radio galaxy, at each frequency. The former has $\mathrm{rms}_{2.4\ \mathrm{GHz}} \approx 0.10$ and $\mathrm{rms}_{8.4\ \mathrm{GHz}} \approx 0.05$. The latter has $\mathrm{rms}_{2.4\ \mathrm{GHz}} \approx 0.07$ and $\mathrm{rms}_{8.4\ \mathrm{GHz}} \approx 0.05$.

4.1.4 J1257-3021

Low frequency images

J1257-3021 is associated with one of the two nuclei of the dominant dumb-bell of the A3532 cluster (figure 4.11).

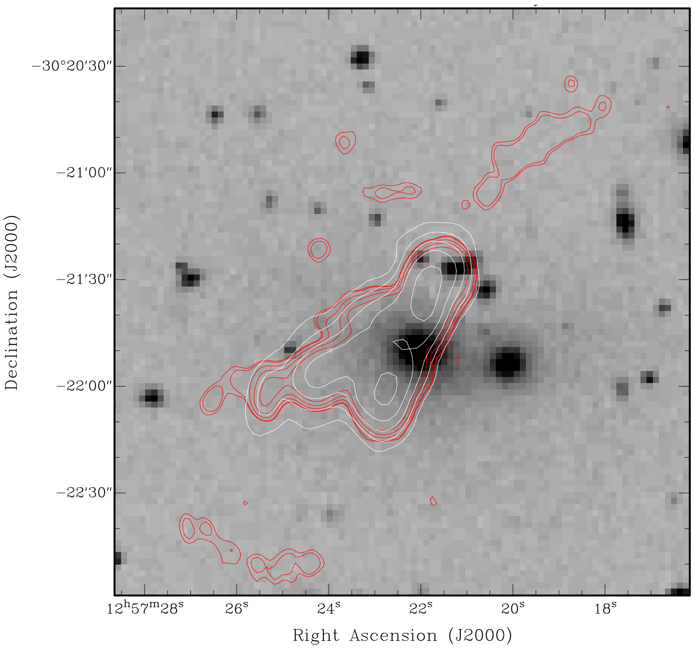

Figure 4.11: Radio-optical overlay of J1257-3021 at 610 MHz (red) and 1.4 GHz (white). The levels are $3\sigma\times(1, 2, 4, 8, 16)$ at 610 MHz and $3\sigma\times(1, 2, 4, 8)$ at 1.4 GHz.

As for J1254-2913, the low frequency contours show that J1257-3021 is formed by a strong component surronded by diffuse emission, which extendes in the north-east direction and is particularly clear in the image at 235 MHz (top panel in figure 4.12). The 610 MHz image (bottom panel in figure 4.12) suggests that the brightest part of the radio galaxy can be interpreted as a wide-angle tailed morphology. It is classified as a FRI/FRII radio galaxy, whose radio power (table 4.1) is almost equal to the transition break according to Fanaroff & Riley (1974). The tails are slightly asymmetric and bent towards north-east direction, suggesting a motion towards the nearby A3530 cluster.

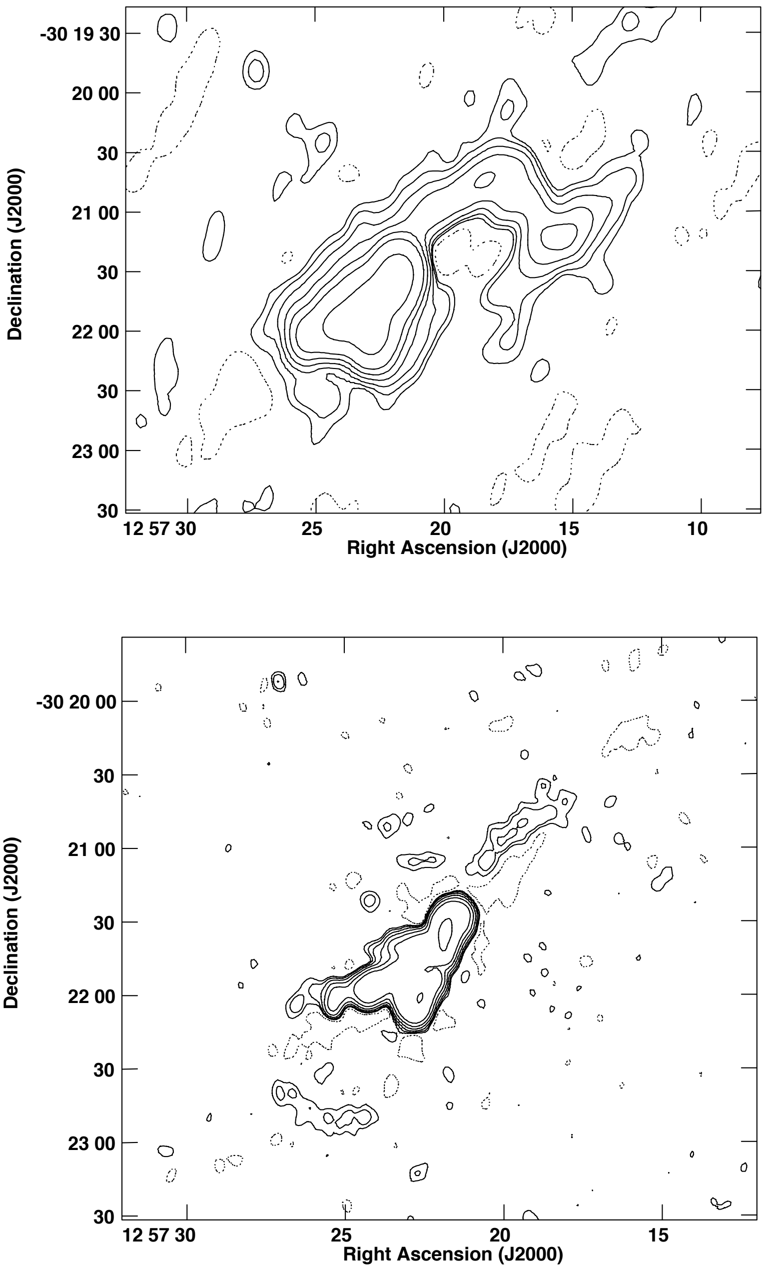

Figure 4.12: J1257-3021. *Top panel*: radio contours at 235 MHz; the restoring beam is 16.3 × 11.9 arcsec^2, PA = 9.5° and rms ≈ 0.76 mJy/beam. *Bottom panel*: radio contours at 610 MHz; the restoring beam is 6.8 × 4.7 arcsec^2, PA = 29° and rms ≈ 0.14 mJy/beam. The levels are $3\sigma\times(\pm1, 2, 4, 8, 16, 32, 128)$ mJy/beam.

High frequency image

J1257-3021 was observed also with the ATCA telescope, at 1.4 and 2.4 GHz. In figure 4.13, the image of the radio galaxy at 1.4 GHz is shown. It confirms the morphology of the brightest part of the radio galaxy presented at 610 MHz, while the diffuse emission is only barely detected.

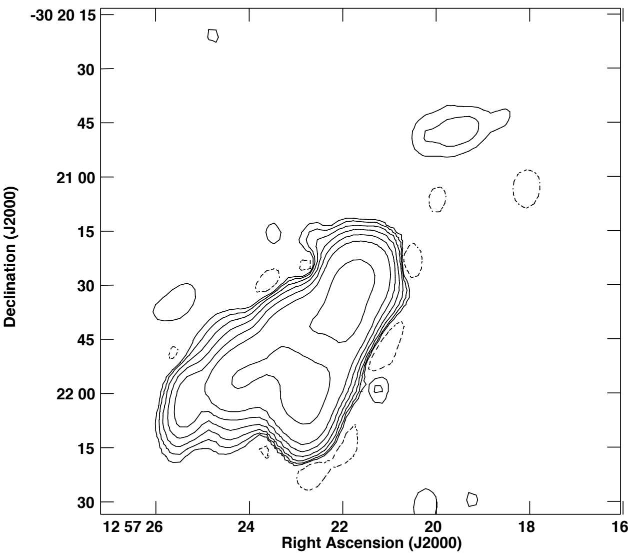

Figure 4.13: Radio contours at 1.4 GHz of J1257-3021; the restoring beam is 5.7×3.5 arcsec^2, PA = $1°$ and rms $\approx$ 0.11 mJy/beam. The levels are $3\sigma \times (\pm 1, 2, 4, 8, 16, 32, 128)$ mJy/beam.

4.2 Radio galaxies in the A3558 complex

The radio proprieties of the BCGs in the clusters of the A3558 complex are remarkably different from those described in section 4.1. Extended radio emission is mainly associated with faint galaxies, in the form of head-tailed sources. In this field we found two radio galaxies in A3556 (J1324-3138 and J1324-3140) and one in both A3558 and A3562 (J1327-3129b and J1333-3141, respectively). Only J1324-3140 and J1327-3129b are associated with the central dominant galaxies.

4.2.1 J1324-3138 and J1324-3140

Low frequency images

J1324-3138 and J1324-3140 belong to the A3556 cluster. J1324-3140 is associated with the optical central dominant galaxy and its morphology is peculiar. At high frequencies (figure 4.15) this radio galaxy shows only a compact component. The low frequency observations show that J1324-3140 has a pair of symmetric lobes, which are well visible at 235 and 327 MHz (top panels in figure 4.14) and become weaker at 610 MHz (bottom panel figure 4.14).

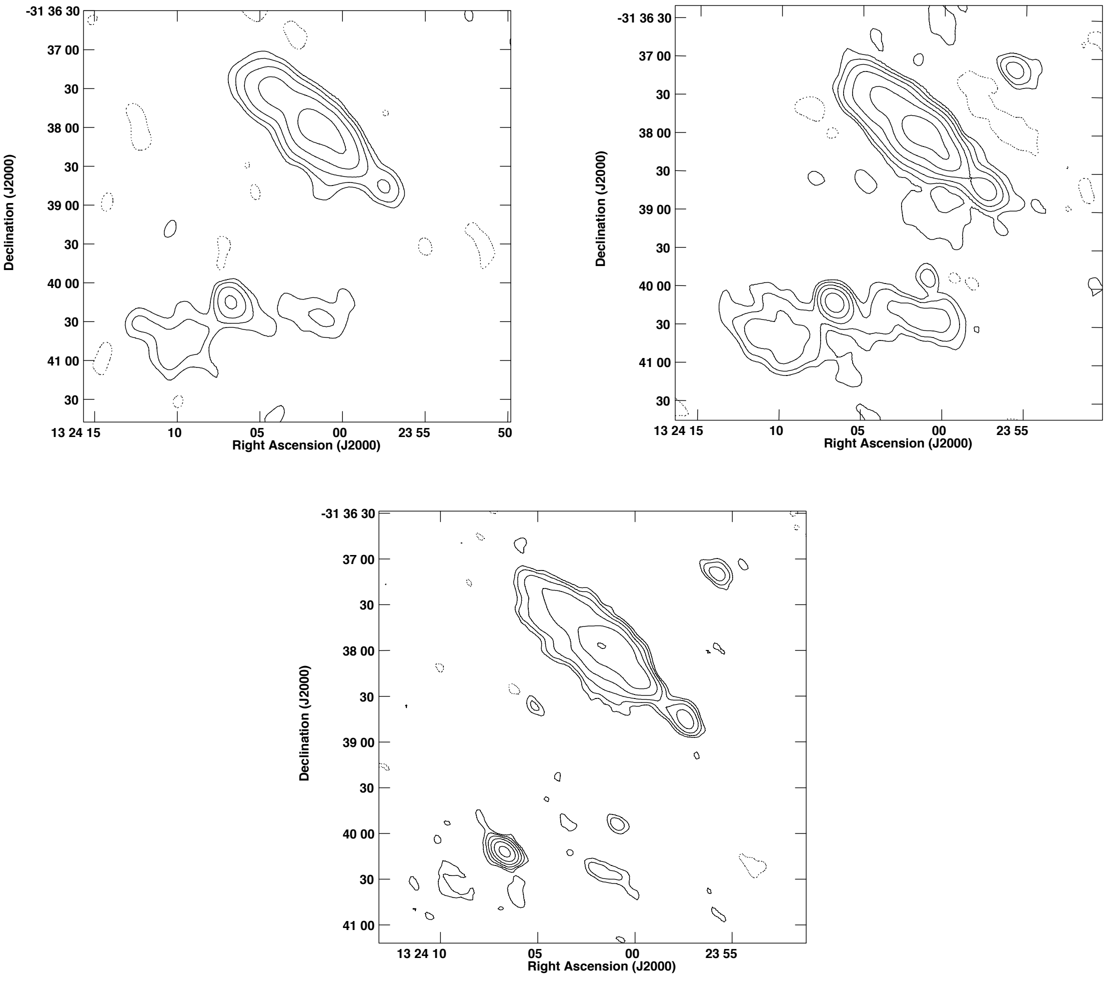

Figure 4.14: J1324-3138 and J1324-3140. *Top panel, left*: radio contours at 235 MHz; the restoring beam is 20.83 × 16.17 arcsec^2, PA = 12.42° and rms ≈ 0.74 mJy/beam. *Top panel, right*: radio contours at 325 MHz; the restoring beam is 16.3 × 11.89 arcsec^2, PA = 12.29° and rms ≈ 0.20 mJy/beam. *Bottom panel*: radio contours at 610 MHz; the restoring beam is 12.86 × 7.2 arcsec^2, PA = 41.78° and rms ≈ 0.08 mJy/beam. The levels are $3\sigma\times(\pm1, 2, 4, 8, 16, 32, 128)$ mJy/beam.

J1324-3138 is located approximatively at 2 arcmin from the A3556 center. Its radio contours at 235, 327 and 610 MHz show that it is a head-tail radio galaxy elongated in the north-east direction. At 610 MHz the nuclear region is better resolved respect to the contours at the other two low frequencies. The peak of emissivity in this source is located in the tail.

High frequency images

The high frequency images are provided by ATCA at .4 and 5 GHz.

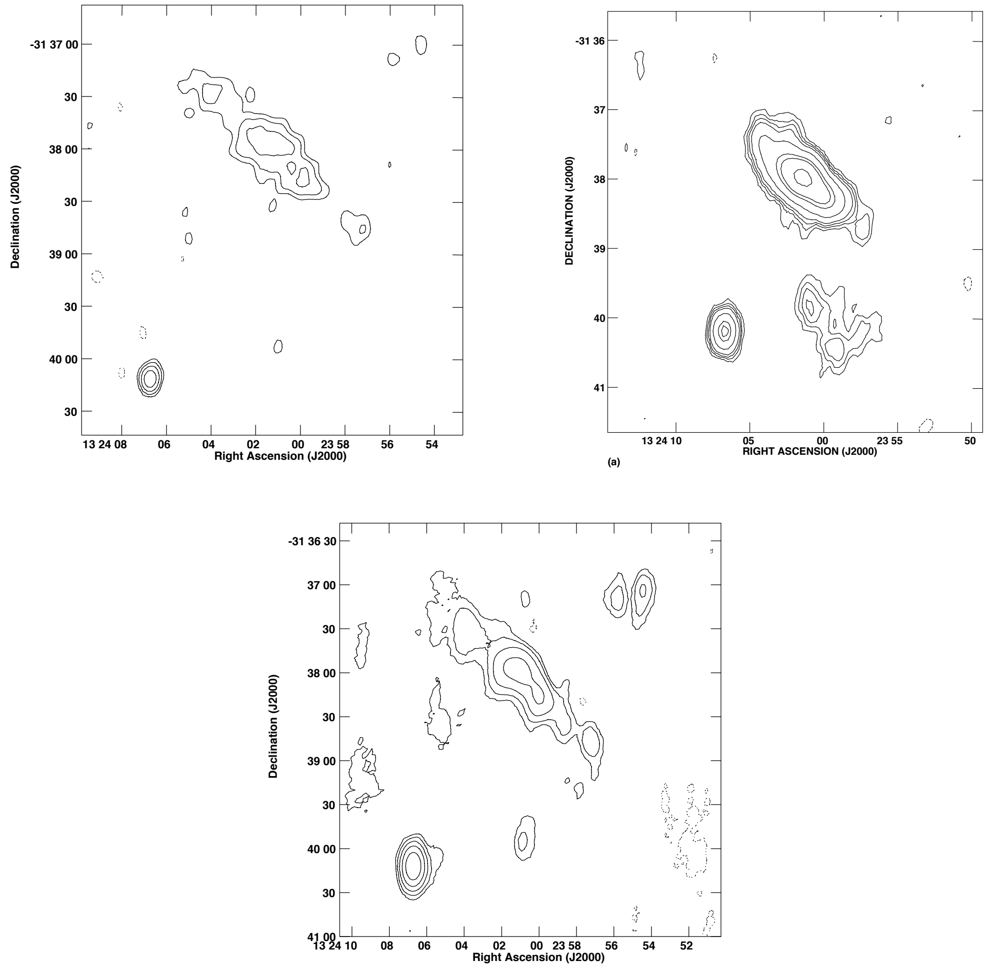

Figure 4.15: J1324-3138 and J1324-3140. *Top panel, left*: radio contours at 1.4 GHz; the restoring beam is 10.18 × 5.95 arcsec^2, PA = 0.26° and rms ≈ 0.19 mJy/beam. *Top panel, right*: natural weighted 1.4 GHz radio contours; the restoring beam is 25.8 × 15.6 arcsec^2, PA = 1.29° and rms ≈ 0.11 mJy/beam (Venturi et al., 1998). *Bottom panel*: radio contours at 5 GHz; the restoring beam is 20 × 10 arcsec^2, PA = 0° and rms ≈ 0.04 mJy/beam. The levels are $3\sigma\times(\pm1, 2, 4, 8, 16, 32, 128)$ mJy/beam.

At high frequencies only the compact component in J1324-3140 associated with the BCG is visible (figure 4.16). ATCA observations at 1.4 GHz presented in Venturi et al. (1998) and reported in figure 4.15 (top right panel), however, reveal some low surface brightness emission west of it, whose origin was unclear at the time of that work. The radio/optical overlay suggests that at least part of the emission has a faint optical counterpart. The rest of the emission could be associated with the western lobe of J1324-3140.

The radio morphology of J1324-3138 is instead quite similar from 235 MHz to 8.4 GHz. This source was studied in Venturi et al. (1998), who concluded that it is most likely a dying radio galaxy, i.e. the nuclear activity is now switched-off.

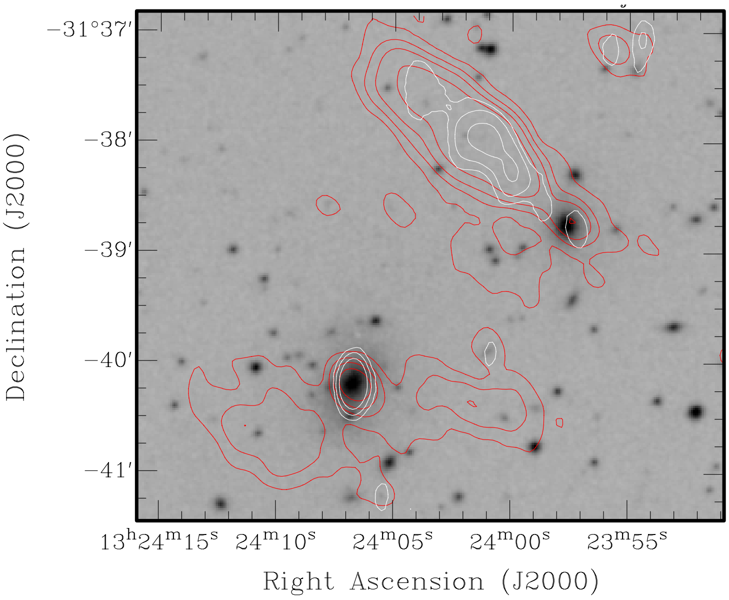

Figure 4.16: Radio-optical overlay of J1324-3138 and J1324-3140 at 325 MHz (red) and 5 GHz (white). The levels are $3\sigma\times(1, 4, 8, 16)$ at 325 MHz and $3\sigma\times(2, 4, 8)$ at 5 GHz.

4.2.2 J1327-3129b

Low frequency images

J1327-3129b is the central dominant galaxy of the A3558 cluster. At low frequencies (figure 4.17) it appears as a compact unresolved source. Literature information is given by Venturi et al. (2000), who observed the A3558 cluster using the ATCA array at 1.38 and 2.38 GHz. The source is compact even at higher frequencies. The radio-optical overlay is shown in figure 4.18.

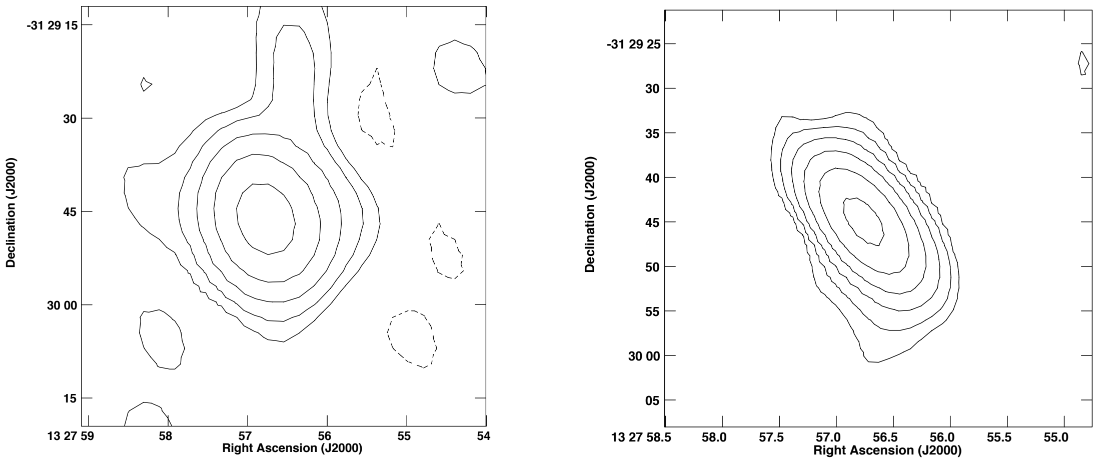

Figure 4.17: J1327-3129b. *Left panel*: radio contours at 325 MHz; the restoring beam is 16.3×11.89 arcsec^2, PA = 12.29° and rms ≈ 0.25 mJy/beam. *Right panel*: radio contours at 610 MHz; the restoring beam is 10.98×5.59 arcsec^2, PA = 35.16° and rms ≈ 0.14 mJy/beam. The levels are $3\sigma\times(\pm1, 2, 4, 8, 16, 32, 128)$ mJy/beam.

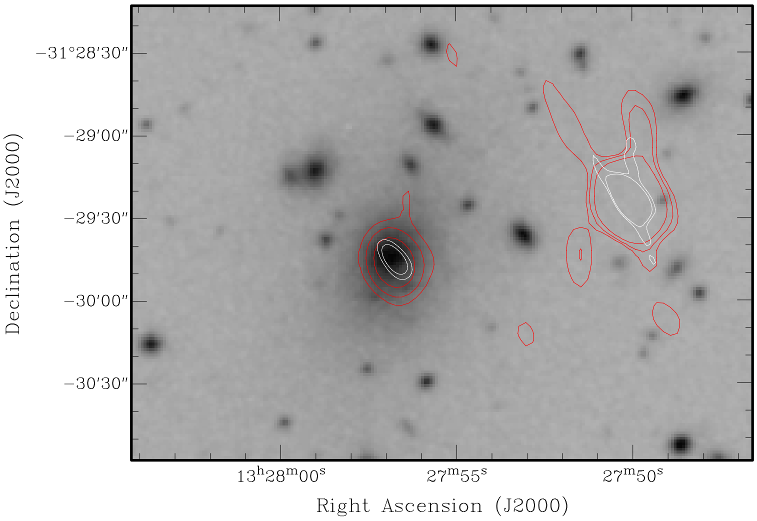

Figure 4.18: Radio-optical overlay of J1327-3129b at 325 MHz (red) and 610 GHz (white). The levels are $3\sigma\times(2, 4, 8)$ at 325 MHz and $3\sigma\times(4, 8)$ at 610 GHz.

4.2.3 J1333-3141

Low frequency images

J1333-3141 is a radio galaxy located at a projected distance of about 1 arcmin from the A3562 center (Venturi et al., 2000). From the radio contours at 235, 325 and 610 MHz (figure 4.19), it is clear that it is a head-tail source. Moreover, observing at low resolution with the GMRT Venturi et al. (2003) and Giacintucci et al. (2005)

found that it is totally embedded in the A3562 radio halo.

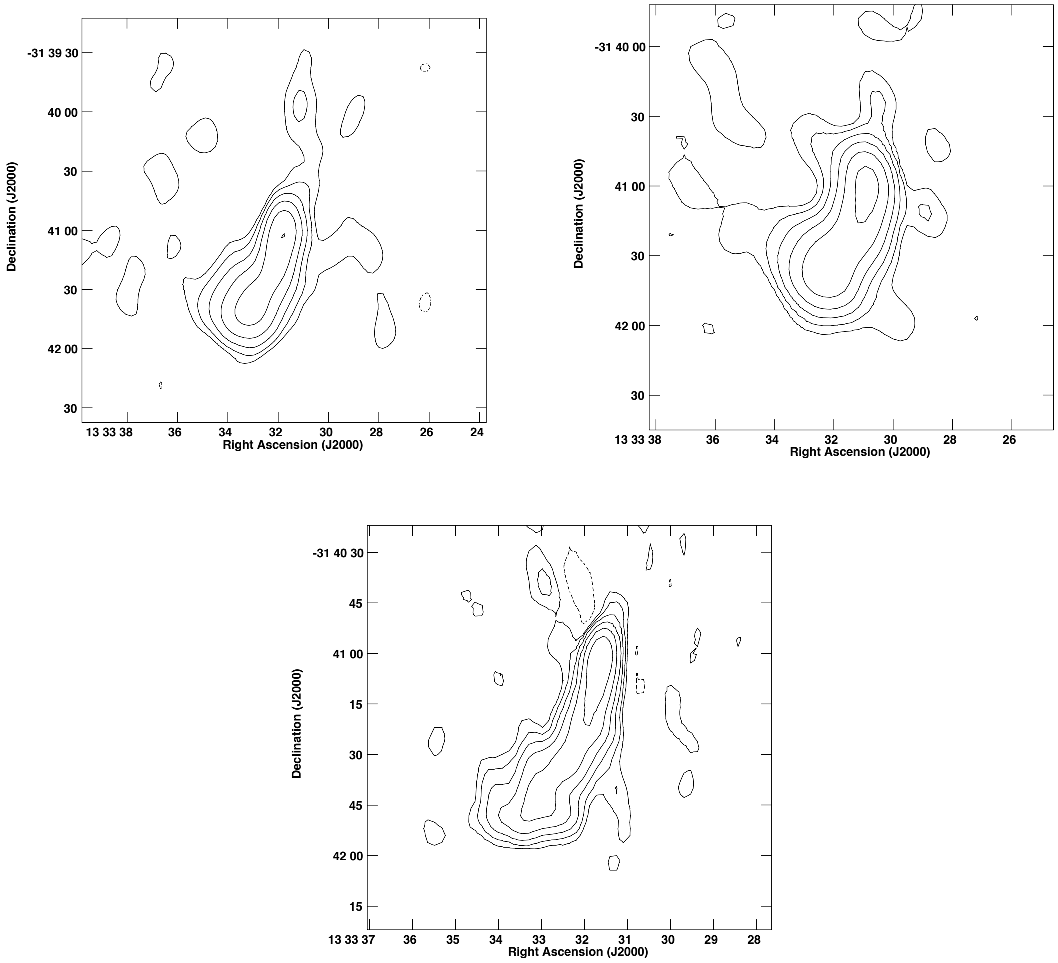

Figure 4.19: J1333-3141. *Top panel, left*: radio contours at 235 MHz; the restoring beam is 18×20 arcsec^2, PA = 5° and rms ≈ 0.88 mJy/beam. *Top panel, right*: radio contours at 325 MHz; the restoring beam is 19.65×12.39 arcsec^2, PA = 28.78° and rms $\approx$ 0.36 mJy/beam. *Bottom panel*: radio contours at 610 MHz; the restoring beam is 8×6 arcsec^2, PA = 0° and rms ≈ 0.08 mJy/beam. The levels are $3\sigma \times (\pm 1$, 2, 4, 8, 16, 32, 128) mJy/beam.

It is interesting to note that the optical central dominant galaxy of the A3562 cluster has no detectable radio emission (figure 4.20), even at the lowest frequency of the our observation (radio-optical superimposition in figure 4.20).

High frequency images

The high frequency images are provided by the ATCA (at 1.4 and 2.4 GHz) and VLA telescope (at 5 and 8.4 GHz). The radio contours are displayed in figure 4.21

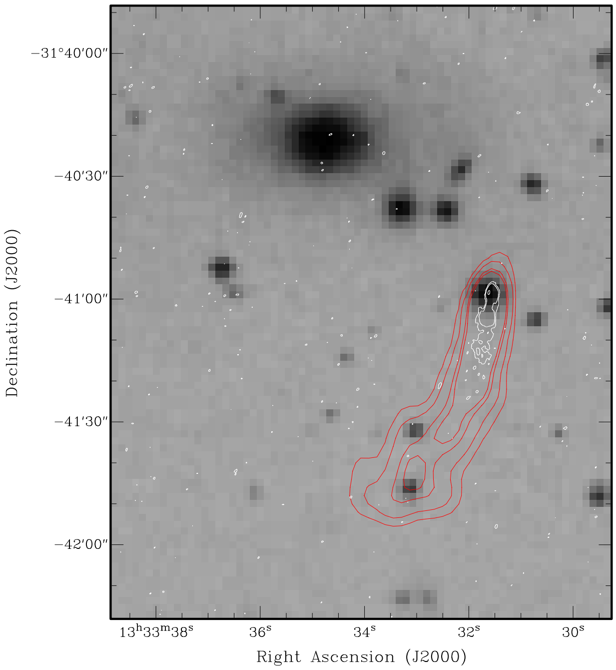

Figure 4.20: Radio-optical overlay of J1333-3141 at 610 MHz (red) and 8.4 GHz (white). The levels are $3\sigma\times(2, 4, 8, 16)$ at 325 MHz and $3\sigma\times(2, 4, 8)$ at 8.4 GHz.

and show that the radio galaxy has a compact radio core, which coincides with the optical galaxy, and a knotty tail, which bends smoothly easterwards expecially at ATCA frequencies. A detailed study of the radio galaxy was performed by Venturi et al. (2003).

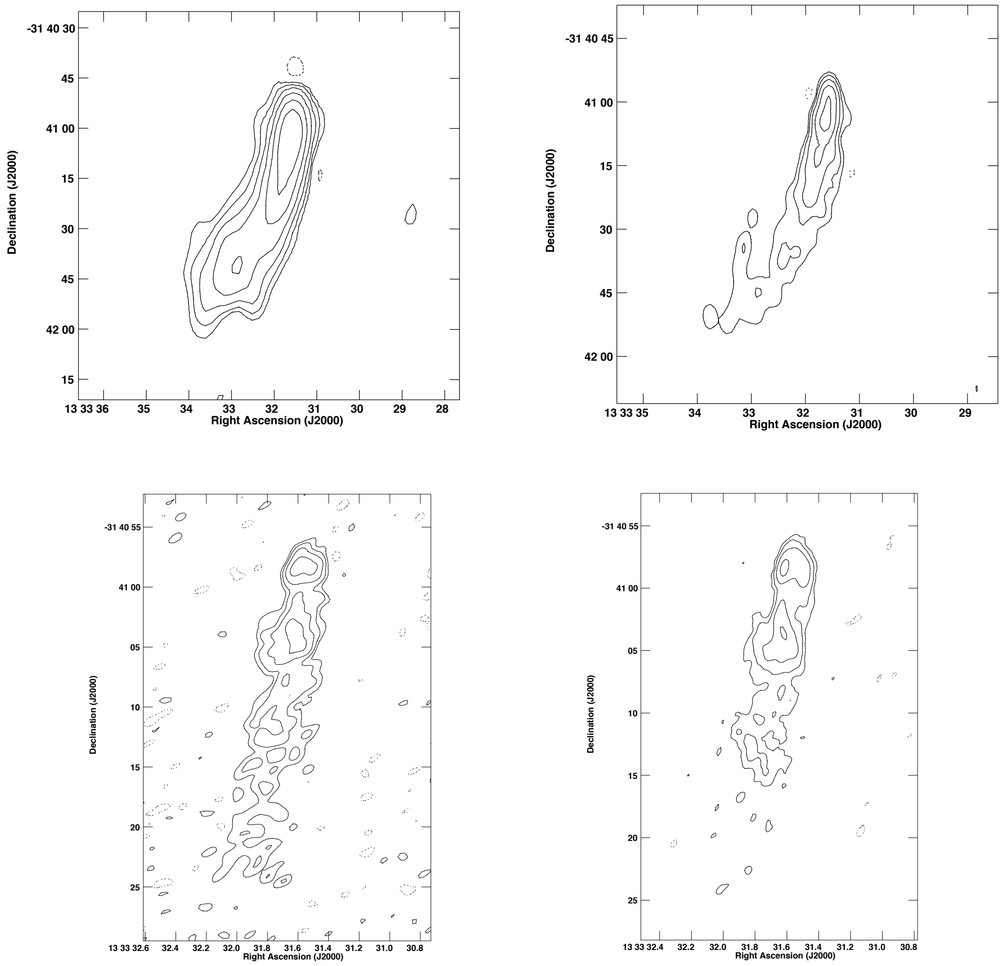

Figure 4.21: J1333-3141. *Top panel, left*: radio contours at 1.4 GHz; the restoring beam is 10.71 × 5.84 arcsec^2, PA = $-0.51°$ and rms ≈ 0.16 mJy/beam. *Top panel, right*: natural weighted 2.4 GHz radio contours; the restoring beam is 5.43 × 3.16 arcsec^2, PA = $0.71°$ and rms ≈ 0.11 mJy/beam (Venturi et al., 1998). *Bottom panel, left*: radio contours at 5 GHz; the restoring beam is 1.46 × 0.84 arcsec^2, PA = $-57.07°$ and rms ≈ 0.04 mJy/beam. *Bottom panel, right*: radio contours at 8.4 GHz; the restoring beam is 1.51 × 0.77 arcsec^2, PA = $-10.57°$ and rms ≈ 0.04 mJy/beam. The levels are $3\sigma\times(\pm1, 2, 4, 8, 16, 32, 128)$ mJy/beam.

Name	cluster	RA (J2000)	DEC (J2000)	$\log P_{1.4\ \mathrm{GHz}}$ W Hz^{-1}	radio morphology	m_{V}	optical morphology
J1254-2900	A3528N	$12^{\mathrm{h}}54^{\mathrm{m}}22.1^{\mathrm{s}}$	$-29^{\mathrm{d}}00^{\mathrm{m}}48^{\mathrm{s}}$	23.84	D	13.5	BCG (cD)
J1254-2901	A3528N	$12^{\mathrm{h}}54^{\mathrm{m}}22.9^{\mathrm{s}}$	$-29^{\mathrm{d}}01^{\mathrm{m}}02^{\mathrm{s}}$	23.52	HT	16.2	ellipt.
J1254-2904	A3528N	$12^{\mathrm{h}}54^{\mathrm{m}}20.4^{\mathrm{s}}$	$-29^{\mathrm{d}}04^{\mathrm{m}}09^{\mathrm{s}}$	23.96	NAT	15.6	ellipt.
J1254-2913	A3528S	$12^{\mathrm{h}}54^{\mathrm{m}}41.0^{\mathrm{s}}$	$-29^{\mathrm{d}}13^{\mathrm{m}}39^{\mathrm{s}}$	24.48	WAT	13.2	BCG (cD)
J1254-2916	A3528S	$12^{\mathrm{h}}54^{\mathrm{m}}52.4^{\mathrm{s}}$	$-29^{\mathrm{d}}16^{\mathrm{m}}18^{\mathrm{s}}$	23.17	HT	14.7	ellipt.
J1257-3021	A3532	$12^{\mathrm{h}}57^{\mathrm{m}}22.5^{\mathrm{s}}$	$-30^{\mathrm{d}}21^{\mathrm{m}}45^{\mathrm{s}}$	24.51	WAT	13.6	dumb-bell
J1324-3138	A3556	$13^{\mathrm{h}}23^{\mathrm{m}}57.5^{\mathrm{s}}$	$-31^{\mathrm{d}}38^{\mathrm{m}}45^{\mathrm{s}}$	23.05	HT	14.3	ellipt.
J1324-3140	A3556	$13^{\mathrm{h}}24^{\mathrm{m}}06.7^{\mathrm{s}}$	$-31^{\mathrm{d}}40^{\mathrm{m}}12^{\mathrm{s}}$	22.45*	D	13.4	BCG (cD)
J1327-3129b	A3558	$13^{\mathrm{h}}27^{\mathrm{m}}56.8^{\mathrm{s}}$	$-31^{\mathrm{d}}29^{\mathrm{m}}43^{\mathrm{s}}$	22.16	unres.	12.6	BCG (cD)
J1333-3140	A3562	$13^{\mathrm{h}}33^{\mathrm{m}}34.8^{\mathrm{s}}$	$-31^{\mathrm{d}}40^{\mathrm{m}}21^{\mathrm{s}}$	undet.	-	13.5	BCG (cD)
J1333-3141	A3562	$13^{\mathrm{h}}33^{\mathrm{m}}31.6^{\mathrm{s}}$	$-31^{\mathrm{d}}41^{\mathrm{m}}01^{\mathrm{s}}$	23.39	HT	15.1†	ellipt.

Table 4.1: Summary of the properties of the sample of the extended radio galaxy in the A3528 and A3558 cluster complexes. References: Venturi et al. (2001) for the objects in the A3528 complex; Venturi et al. (1996 and 2000) for the objects in the A3558 complex; * from NVSS image; † this value is referred to m_{R}. The magnitude values are taken from NED database (http://ned.ipac.caltech.edu).

CHAPTER 5

SPECTRAL ANALYSIS

The synchrotron spectra of radio galaxies are generally well fitted by a power-law, but in some cases a steepening at high frequencies is observed. Such spectral shape is explained as radiative aging effects on relativistic electrons (section 5.1). In this chapter, I will analyse the spectra of the radio galaxies studied here and I will determine the physical parameters that characterized them (section 5.3).

5.1 Radiative losses and spectral steepening

During their active phase, extended radio galaxies have a synchrotron power-law (PL) spectrum with a typical spectral index $\alpha \approx 0.7 \div 0.8$ ($S_\nu \propto \nu^{-\alpha}$). Such radiation is produced by the accretion of material onto the black hole, which is the central engine of the AGN and sustains the growth of the radio galaxy into the external medium. When the accretion stops, the radio activity is no longer sustained, the emitting particles lose their energy and the radio galaxy "rapidly" fades (*dying phase*). Since the higher the particle energy the higher the radiation losses, the spectral steepening starts at high frequencies. In the spectral analysis, only radiative losses are taken into account, since they are expected to be dominant with respect to the adiabatic ones.

The electron spectrum evolution as consequence of the radiative losses, which include only the contribution of the synchrotron radiation, is given by Pacholczyk (1970):

$$N(E,\theta,t) = N_0 E^{-\delta}(1 - c_2 H^2 \sin^2\theta E t)^{\delta-2}\,, \tag{5.1}$$

where E is the energy of the particles, θ is the angle between the velocity and magetic field H vectors, termed pitch angle, and t is the time since the final acceleration occurred either in the nucleus or in the hot spots. The initial population of electrons is assumed to have a power-law spectrum, with a normalization factor N_0 and a spectral index δ. The quantity $c_2 = \frac{2e^4}{3m_{\mathrm{e}}^4c^7}$ is a constant, defined by Pacholczyk (1970), where e and m_{e} are the charge and the mass of electron respectively and c is the speed of light. The resulting synchrotron spectrum is:

$$\varepsilon_\nu(t) = 4\pi c_3 N_0 s B \int_0^{\pi/2} d\theta \sin^2\theta \int_0^{E_T} dE F(x) E^{-\delta} \times \begin{cases} (1 - c_2 H^2 \sin^2\theta E t)^{\delta-2} & \text{(KP)} \\ (1 - c_2 H^2 \langle \sin^2\theta \rangle E t)^{\delta-2} & \text{(JP)} \end{cases} \tag{5.2}$$

where $E_T \equiv (c_2 H^2 \sin^2\theta E t)^{-1}$, s is the source depth and $c_3 = \frac{\sqrt{3}e^3}{4\pi m_{\mathrm{e}} c^2}$ is another constant defined by Pacholczyk (1970), as are the function $F(x)$ and the characteristic frequency ν_{c}, where $x \equiv \frac{\nu}{\nu_{\mathrm{c}}}$.

The equation system indicates two different models of radiation losses, which aim to describe the shape of the spectral curvature. The Kardashev-Pacholczyk (KP) model assumes that the electrons do not change their pitch angle during their radiative lifetime, and the electron density and magnetic field are homogeneous along the source depth (Kardashev 1962, and Pacholczyk 1970). The Jaffe & Perola (JP) model, instead, assume that the pitch angle is continuously isotropized by electron scattering, whose time scale is much shorter than their radiative lifetime (Jaffe & Perola, 1974). For this reason, the term $\langle \sin^2\theta \rangle$ in equation 5.2 represents the time averaging, which is equal to $2/3$ for an isotropic pitch-angle distribution. Hence, the JP spectrum results slightly steeper than the KP one (top panel in figure 5.1).

According to these two models, the steepening results at energies above a given frequency ν_{br}, termed break frequency:

$$\nu_{\mathrm{br}} = \begin{cases} 1.12 \times 10^9 \left(\frac{H}{\mathrm{mG}}\right)^{-3} \left(\frac{t}{\mathrm{yr}}\right)^{-2} & \text{(KP)} \\ 2.52 \times 10^9 \left(\frac{H}{\mathrm{mG}}\right)^{-3} \left(\frac{t}{\mathrm{yr}}\right)^{-2} & \text{(JP)} \end{cases} \quad \mathrm{GHz} \tag{5.3}$$

which progressively shifts to at lower values with the time. Both models assume an initial single injection of electrons.

A third model assumes that the particles are continuously injected with a power-law energy spectrum $N(E) \propto E^{-\delta_{\mathrm{inj}}}$ in a region of constant magnetic field (IC model, by Kardashev 1962). Such energy spectrum results in a power-law with spectral index $\alpha_{\mathrm{inj}} = \frac{\delta_{\mathrm{inj}}-1}{2}$ below the break frequency and $\leq \alpha_{\mathrm{inj}} + 0.5$ above it (bottom panel in figure 5.1).

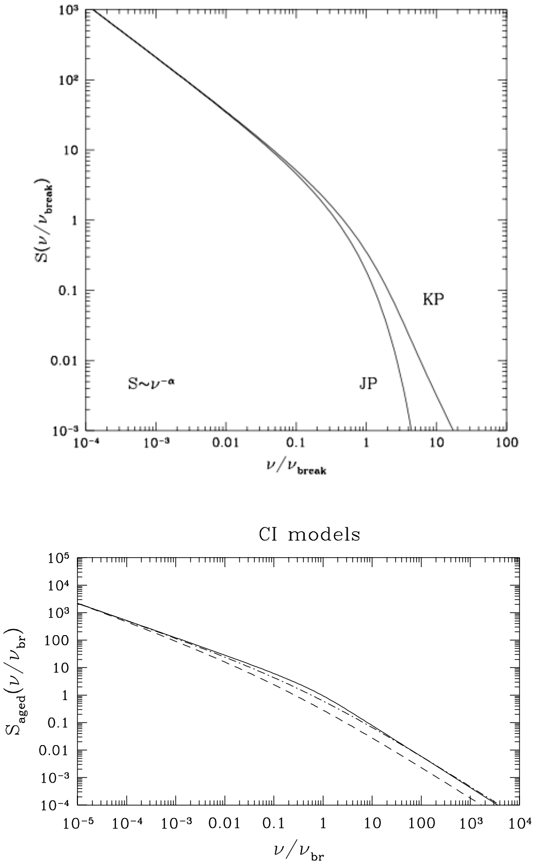

Figure 5.1: *Top panel*: Kardashev-Pacholczyk and Jaffe-Perola loss models (Murgia et al. 2000). *Bottom panel*: three kinds of continuous injection model; the standard CI is plotted with the solid line, while the one that take account of expansion effects (CIE) and the variation of the magnetic field (CIm) are plotted with dashed and dot-dashed lines, respectively (Murgia et al. 1999). Both plots are in arbitrary units.

Taking into account Inverse Compton[1] losses too, due to the scattering between the relativistic electrons and the CMB photons, the age of the radio sources for the three models are (Feretti et al. 1998):

$$t_{\rm br} = \begin{cases} 1060\,\frac{H^{0.5}}{H^2+\frac{2}{3}H^2_{\rm CMB}}[(1+z)\nu_{\rm br}]^{-0.5} & \text{(KP)} \\ 1590\,\frac{H^{0.5}}{H^2+H^2_{\rm CMB}}[(1+z)\nu_{\rm br}]^{-0.5} & \text{(JP)} \\ 1610\,\frac{H^{0.5}}{H^2+H^2_{\rm CMB}}[(1+z)\nu_{\rm br}]^{-0.5} & \text{(IC)} \end{cases} \quad \text{Myr} \tag{5.4}$$

where H and $H_{\rm CMB}$ are expressed in μG and $\nu_{\rm br}$ in GHz. The parameter $H_{\rm CMB}$ is a

---

[1] The Inverse Compton (IC) is the radiation due to the interplay between relativistic electrons and low-energy photons.

fake magnetic field whose strength has an energy density equal to that of the CMB at the redshift z: $H_{\mathrm{CMB}} = 3.25(1+z)^2$ μG.

Once the power supply from the nucleus is switched-off, the radio spectrum undergoes a further steepening and drops exponentially. During this new phase, called *relic phase* (Komissarov & Gubanov 1994), the spectrum is modeled using the $\mathrm{CI_{OFF}}$ model (e.g. Parma et al. 2007, and Murgia et al. 2011). It is based on a continuous injection of particles for part of the lifetime of the radio source followed by the interruption of the nuclear activity. It also assumes that the magnetic field is constant whitin the source.

Another intriguing phase starts when the central nucleus switches on again and produce new radio activity. During the *re-started activity phase*, the radio galaxy may present a nuclear region with a spectral index typical of an active radio galaxy, and a surronding diffuse emission characterized by a very steep value of α.

5.2 Flux densities and radio spectra

In order to study the spectral behaviour of the extended radio galaxies it is necessary to measure the flux density over the widest range of frequencies possible. For this reason, the observations made with the GMRT at low frequencies (235 and 610 MHz) have been complemented with the high frequency measurements available in the literature and provided by ATCA (1.38 and 2.38 GHz), MOST (843 MHz) and VLA (5 and 8.4 GHz). Moreover, the images at 150 MHz obtained with the TIFR GMRT Sky Survey (TGSS) and at 1.4 GHz with the NRAO VLA Sky Survey (NVSS) have been used.

5.2.1 Flux density measurements

The comparison between the low and high frequency images, which have been shown in chapter 4, shows that most of the radio galaxies of the sample show a nuclear component and further emission on the large scale. In all cases and at each frequency, we derived the total flux density and the contribution of the nuclear and the extended component separately.

At each frequency, the flux density measurement was performed using the task TVSTAT in the AIPS package, which traces a polygonal curve that allows the selection of a specific region of the image. The total flux densities at low frequencies were measured by considering the total emitting volume of the sources from the radio contours at 235 MHz. In this way, I also took into account the possible sensitivity limits in the images, where the total size of the radio emission is usually lower. The size of the inner region was selected according to the image at highest frequency to isolate the nuclear emission, while the flux density of the diffuse emission was obtained by subtraction of the central flux density from the total one. The only exceptions are J1257-3021 and J1324-3140, where the central and the diffuse flux densities were obtained individually, as they are well separated.

In two radio galaxies of the sample the core is unresolved. In these cases, the flux density measurement was taken with the task JMFIT. It performs a 2D Gaussian fit of the selected compact region and, after a number of iterations, it returns the peak and the integrated flux densities, the de-convolved size, the position angle, and the position of the peak. This task allows a better estimate of the flux density of the radio galaxy core.

The flux densities of the radio galaxies of the sample are listed in tables from 5.2 to 5.11.

Errors

The flux density error $\sigma_{\rm s}$ is the sum of two contributions. The first is the thermal noise of the image, which is parametrized as:

$$\sigma_{\rm rms} = {\rm rms} \times \sqrt{\frac{A_{\rm source}}{A_{\rm beam}}}\,. \tag{5.5}$$

where $A_{\rm source}$ and $A_{\rm beam}$ are the source and the beam areas respectively. The rms is the noise of the image that has been measured as near as possible to the radio galaxy, and it is of the order of $10^{-3} \div 10^{-4}$ Jy/beam (see tables 3.4 and 3.5). A second term, $\sigma_{\rm cal}$, is given by the residual amplitude errors due to the calibration procedure (table 5.1). Hence, it depends on the data reduction of the single observation and it is generally of the order of a small percentage of the flux density of the source.

Therefore, the total flux density error is:

$$\sigma_{\rm s} = \sqrt{\sigma^2_{\rm rms} + \sigma^2_{\rm cal}}\,. \tag{5.6}$$

In general for sources with flux density as high as those discussed in this thesis work, the calibration error is the dominant contribution: $\sigma_{\rm s} \approx \sigma_{\rm cal}$. The $\sigma_{\rm cal}$ values in table 5.1 agree with the residual amplitude errors found by Chandra et al. (2004).

The diffuse flux density errors, determined as the difference between the total and the central ones, is obtained by means of the formula of propagation of errors.

Telescope	ν (MHz)	$\sigma_{\rm cal}$ (%)	Ref.
GMRT	150	20	$^{(b)}$
GMRT	235	8	$^{*,(a)}$
GMRT	325	5	$^{(a)}$
VLA	327	5	$^{(e)}$
GMRT	610	5	$^{*,(a)}$
MOST	843	5	$^{(c)}$
ATCA	1380	1	$^{(e),(f)}$
VLA	1400	3	$^{(d)}$
ATCA	2380	1	$^{(e),(f)}$
VLA	5000	3	$^{(e)}$
ATCA	5000	3	$^{(e)}$
VLA	8400	3	$^{(e)}$

Table 5.1: Calibration errors for each telescope at each frequency. References: * this thesis; $^{(a)}$ Venturi et al., in preparation; $^{(b)}$ http://tgss.ncra.tifr.res.in; $^{(c)}$ Bock et al. (1999); $^{(d)}$ Condon et al. (1998); $^{(e)}$ Venturi et al. (1997, 1998, 2000 and 2001); $^{(f)}$ Reid et al. (1998).

5.2.2 Integrated radio spectra

The integrated radio spectra of the radio galaxies discussed here are displayed from figure 5.2 to 5.11. For the radio galaxies whose emission is characterized by a nuclear and an extended component, the spectra of the central and extended region are plotted too. Such spectra were then fitted with the SYNAGE++ software (Murgia 1999, 2001) in order to obtain the radiative loss model which better describes the data. This program assumes an initial spectral index that agrees with the pure-synchrotron spectrum (power-law) and then considers a second slope with the purpose of fitting the high frequency region of the spectrum. After a series of iterations which minimize the χ^2 of the global fit, the program provides in output the $\nu_{\rm br}$ value. The resulting fit models are shown in figures 5.12 through 5.21. For each radio galaxy not all the data plotted in figure and listed in table are used to produce the best fit model. In particular, the MOST flux density value at 843 MHz is generally neglected, since it is systematically above to the slope of the spectra and possibly suffers from confusion. Moreover, due to the different restoring beam the flux densities at a given frequency are not always comparable, hence we selected the data at similar resolution. Finally, the flux densities at 610 MHz are sometimes lower than the spectral slope, but this is a known problem for the GMRT observations.

Telescope	ν (MHz)	S_c (mJy)	Restoring beam (arcsec^2)	Ref.
GMRT	235	996.1 ± 79.7	16.3×11.9	(a)
GMRT	610	428.1 ± 21.4	6.8×4.7	(a)
ATCA	1380	230.9 ± 6.9	10.0×6.0	(c)
ATCA	1400	211.0 ± 6.3	11.8×6.2	(b)
ATCA	2380	142.4 ± 4.3	6.0×3.5	(c)
ATCA	2400	143.0 ± 4.3	6.2×4.2	(b)
VLA	8400	50.5 ± 1.5	2.76×1.59	(d)

Table 5.2: J1254-2900. References: (a) this thesis; (b) Reid et al. (1998); (c) Venturi et al. (2001); (d) VLA image (Venturi et al. 2000).

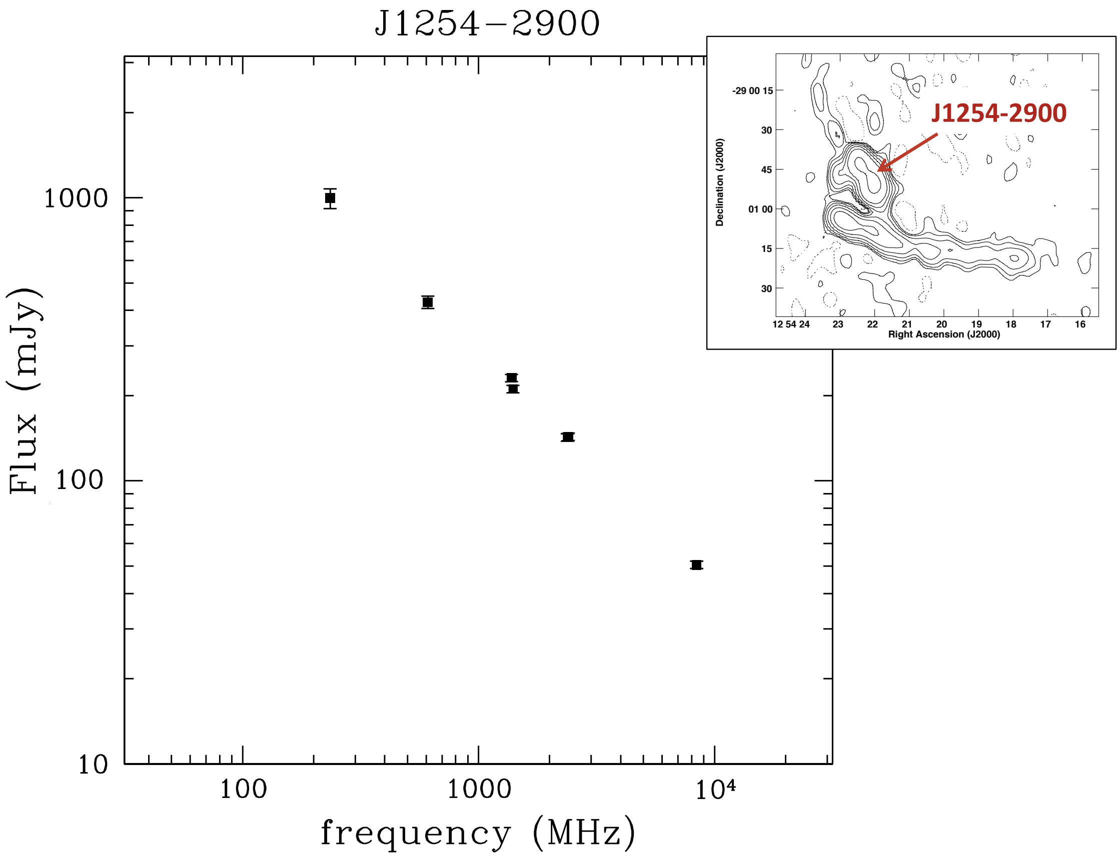

Figure 5.2: Integrated radio spectrum of J1254-2900.

Telescope	ν (MHz)	$S_{\rm tot}$ (mJy)	$S_{\rm c}$ (mJy)	$S_{\rm diff}$ (mJy)	Restoring beam (arcsec^2)	Ref.
GMRT	235	349.4 ± 28.0	239.9 ± 19.2	109.5 ± 34.0	16.3×11.9	$^{(a)}$
GMRT	610	186.6 ± 9.3	140.0 ± 7.0	46.6 ± 11.6	6.8×4.7	$^{(a)}$
ATCA	1380	-	110.5 ± 3.3	-	10.0×6.0	$^{(c)}$
ATCA	1400	-	97.0 ± 3.0	-	11.8×6.2	$^{(b)}$
ATCA	2380	-	57.9 ± 1.7	-	6.0×3.5	$^{(c)}$
ATCA	2400	-	65.0 ± 2.0	-	6.2×4.2	$^{(b)}$
VLA	8400	-	22.1 ± 0.7	-	2.76×1.59	$^{(d)}$

Table 5.3: J1254-2901. References: $^{(a)}$ this thesis; $^{(b)}$ Reid et al. (1998); $^{(c)}$ Venturi et al. (2001); $^{(d)}$ VLA image (Venturi et al. 2000).

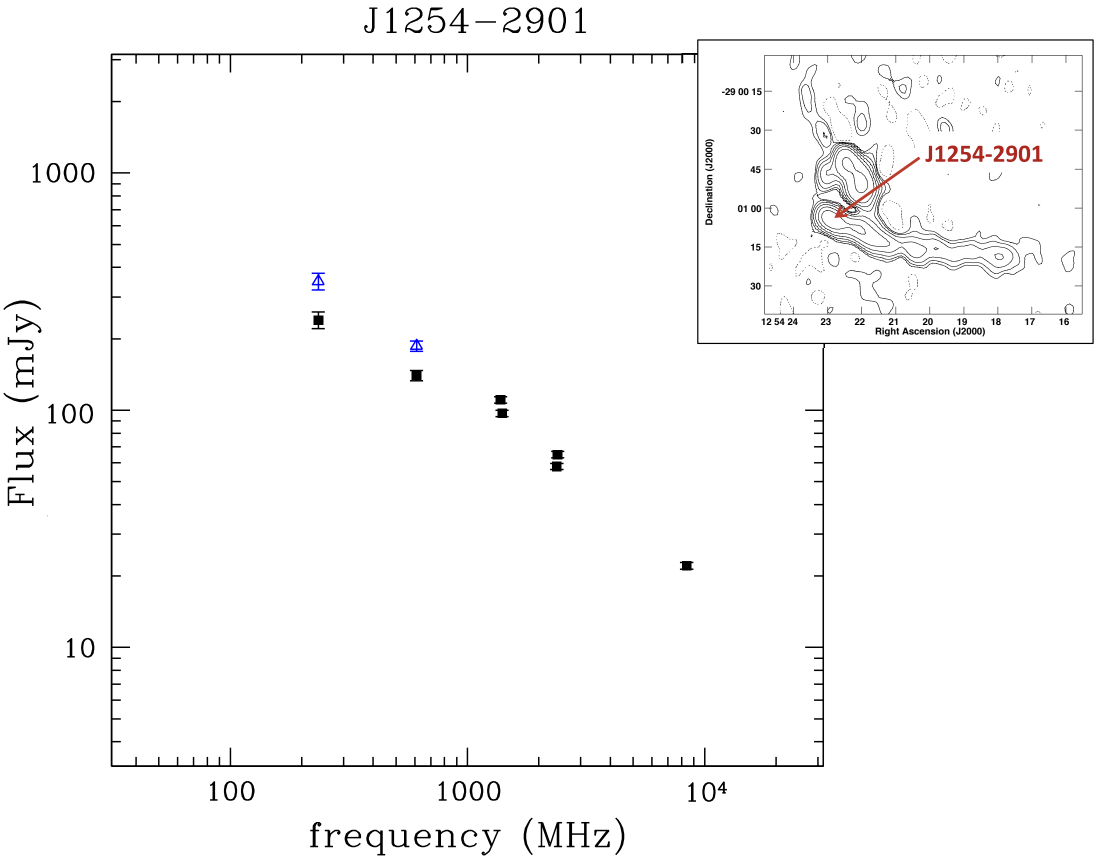

Figure 5.3: Integrated radio spectrum of J1254-2901. The filled squares represent the flux densities of the central region, while the open blue triangles represent the total flux densities.

Telescope	ν (MHz)	$S_{\rm tot}$ (mJy)	$S_{\rm c}$ (mJy)	$S_{\rm diff}$ (mJy)	Restoring beam (arcsec^2)	Ref.
GMRT	150	1561.4 ± 312.3	525.6 ± 105.1	1035.2 ± 329.2	24.0×15.0	$^{(e)}$
GMRT	235	782.8 ± 62.6	377.5 ± 30.2	405.3 ± 69.5	16.3×11.9	$^{(a)}$
GMRT	610	365.0 ± 18.3	177.9 ± 8.9	209.0 ± 21.3	6.8×4.7	$^{(a)}$
MOST	843	519.0 ± 15.6	-	-	88.7×43.0	$^{(g)}$
ATCA	1380	259.9 ± 7.8	-	-	10.0×6.0	$^{(c)}$
ATCA	1400	240.0 ± 7.2	-	-	11.8×6.2	$^{(b)}$
VLA	1400	311.7 ± 9.4	-	-	45.0×45.0	$^{(f)}$
ATCA	2380	142.8 ± 4.3	-	-	6.0×3.5	$^{(c)}$
VLA	8400	-	45.9 ± 1.4	-	2.76×1.59	$^{(d)}$

Table 5.4: J1254-2904. References: $^{(a)}$ this thesis; $^{(b)}$ Reid et al. (1998); $^{(c)}$ Venturi et al. (2001); $^{(d)}$ VLA image (Venturi et al. 2000); $^{(e)}$ TGSS image (http://tgss.ncra.tifr.res.in); $^{(f)}$ NVSS image (http://www.cv.nrao.edu/nvss/); $^{(g)}$ SUMSS catalog (http://www.physics.usyd.edu.au/sifa/Main/SUMSS).

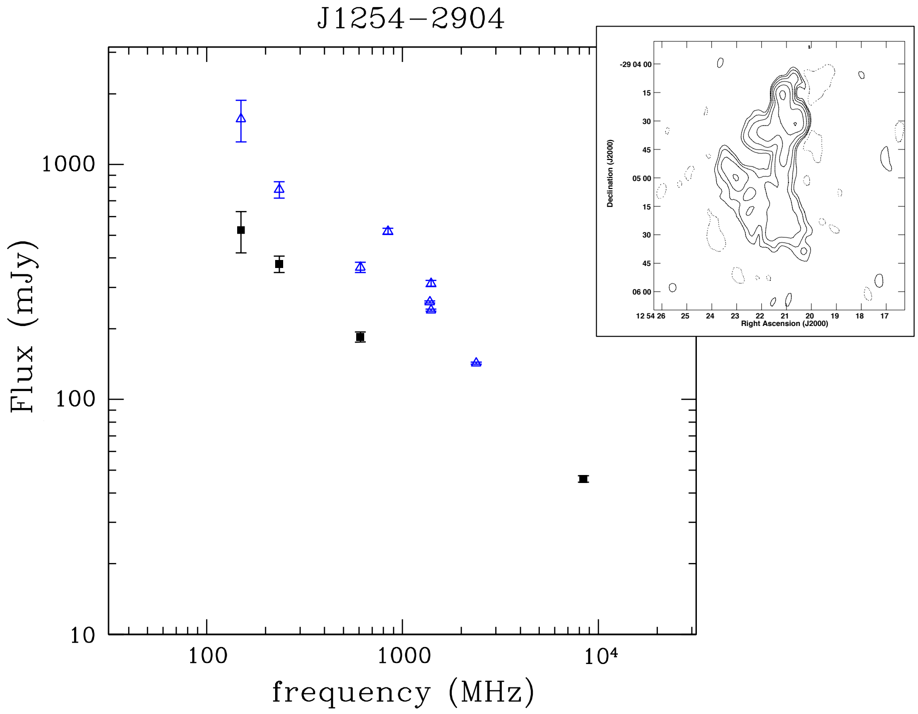

Figure 5.4: Integrated radio spectrum of J1254-2904. The filled squares represent the flux densities of the central region, while the open blue triangles represent the total flux densities. The MOST at 843 MHz and the NVSS at 1.4 GHz flux densitis are higher than the ones expected from the global slope of the data.

Telescope	ν (MHz)	$S_{\rm tot}$ (mJy)	$S_{\rm c}$ (mJy)	$S_{\rm diff}$ (mJy)	Restoring beam (arcsec^2)	Ref.
GMRT	150	14491.0 ± 2898.2	-	-	24.0×15.0	$^{(e)}$
GMRT	235	7291.4 ± 583.3	4714.5 ± 377.2	2576.9 ± 694.6	16.3×11.9	$^{(a)}$
GMRT	610	2159.1 ± 108.0	1956.7 ± 97.8	202.4 ± 145.8	6.8×4.7	$^{(a)}$
MOST	843	1970.0 ± 59.1	-	-	88.7×43.0	$^{(g)}$
ATCA	1380	-	936.7 ± 28.1	-	10.0×6.0	$^{(c)}$
ATCA	1400	-	848.0 ± 25.4	-	11.8×6.2	$^{(b)}$
VLA	1400	-	1069.1 ± 32.1	-	45.0×45.0	$^{(f)}$
ATCA	2380	-	538.4 ± 16.2	-	6.0×3.5	$^{(c)}$
ATCA	2400	-	477.0 ± 14.3	-	6.2×4.2	$^{(b)}$
VLA	8400	-	30.4 ± 0.9	-	2.76×1.59	$^{(d)}$

Table 5.5: J1254-2913. References: $^{(a)}$ this thesis; $^{(b)}$ Reid et al. (1998); $^{(c)}$ Venturi et al. (2001); $^{(d)}$ VLA image (Venturi et al. 2000); $^{(e)}$ TGSS image (http://tgss.ncra.tifr.res.in); $^{(f)}$ NVSS image (http://www.cv.nrao.edu/nvss/); $^{(g)}$ SUMSS catalog (http://www.physics.usyd.edu.au/sifa/Main/SUMSS).

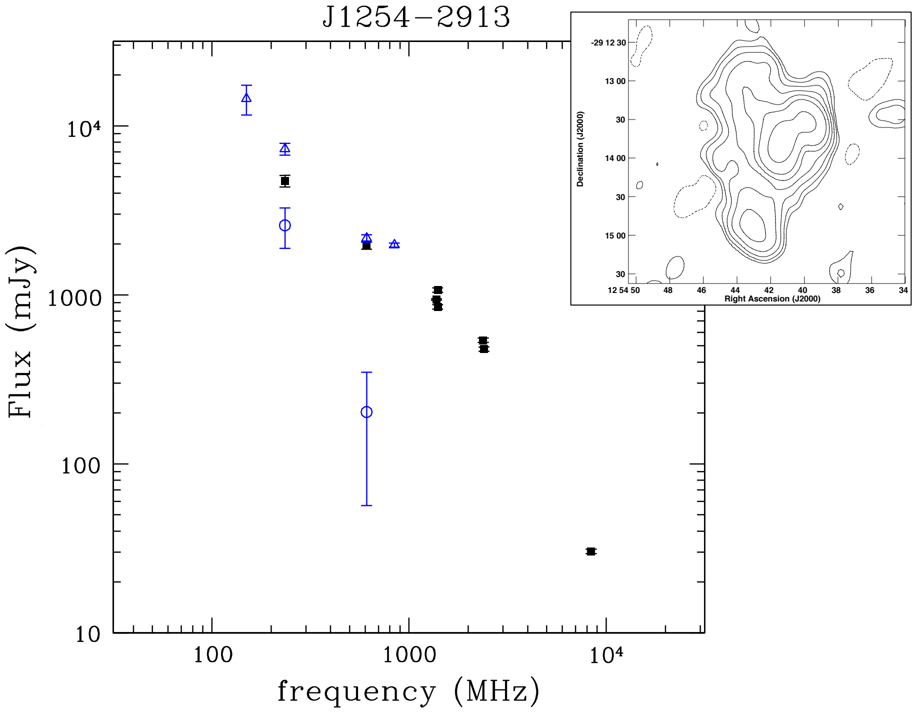

Figure 5.5: Integrated radio spectrum of J1254-2913. The filled squares, the open blue triangles and the open blue circles represent the flux densities of the central, total and diffuse region respectively. The MOST flux density is higher than the one expected from the global slope of the data. Moreover, the central region is not clearly observed in the TGSS image, hence its flux density was not obtained.

Telescope	ν (MHz)	$S_{\rm c}$ (mJy)	Restoring beam (arcsec^2)	Ref.
GMRT	235	186.5 ± 14.9	16.3×11.9	(a)
GMRT	610	87.4 ± 4.8	6.8×4.7	(a)
MOST	843	124.0 ± 3.7	88.7×43.0	(b)
ATCA	1380	62.1 ± 1.9	10.0×6.0	(c)
VLA	1400	85.8 ± 2.6	45.0×45.0	(e)
ATCA	2380	49.6 ± 1.5	6.2×4.2	(c)
VLA	8400	15.3 ± 0.5	2.76×1.59	(d)

Table 5.6: J1254-2916. References: (a) this thesis; (b) Reid et al. (1998); (c) Venturi et al. (2001); (d) VLA image (Venturi et al. 2000); (e) NVSS image (http://www.cv.nrao.edu/nvss/).

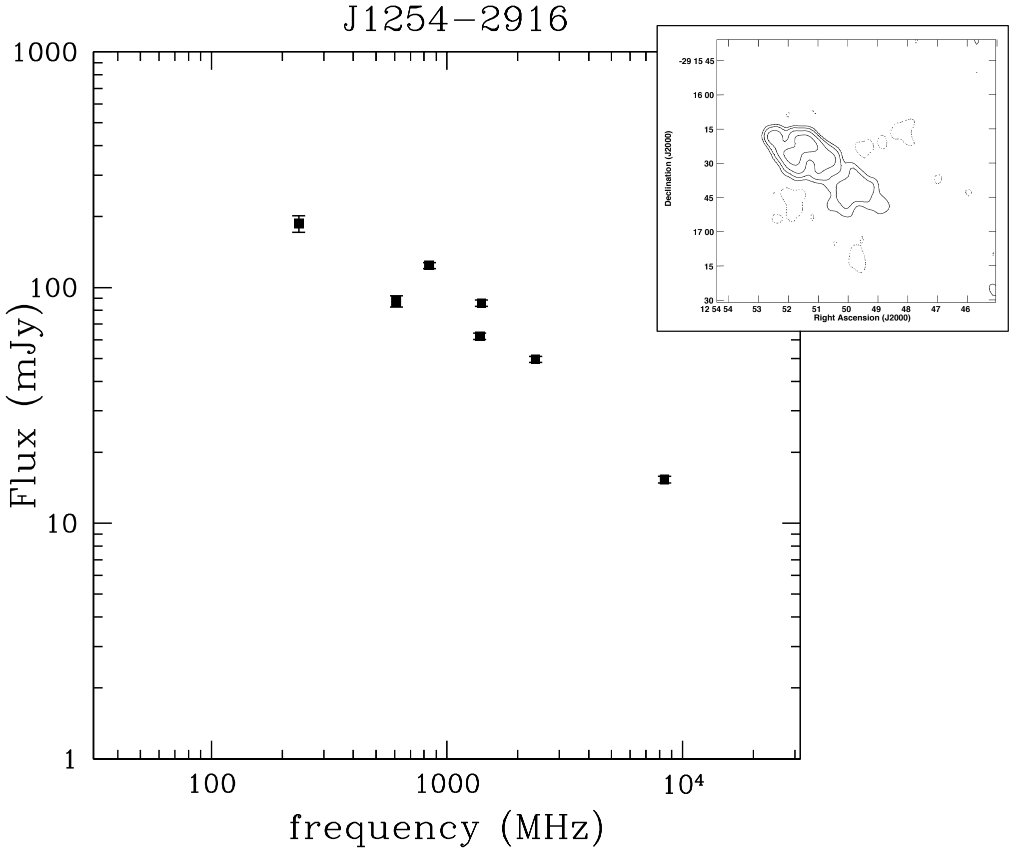

Figure 5.6: Integrated radio spectrum of J1254-2916. The MOST and the NVSS flux densities are higher than the ones expected from the global slope of the data.

Telescope	ν (MHz)	$S_{\rm c}$ (mJy)	$S_{\rm diff}$ (mJy)	Restoring beam (arcsec^2)	Ref.
GMRT	150	6802.4 ± 1360.5	1853.5 ± 370.7	24.0×15.0	$^{(e)}$
GMRT	235	4251.3 ± 334.9	340.5 ± 27.2	16.3×11.9	$^{(a)}$
GMRT	610	1484.0 ± 74.2	38.0 ± 1.9	6.8×4.7	$^{(a)}$
MOST	840	1773.0 ± 53.2	-	88.7×43.0	$^{(f)}$
ATCA	1380	1056.5 ± 31.7	-	10.0×6.0	$^{(b)}$
ATCA	1400	1038.3 ± 31.1	-	11.8×6.2	$^{(c)}$
VLA	1400	1061 ± 31.8	-	45.0×45.0	$^{(d)}$
ATCA	2380	651.7 ± 19.6	-	6.2×4.2	$^{(b)}$

Table 5.7: J1257-3021. References: $^{(a)}$ this thesis; $^{(b)}$ Venturi et al. (2001); $^{(c)}$ ATCA images (Venturi et al. 1998); $^{(d)}$ NVSS image (http://www.cv.nrao.edu/nvss/); $^{(e)}$ TGSS image (http://tgss.ncra.tifr.res.in); $^{(f)}$ SUMSS catalog (http://www.physics.usyd.edu.au/sifa/Main/SUMSS).

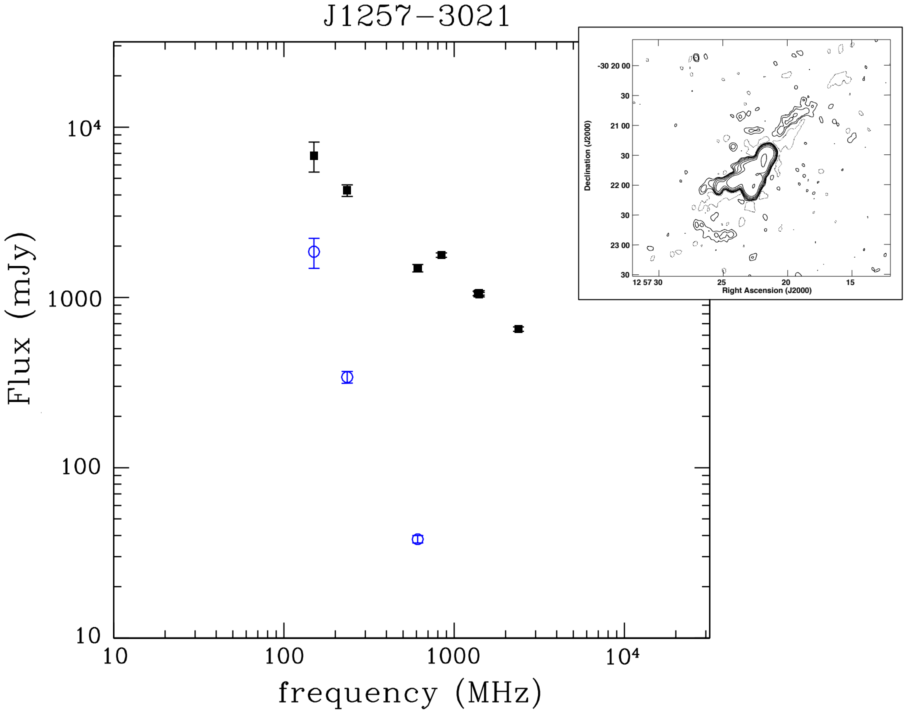

Figure 5.7: Integrated radio spectrum of J1257-3021. The filled squares represent the flux densities of the central region, while the open blue circles represent the flux densities of the diffuse emission located in north-east direction. The MOST flux density is higher than the one expected from the global slope of the data.

Telescope	ν (MHz)	$S_{\rm tot}$ (mJy)	$S_{\rm c}$ (mJy)	$S_{\rm diff}$ (mJy)	Restoring beam (arcsec^2)	Ref.
GMRT	235	278.3 ± 22.3	9.1 ± 0.7	269.2 ± 22.3	20.83×16.17	$^{(a)}$
VLA	327	230.0 ± 11.5	-	-	59.4×45.2	$^{(b)}$
GMRT	325	254.0 ± 12.7	8.1 ± 0.4	245.9 ± 12.7	16.3×11.9	$^{(a)}$
GMRT	610	122.7 ± 6.1	6.2 ± 0.2	119.5 ± 6.1	12.86×7.2	$^{(a)}$
MOST	843	80.2 ± 2.4	-	-	82.0×43.0	$^{(b)}$
ATCA	1376	41.0 ± 1.2	2.1 ± 0.1	38.9 ± 1.2	10.2×5.9	$^{(b)}$
ATCA	1380	41.2 ± 1.2	-	-	6.0×10.1	$^{(c)}$
ATCA	1400	43.1 ± 1.3	2.7 ± 0.1	40.4 ± 1.3	10.18×5.95	$^{(d)}$
ATCA	2380	21.0 ± 0.6	-	-	3.4×5.3	$^{(c)}$
ATCA	2382	21.0 ± 0.6	1.7 ± 0.1	19.3 ± 0.6	9.8×6.5	$^{(b)}$
ATCA	4790	7.3 ± 0.3	0.50 ± 0.03	6.8 ± 0.3	20.0×10.0	$^{(b)}$
ATCA	5000	6.8 ± 0.2	0.30 ± 0.01	6.5 ± 0.2	20.0×10.0	$^{(d)}$
ATCA	8640	2.2 ± 0.1	0.10 ± 0.01	2.1 ± 0.1	20.0×10.0	$^{(d)}$

Table 5.8: J1324-3138. References: $^{(a)}$ Venturi et al. (in preparation); $^{(b)}$ Venturi et al. (1998); $^{(c)}$ Venturi et al. (1997); $^{(d)}$ATCA image (Venturi et al. 1997, 1998).

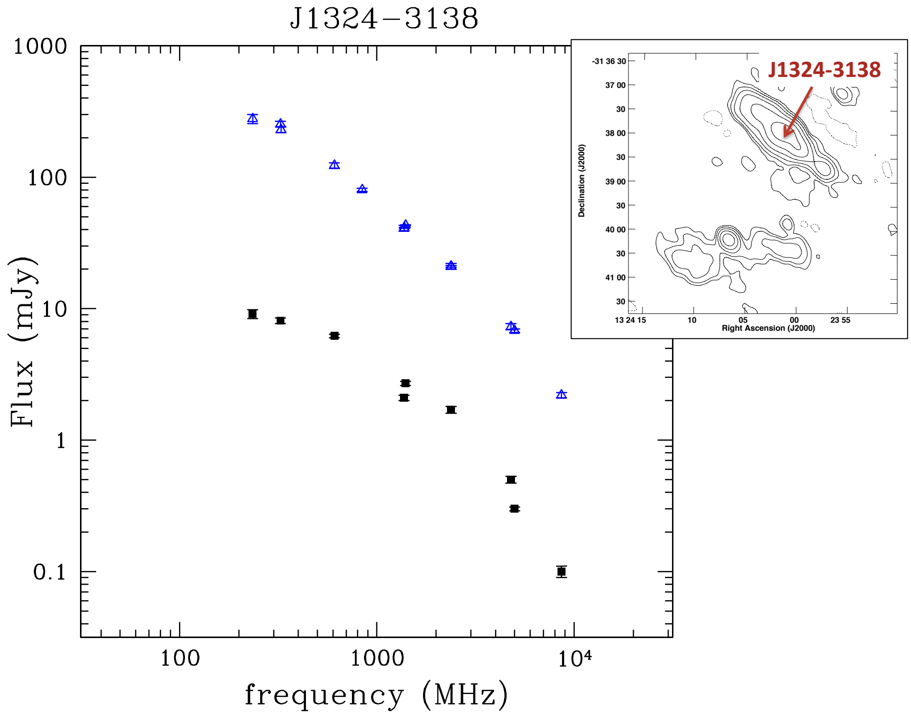

Figure 5.8: Integrated radio spectrum of J1324-3138. The filled squares represent the flux densities of the central region, while the open blue triangles represent the total flux densities. Such spectra are in good agreement with the work of Venturi et al. (1998).

Telescope	ν (MHz)	$S_{\rm tot}$ (mJy)	$S_{\rm c}$ (mJy)	$S_{\rm diff}$ (mJy)	Restoring beam (arcsec^2)	Ref.
GMRT	235	77.1 ± 6.2	18.6 ± 1.5	58.5 ± 6.4	20.83×16.17	$^{(a)}$
GMRT	325	84.6 ± 4.2	16.8 ± 0.8	67.8 ± 4.3	16.3×11.9	$^{(a)}$
GMRT	610	18.7 ± 0.9	10.9 ± 0.5	7.8 ± 1.0	12.86×7.2	$^{(a)}$
MOST	843	16.7 ± 0.5	-	-	82.0×43.0	$^{(b)}$
ATCA	1380	-	7.8 ± 0.2	-	6.0×10.1	$^{(b)}$
ATCA	1400	-	5.6 ± 0.2	-	10.18×5.95	$^{(c)}$
ATCA	2380	-	7.4 ± 0.2	-	3.4×5.3	$^{(b)}$
ATCA	5000	-	3.0 ± 0.1	-	20.0×10.0	$^{(c)}$

Table 5.9: J1324-3140. References: $^{(a)}$ Venturi et al. (in preparation); $^{(b)}$ Venturi et al. (1997); $^{(c)}$ATCA image (Venturi et al. 1997).

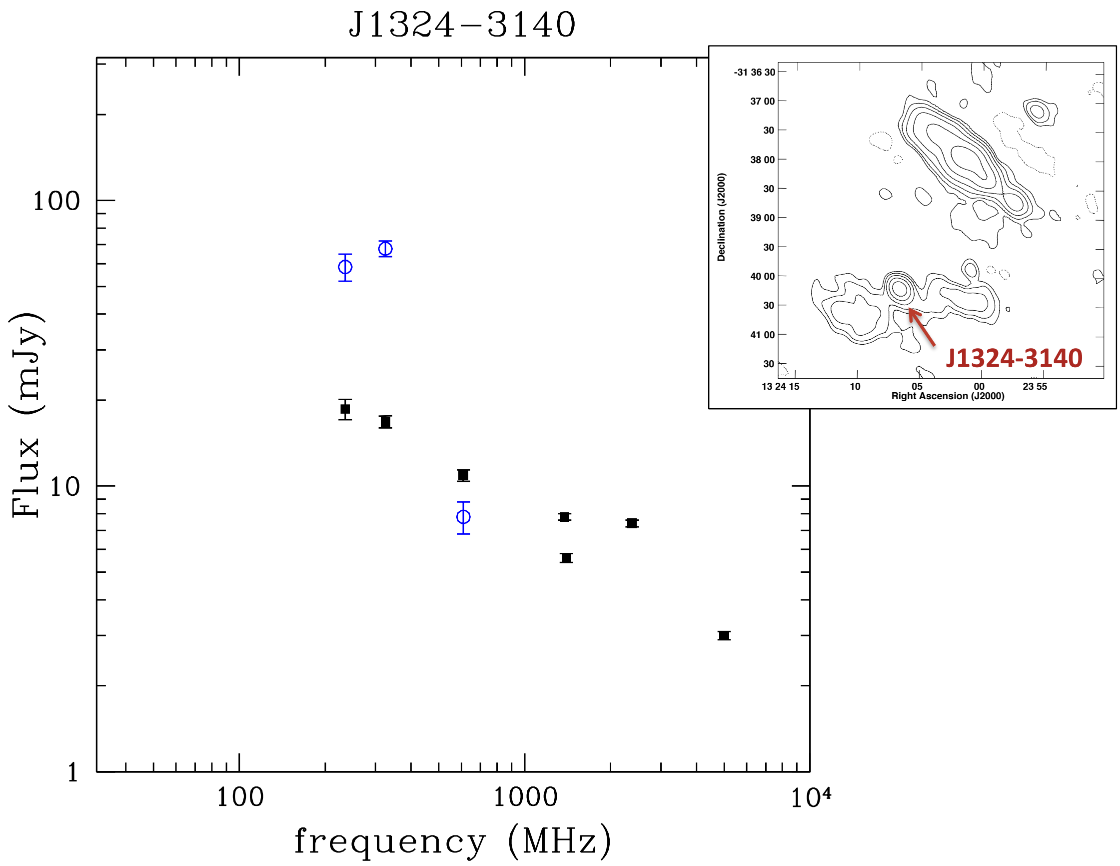

Figure 5.9: Integrated radio spectrum of J1324-3140. The filled squares represent the flux densities of the central region, while the open blue circles represent the flux densities of the diffuse emission. The ATCA at 2.4 GHz flux density is higher than the ones expected from the global slope of the data.

Telescope	ν (MHz)	S_c (mJy)	Restoring beam (arcsec^2)	Ref.
GMRT	235	19.1 ± 1.5	20.83×16.17	(a)
GMRT	325	17.9 ± 1.4	16.3×11.89	(a)
GMRT	610	14.6 ± 0.7	10.98×5.59	(a)
ATCA	1380	6.2 ± 0.2	10.0×5.0	(b)
ATCA	2380	1.5 ± 0.2	6.0×3.0	(b)

Table 5.10: J1327-3129b. References: (a) Venturi et al. (in preparation); (b) Venturi et al. (2000).

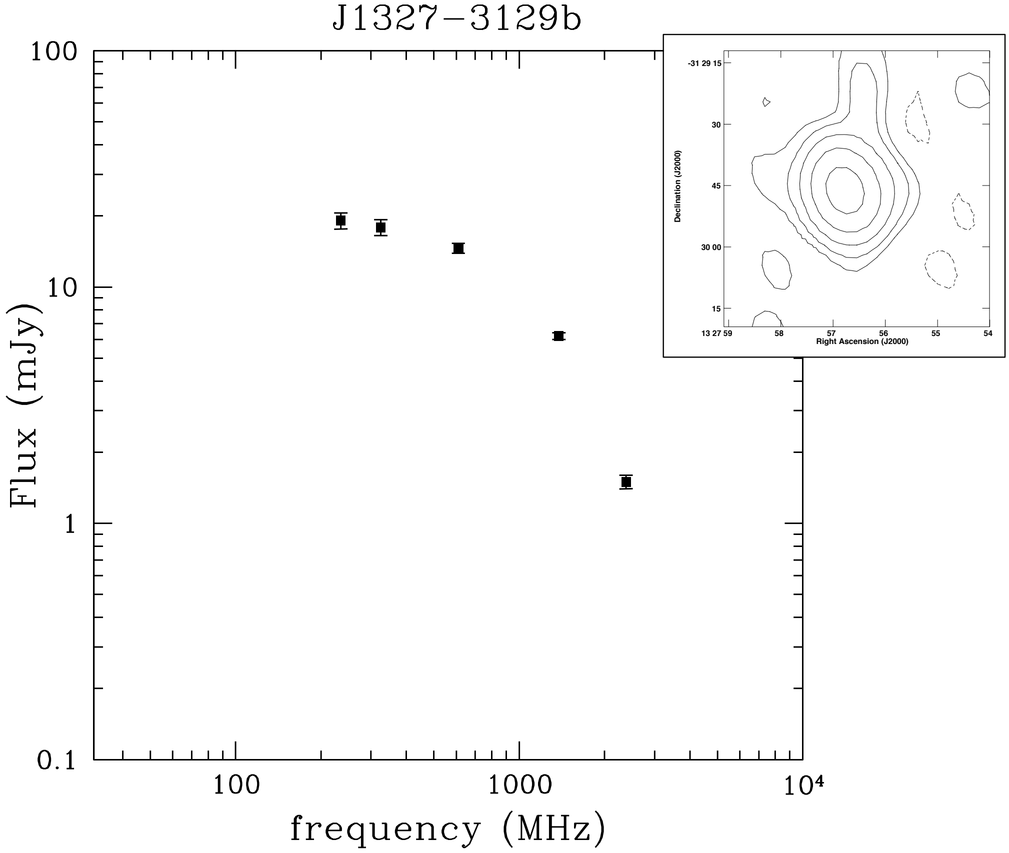

Figure 5.10: Integrated radio spectrum of J1327-3129b.

Telescope	ν (MHz)	$S_{\rm tot}$ (mJy)	$S_{\rm c}$ (mJy)	$S_{\rm diff}$ (mJy)	Restoring beam (arcsec^2)	Ref.
GMRT	235	389.8 ± 31.2	86.0 ± 6.9	303.8 ± 32.0	18.9×20.0	(a)
GMRT	327	247.6 ± 19.8	72.4 ± 5.8	175.2 ± 20.6	19.65×12.39	(a)
GMRT	610	205.7 ± 10.3	61.2 ± 3.1	144.5 ± 10.8	8.0×6.0	(a)
ATCA	1380	99.0 ± 3.0	-	-	10.0×5.0	(b)
ATCA	1400	99.9 ± 3.0	36.0 ± 1.1	63.9 ± 3.2	10.71×5.84	(c)
ATCA	2380	61.3 ± 1.8	-	-	6.0×3.0	(b)
ATCA	2400	55.6 ± 1.7	23.5 ± 0.7	32.1 ± 1.8	5.43×3.16	(c)
VLA	5000	-	24.8 ± 0.7	-	1.46×0.84	(d)
VLA	8400	-	13.6 ± 0.4	-	1.51×0.77	(d)

Table 5.11: J1333-3141. References: (a) Venturi et al. (in preparation); (b) Venturi et al. (2000); (c) ATCA image (Venturi et al. 2000); (d) VLA image (Venturi et al. 2003).

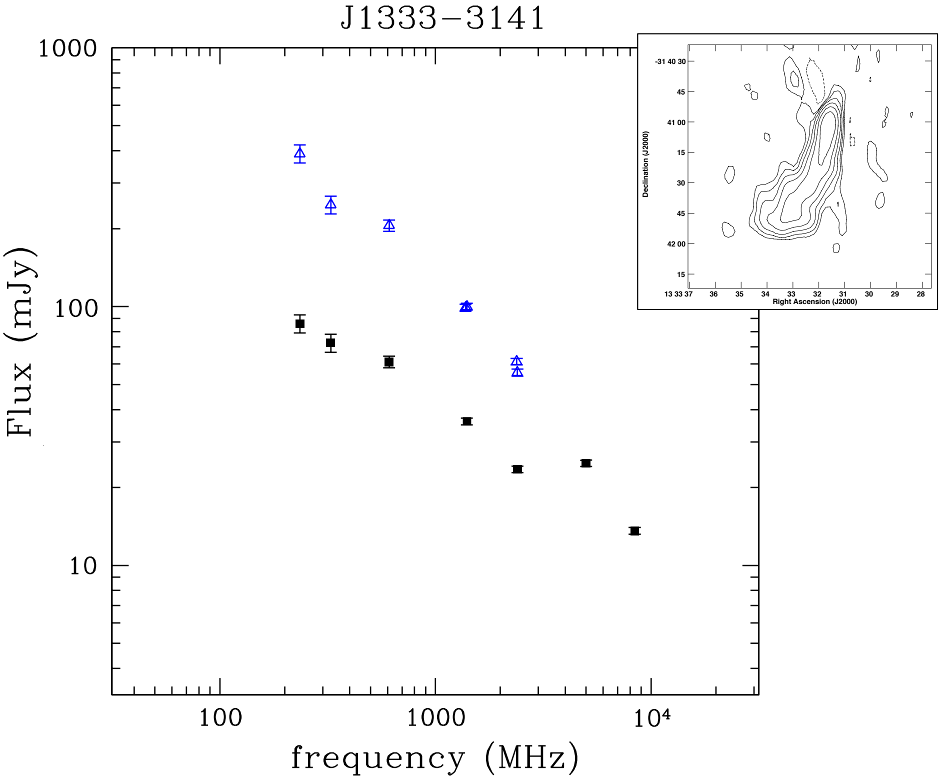

Figure 5.11: Integrated radio spectrum of J1333-3141. The filled squares represent the flux densities of the central region, while the open blue triangles represent the total flux densities.

Radiative model fit:

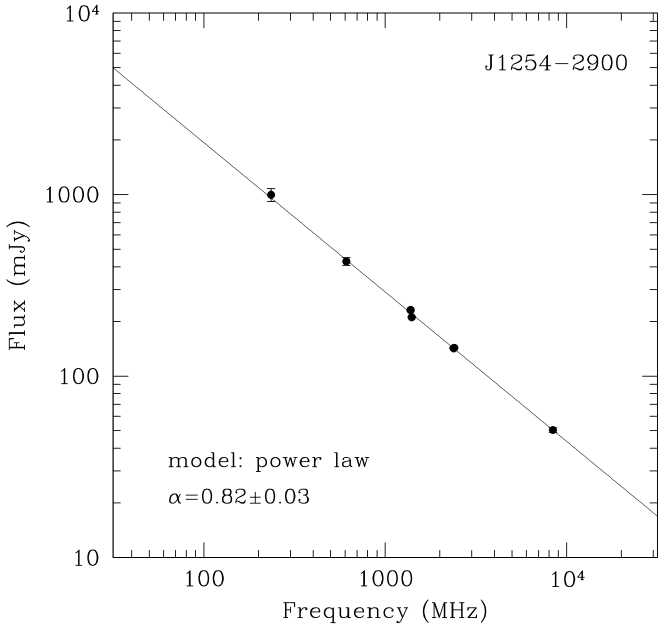

Figure 5.12: Best fit model of the J1254-2900 spectrum.

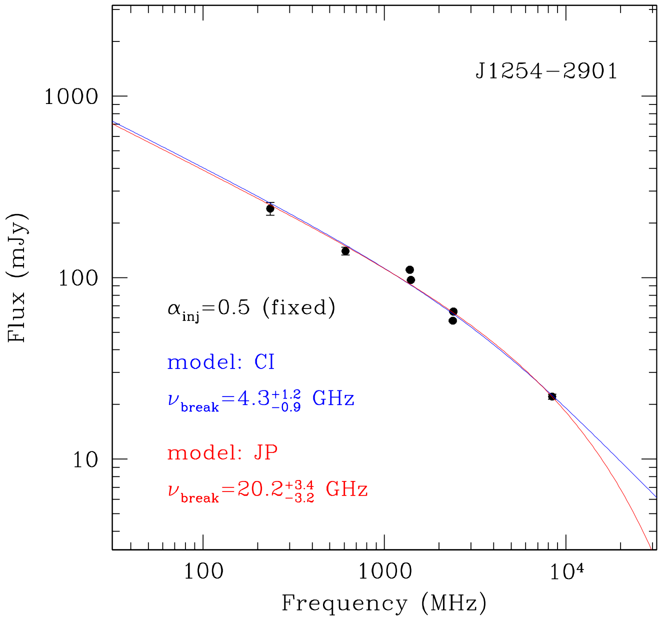

Figure 5.13: Best fit models of the J1254-2901 central region spectrum. The different colors represent the two radiative models used to fit the spectrum: the CI (blue) and the JP (red).

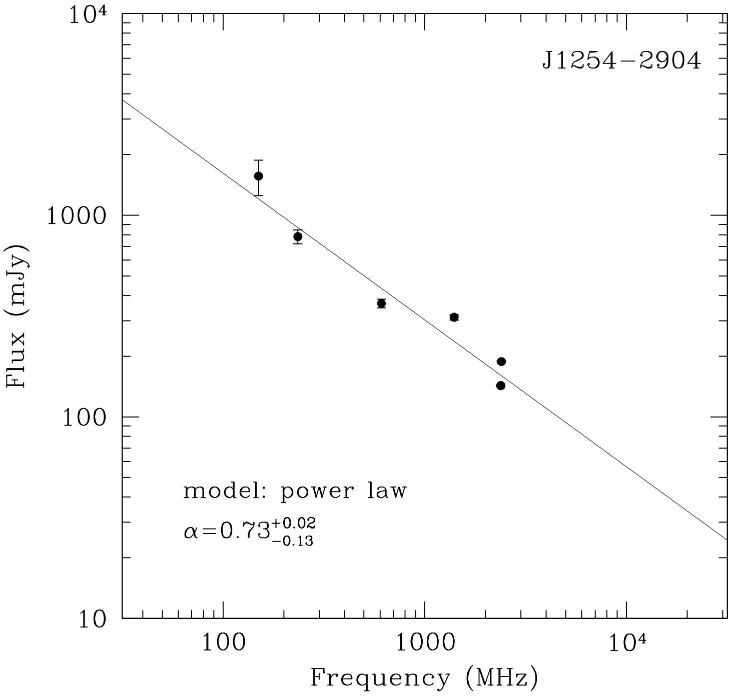

Figure 5.14: Best fit model of the J1254-2904 total spectrum.

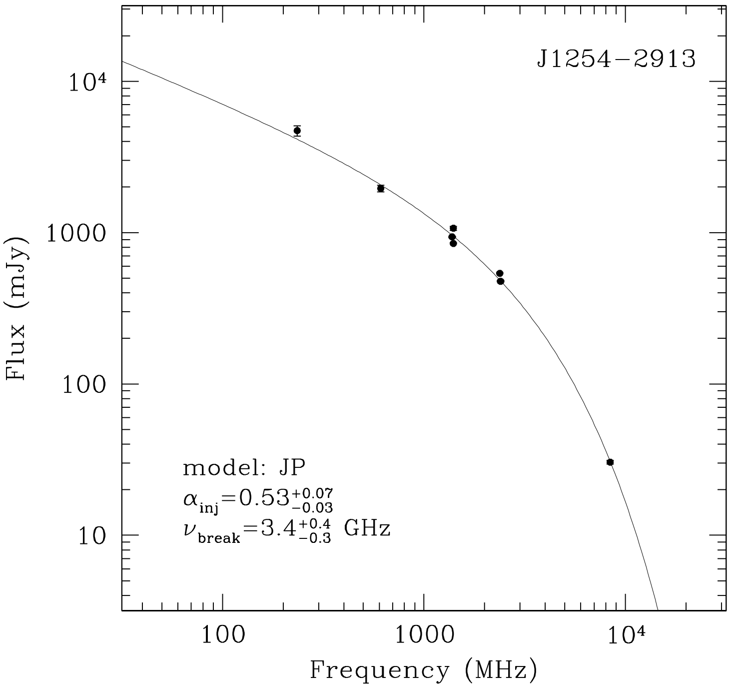

Figure 5.15: Best fit model of the J1254-2913 central region spectrum.

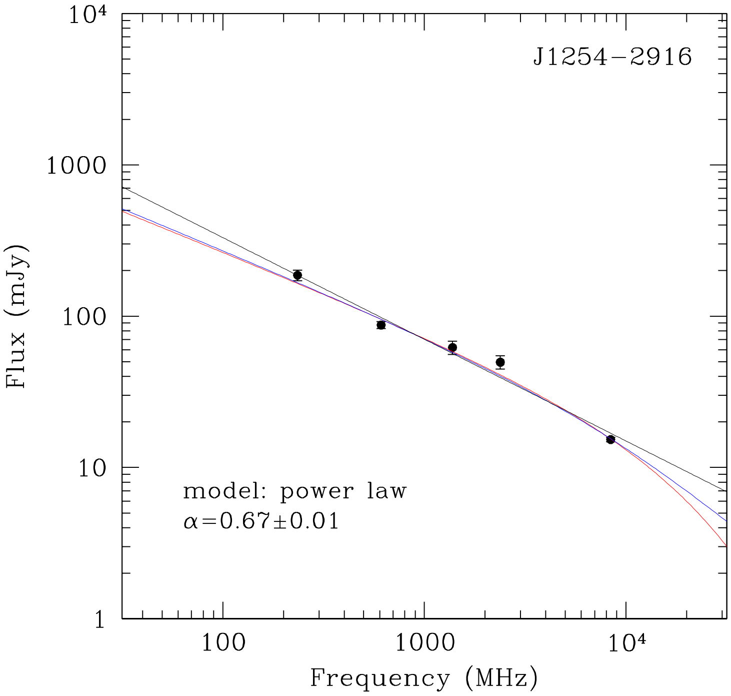

Figure 5.16: Best fit models of the J1254-2916 spectrum. The different colors represent the three radiative models used to fit the spectrum: the PL (black), the CI (blue) and the JP (red).

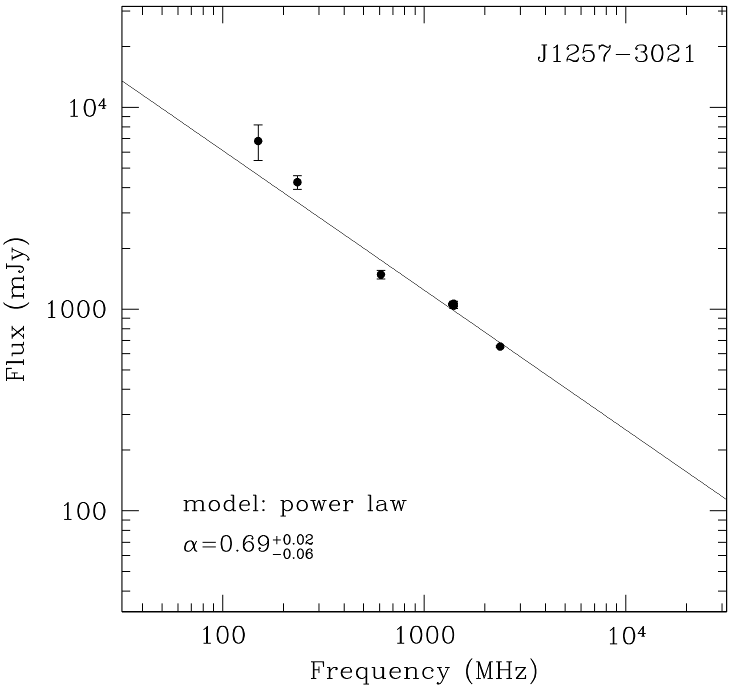

Figure 5.17: Best fit model of the J1257-3021 central region spectrum.

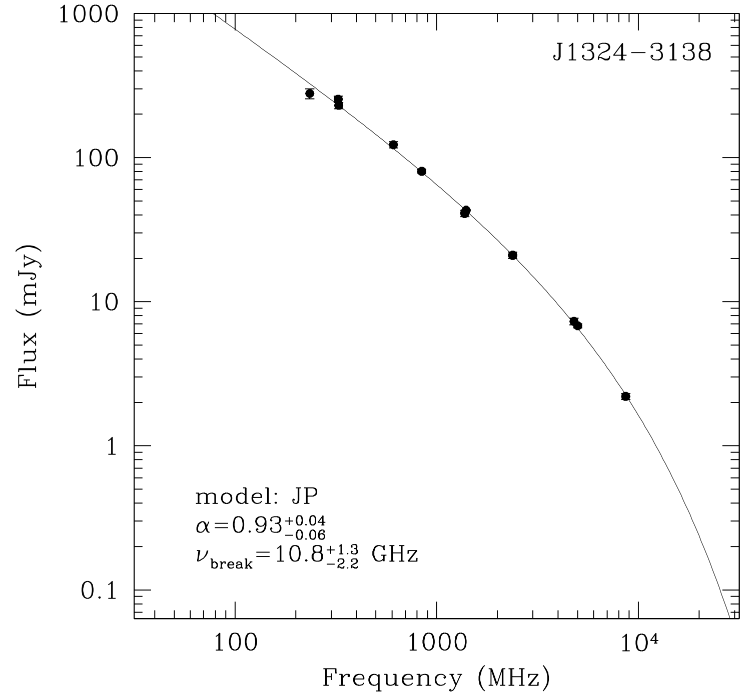

Figure 5.18: Best fit model of the J1324-3138 total spectrum.

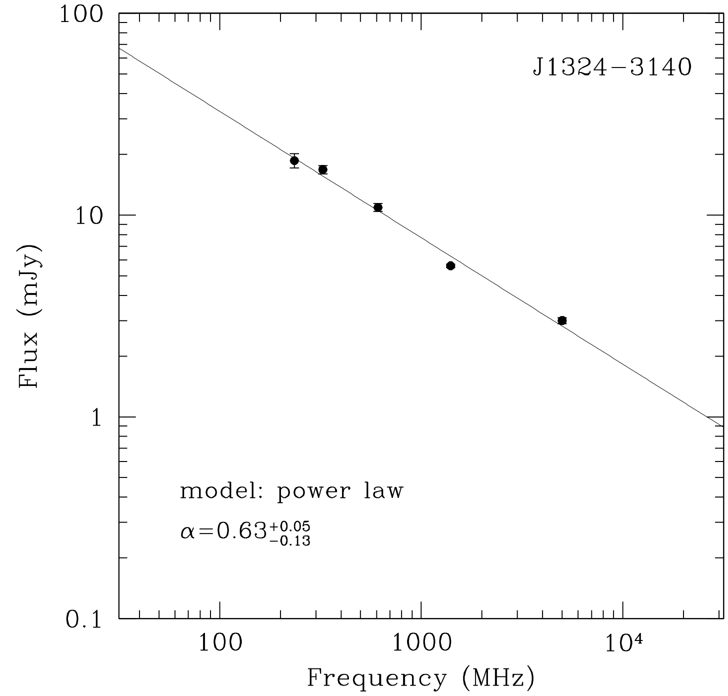

Figure 5.19: Best fit model of the J1324-3140 central region spectrum.

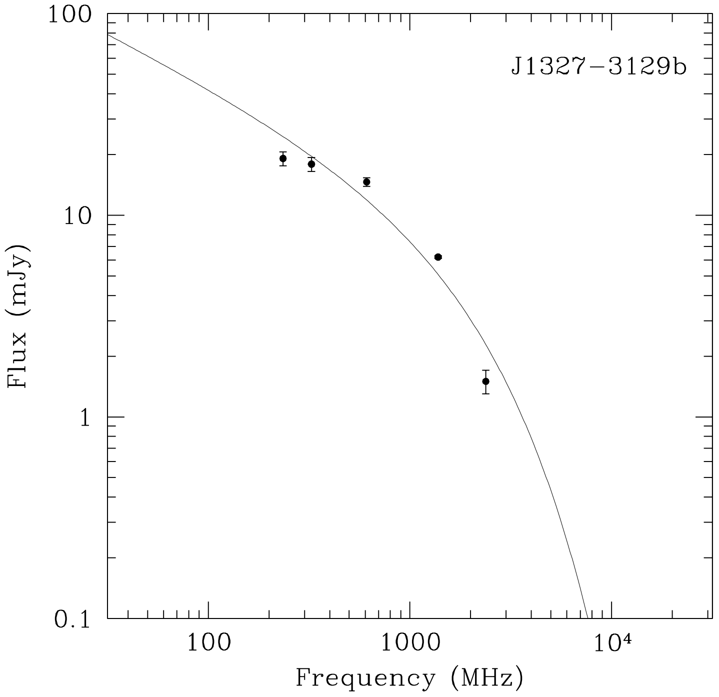

Figure 5.20: The J1327-3129b spectrum fitted with $\mathrm{CI_{OFF}}$ model.

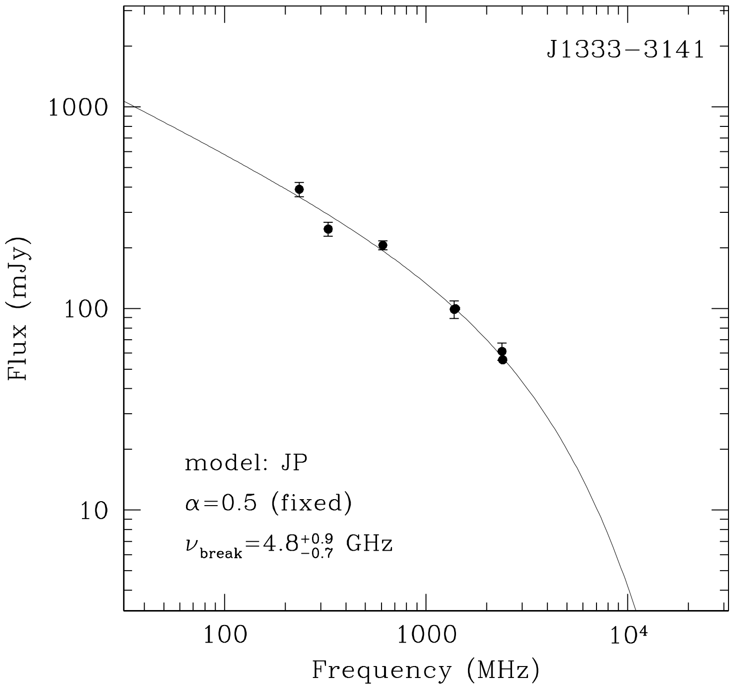

Figure 5.21: Best fit model of the J1333-3141 total spectrum.

Radio galaxy	rad. loss model	α_{inj}	χ^2_{red}	ν_{br} (GHz)
J1254-2900	PL	$0.82^{+0.03}_{-0.03}$	0.02	≥ 8.4
J1254-2901	JP	0.5*	3.92	$20.2^{+3.4}_{-3.2}$
J1254-2904	PL	$0.73^{+0.02}_{-0.13}$	1.22	≥ 8.4
J1254-2913	JP	$0.53^{+0.07}_{-0.03}$	3.68	$3.4^{+0.4}_{-0.3}$
J1254-2916	PL	$0.67^{+0.04}_{-0.04}$	0.63	≥ 8.4
J1257-3021	PL	$0.69^{+0.02}_{-0.06}$	5.50	≥ 8.4
J1324-3138	JP	$0.93^{+0.04}_{-0.06}$	1.34	$10.8^{+1.3}_{-2.2}$
J1324-3140	PL	$0.063^{+0.05}_{-0.13}$	0.20	≥ 8.4
J1327-3129b	undef.			
J1333-3141	JP	0.5*	2.92	$4.8^{+0.9}_{-0.7}$

Table 5.12: Best fit model of the radiative losses of the radio galaxy; * fixed α value.

The results of the radiative best fit models are listed in table 5.12. From this analysis, we make some considerations on the state of activity of the radio galaxy of the sample.

- **J1254-2900:**

  The cD radio galaxy of A3528 is a mini double radio galaxy that presents a distorted morphology at high frequencies. It is a "normal" active radio galaxy emitting via synchrotron radiation with a typical spectral index $\alpha = 0.82$ (figure 5.12).

- **J1254-12901:**

  It is a head-tail radio galaxy, where we can distinguish two regions of emission. The integrated spectrum of the central region is well described by both a JP and a CI model ($\chi^2_{\mathrm{red,\ JP}} = 3.92$ versus $\chi^2_{\mathrm{red,\ CI}} = 4.09$). The fit with best model is plotted in figure 5.13. The spectrum of the total emission and the tail were obtained also at low frequencies, and they are characterized by $\alpha^{235}_{610} = 0.66 \pm 0.07$ and $\alpha^{235}_{610} = 0.90 \pm 0.15$, respectively. It is interesting to note that the spectrum of the total emission is flatter than that of the tail, which implies that the central region is the dominant component of the whole radio galaxy.

- **J1254-2904:**

  It is a narrow-angle tail radio galaxy, and we can distinguish two regions of emission. The total spectrum is well fitted by a power-law with a typical spectral index ($\alpha = 0.73$, figure 5.14). Moreover, the measurement of the flux density at low frequencies (150, 235 and 610 MHz) allows the spectral analysis of the central and the diffuse regions. The former has a spectral index $\alpha_{610}^{150} = 0.77 \pm 0.25$, consistent with an active structure. The latter has a spectral index $\alpha_{610}^{150} = 1.14 \pm 0.35$, which indicates that the population of relativistic particles is aged.

- **J1254-2913:**

  The cD radio galaxy of A3528S is a wide-angle tail radio galaxy surronded by diffuse emission. The 8.4 GHz image of the source presented in chapter 4 (see left panel in figure 4.7) suggests that the core accounts for a tiny fraction of the total flux density. The spectrum of the central region (figure 5.15) is consistent with a nuclear structure which is in an active phase, even though the electron population is aging, as it is found for the radio emission associated with the BCGs. The spectral index of the total emission was obtained both with and without the 150 MHz value, and it is $\alpha_{610}^{150} = 1.36 \pm 0.25$ and $\alpha_{610}^{235} = 1.28 \pm 0.07$, respectively. The spectral index of the diffuse emission is very steep, $\alpha_{610}^{235} = 2.67 \pm 1.08$. Given that our flux density measurement at 610 MHz may understimate the real source flux density, the spectral index reported here could be an upper limit.

- **J1254-2916:**

  The spectrum of this head-tail radio galaxy can be fitted by both a power-law and the JP and CI radiative loss models (figure 5.16). The statisitical analysis marginally favours the PL ($\chi^2_{\text{red, PL}} = 0.63$ versus $\chi^2_{\text{red, JP}} = 4.18$ and $\chi^2_{\text{red, CI}} = 4.32$).

- **J1257-3021:**

  The spectrum of the central region in the cD radio galaxy of A3532 is consistent with an active structure (figure 5.17). This radio galaxy is characterized by the presence of diffuse emission in north-west direction, observed at 150, 235 and 610 MHz. The spectral index of this region is $\alpha_{610}^{150} = 2.77 \pm 0.25$, which implies a very old population of relativistic electrons. However, also in this case the flux density at 610 MHz may be undestimated, hence the spectral index may be not as steep as reported here.

- **J1324-3138:**

  The head-tail radio galaxy of A3556 was studied in detail by Venturi et al. (1998). The flux densities at low frequencies measured after the recent data analysis (Venturi et al., in preparation) agree with the previously fitted model of an aged radio source (figure 5.18 and figure 8 in Venturi et al. 1998). The spectrum of the central region (filled squares in figure 5.8) is not typical of the central engine in a radio loud AGN. In fact some spectral curvature and steep high frequency slope suggest that the radio emission has a substantial contribution from an aged population of relativistic electrons.

- **J1324-3140:**

  The spectral study of the cD radio galaxy of A3556 shows that it is not a simple compact source, as thought from the earlier high frequency images. Beyond the compact component associated with the nucleus of the cD, the low frequency observations (Venturi et al., in preparation) revealed the presence of a pair of symmetric lobes, whose spectral index is very steep. The flux density measurements presented here are obviously affected by some errors, whose origin is under investigation. Nevertheless, we can safely say that the two lobes have a very steep spectrum ($\alpha > 2$). However, it can not be neglected the possibility of a low flux density at 610 MHz. The spectrum of the central region (figure 5.19) is consistent with a compact source.

- **J1327-3129b:**

  The cD radio galaxy of A3558 is compact. Its spectrum could not be properly fitted by the radiative loss models considered in this work. The spectral indexes have been calculated into three frequency intervals, $\alpha_{610}^{235} = 0.28 \pm 0.07$, $\alpha_{1400}^{610} = 1.03 \pm 0.09$ and $\alpha_{2400}^{1400} = 2.63 \pm 0.50$. These values suggest that J1327-3129b is a very aged, possibly no longer active.

- **J1333-3141:**

  The spectrum of the whole head-tail radio galaxy was fitted by a JP model after fixing the spectral index (figure 5.21). The central region has an almost flat spectrum, obtained in a wide frequency range ($\alpha_{5000}^{235} = 0.41 \pm 0.04$), while the tail has a spectral index typical of an aged relativistic population ($\alpha_{2400}^{235} = 0.97 \pm 0.08$). This tailed radio galaxy is embedded in the radio halo of A3562 and the emission from the tail merges into the diffuse cluster radio emission.

5.3 Physical parameters

In order to estimate the radiative age of the radio galaxies, it is necessary to know the magnetic field values and the break frequencies of the spectra (equation 5.4). The latter is obtained by finding the model of radiative losses (KP, JP or CI) which is the best approximation of the spectral data (section 5.2.2). The former is found from the synchrotron luminosity $L_{\rm sync}$, even if it does not give an unambiguous value. Hence some assumptions must be made.

The magnetic field is estimated under the equipartition condition (Burbidge 1958), which minimizes the total energy content of a radio source emitting via synchrotron radiation. It is given by three components, electrons and protons ($E_{\rm part}$), and the magnetic field ($E_{\rm H}$):

$$E_{\rm tot} = E_{\rm part} + E_{\rm H}\,. \tag{5.7}$$

The two terms of the energy content are parametrized as follows:

$$E_{\rm H} = \frac{H^2}{8\pi}\Phi V \tag{5.8}$$

$$E_{\rm part} = E_{\rm e} + E_{\rm p} = (1+k)E_{\rm e} \tag{5.9}$$

where Φ is the filling factor, i.e. the fraction of the source volume occupied by the magnetic field, and V is the total volume of the radio source. The parameter k is a multiplicative factor between the electron ($E_{\rm e}$) and proton energies ($E_{\rm p}$). Generally it is assumed that the two population of particles have the same energy contribution, hence $k = 1$. The electron total energy calculated into the energy range $\varepsilon_1 \div \varepsilon_2$ is

$$E_{\rm e} = V \times \int_{\varepsilon_1}^{\varepsilon_2} \varepsilon N(\varepsilon) d\varepsilon = V \times N_0 \int_{\varepsilon_1}^{\varepsilon_2} \varepsilon^{-\delta+1} d\varepsilon \tag{5.10}$$

where $N(\varepsilon) = N_0 \varepsilon^{-\delta}$ is the typical initial distribution of electrons and the values of ε_1 and ε_2 are arbitrary. The constant VN_0 is related to the synchrotron (bolometric) luminosity, according to:

$$L_{\rm sync} = V \times \int_{\varepsilon 1}^{\varepsilon_2} \left(-\frac{d\varepsilon}{dt} \right) N(\varepsilon) d\varepsilon = c_2 (H \sin\theta)^2 V N_0 \int_{\varepsilon_1}^{\varepsilon_2} \varepsilon^{-\delta+2} d\varepsilon \tag{5.11}$$

hence, by eliminating VN_0, by writing ε_1 and ε_2 in terms of frequencies[2], and by assuming $\sin\theta = 1$, the electron total energy is:

$$E_{\rm e} = c_2^{-1} c_1^{1/2} \bar{c}(\alpha, \nu_1, \nu_2) L_{\rm sync} H^{-3/2} = c_{12}(\alpha, \nu_1, \nu_2) L_{\rm sync} H^{-3/2} \tag{5.12}$$

where $\bar{c} = \left(\frac{2\alpha-2}{2\alpha-1}\right) \frac{\nu_1^{(1-2\alpha)/2} - \nu_2^{1-2\alpha)/2}}{\nu_1^{(1-\alpha)} - \nu_2^{(1-\alpha)}}$ and $c_{12}(\alpha, \nu_1, \nu_2)$ a constant defined by Pacholczyk (1970). Hence, the electron energy can be expressed as a function of the synchrotron luminosity $L_{\rm sync}$, which is an observable, the strenght of the magnetic field H, and a constant which depends on the energy spectrum of the radiating electrons.

Finally, the total energy of a radio source emitting via synchrotron radiation is:

$$E_{\rm tot} = (1+k) c_{12} L_{\rm sync} H^{-3/2} + \frac{H^2}{8\pi} \Phi V \,, \tag{5.13}$$

which is a function of the magnetic field (figure 5.22). This distribution has a minimum value (found when $\partial E_{\rm tot}/\partial H = 0$) which is achieved when:

$$(1+k) E_{\rm e} = \frac{4}{3} E_{\rm H} \,, \tag{5.14}$$

which implies that the particle and magnetic energies must to be almost similar (*equipartition condition*). The minimum energy, expressed in erg, is therefore:

---

[2] The classical approach (Pacholczyk 1970) assumes $\nu_1 = 10$ MHz and $\nu_2 = 100$ GHz. In this thesis I chose $\nu_2 = 10$ GHz since after this frequency the spectra is very steep for almost all the radio galaxies and the energy content is very small (section 5.2.2). However, Brunetti et al. (1997) argued that it should be improved by using the Lorentz factors γ and not a fixed emitted frequency band $\nu_1 \div \nu_2$.

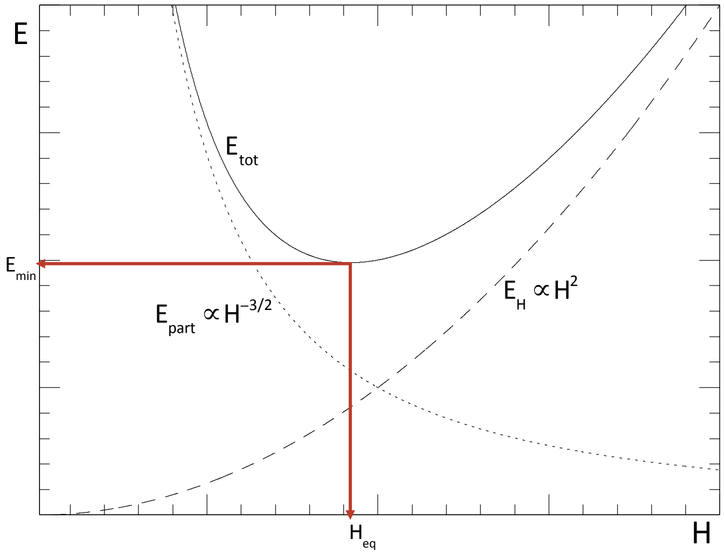

Figure 5.22: Energy content in a radio source: the solid line represents the total energy, the dashed line the magnetic energy and the dotted line the particle energy. The energy is minimum when $E_{\rm part}$ and $E_{\rm H}$ are almost equal (equipartition condition) and it correspond to $H_{\rm eq}$ (Govoni & Feretti (2004). The plot is in arbitrary units.

$$\begin{aligned} E_{\text{tot, min}} &= c_{13}\left(\frac{3}{4\pi}\right)^{3/7}(1+k)^{4/7}\Phi^{3/7}V^{3/7}L_{\rm sync}^{4/7} \\ &\approx 2.5\times10^{41}(1+k)^{4/7}P_{1.4\ \rm GHz}^{4/7}V^{3/7} \end{aligned} \tag{5.15}$$

where $c_{13} = 0.921 c_{12}^{4/7}$ (Pacholczyk 1970), $P_{1.4\ \rm GHz}$ is the monochromatic radio power expressed in W Hz^{-1}, V is expressed in kpc^3 and the filling factor is assumed $\Phi = 1$. The minimum energy density (erg cm^{-3}) is:

$$u_{\rm min} = \frac{E_{\text{tot, min}}}{V} = 8.6\times10^{-24}(1+k)^{4/7}\left(\frac{P_{1.4\ \rm GHz}}{V_{\rm kpc^3}}\right)^{4/7}. \tag{5.16}$$

The equipartition magnetic field, expressed in gauss (G), is obtained as:

$$H_{\rm eq} = \sqrt{\frac{24\pi}{7}u_{\rm min}}\,. \tag{5.17}$$

This value is assumed to be a good approximation of the (average) magnetic field of a radio source. It is important to note that it is based on strong approximations. First, the ratio between the electron and the proton energy, the k factor, is totally unknown. Second, the geometry of the source is usually chosen as simple as possible, and it is arbitrary in the third-dimension along the line of sight. Moreover, the choice to fix $\Phi = 1$ is probably an overstimate of the real volume occupied by the magnetic field: indeed, at high frequencies some sources show filamentary structures. Third, the energy range of emission ($\varepsilon_1 \div \varepsilon_2$) is not actually known. Last but not least, the validity of the equipartition condition itself is still debated. Despite all this, the equipartition condition is the best way to obtain at least an extimation of its order of magnitude.

Finally from the equation 5.16 and from the equipartition condition, we also obtain the internal pressure of the radio source, under the hypothesis of ordered magnetic field:

$$P_{\rm int} = P_{\rm m} + P_{\rm r} = u_{\rm H} + \frac{u_{\rm r}}{3} = \frac{3}{7}u_{\rm min} + \frac{1}{3}\left(\frac{4}{7}u_{\rm min}\right) = \frac{13}{21}u_{\rm min} \tag{5.18}$$

where $u_{\rm H}$ and $u_{\rm r}$ are the magnetic and relativistic energy densities respectively.

The physical parameters obtained for the radio galaxies of the sample are listed in table 5.13. The errors are not reported because they are dominated by the assumptions made during the extimation of the radio galaxy volume. The geometry assumed depends on the object, but it was generally chosen a prolate ellipsoid, i.e. an ellipsoid with the third-dimension equal to the minor semi-axis. The only exceptions are J1327-3129b and the inner region of J1324-3140, both unresolved sources for which a spherical geometry was used. Hence, the volume of the radio galaxies was obtained from the relation:

$$V = \begin{cases} \frac{\pi}{6}ab^2 & \text{(prolate ellipsoide)} \\ \frac{4\pi}{3}a^3 & \text{(sphere)} \end{cases} \quad {\rm kpc}^3 \tag{5.19}$$

where a and b are the major and the minor semi-axes of the ellipsoid respectively. They are expressed in kpc and are calculated by multiplying the angular size of the radio galaxy with a conversion factor f. The monochromatic luminosity $P_{1.4\ \rm GHz}$ is given by:

$$P_{1.4\ \rm GHz} = 4\pi D_{\rm lum}^2 S_{1.4\ \rm GHz} \quad {\rm W\ Hz^{-1}} \tag{5.20}$$

where $D_{\rm lum}$ is the luminosity distance expressed in Mpc, and $S_{1.4\ \rm GHz}$ is the flux density at 1.4 GHz. Both f and $D_{\rm lum}$ are obtained from the NASA/IPAC Extragalactic Database (http://ned.ipac.caltech.edu) after fixing the cosmology (flat

Universe, $H_0 = 70$ km s^{-1} Mpc^{-1}, $\Omega_m = 0.286$ and $\Omega_\Lambda = 0.714$).

The age of the radio galaxies are obtained from equation 5.4 and using the equipartition magnetic field (last column in table 5.13) and the break frequency found from the spectral analysis (last column in table 5.12). When the spectrum is modeled by a PL, we considered a lower limit for $\nu_{\rm br} = 8.4$ GHz, i.e. the last measurement in our dataset, while for J1327-3129b we chose $\nu_{\rm br} = 1.4$ GHz, i.e. the frequency that represents the last injection of electrons. The results are in table 5.13.

Radio galaxy	$S_{1.4\ \mathrm{GHz}}$ (mJy)	V (kpc^3)	D_{lum} (Mpc)	$P_{1.4\ \mathrm{GHz}}$ (W Hz^{-1})	$E_{\mathrm{tot,\ min}}$ (erg)	u_{min} (erg cm^{-3})	H_{eq} (G)	P_{int} (dyne cm^{-2})	t_{br} (Myr)
J1254-2900	230.9	7158	241	1.6×10^{24}	1.1×10^{57}	5.4×10^{-12}	7.6×10^{-6}	3.3×10^{-12}	21*
J1254-2901	110.0	4294	243	7.7×10^{23}	6.0×10^{56}	4.8×10^{-12}	7.2×10^{-6}	3.0×10^{-12}	15*
J1254-2904	311.7	63526	243	2.2×10^{24}	3.4×10^{57}	1.9×10^{-12}	4.5×10^{-6}	1.1×10^{-12}	36*
J1254-2913	1069.1	1043994	257	8.4×10^{24}	2.5×10^{58}	8.1×10^{-13}	3.0×10^{-6}	5.0×10^{-13}	71
J1254-2916	62.1	189980	214	3.4×10^{23}	7.1×10^{56}	1.3×10^{-12}	3.7×10^{-6}	7.9×10^{-13}	41*
J1257-3021	1061.7	50215	242	7.4×10^{24}	6.2×10^{57}	4.3×10^{-12}	6.8×10^{-6}	2.6×10^{-12}	24*
J1324-3138	43.1	238283	223	2.6×10^{23}	1.8×10^{57}	2.6×10^{-13}	1.7×10^{-6}	1.6×10^{-13}	42
J1324-3140	84.6	260646	213	4.6×10^{23}	2.6×10^{57}	3.4×10^{-13}	1.9×10^{-6}	2.1×10^{-13}	49*
J1327-3129b	6.2	6371	208	3.2×10^{22}	1.1×10^{56}	6.2×10^{-13}	2.6×10^{-6}	3.8×10^{-13}	116**
J1333-3141	99.9	7017	223	5.9×10^{23}	6.3×10^{56}	3.1×10^{-12}	5.8×10^{-6}	1.9×10^{-12}	38

Table 5.13: Physical parameters of the radio galaxies of the sample. * upper limit estimation of the radio galaxy age due to the non-identification of the real break frequency. ** the electron population age is calculated at 1.4 GHz, where the first steepening is seen, hence it is a lower limit.

CHAPTER 6

DISCUSSION AND CONCLUSIONS

The study in the radio band of the A3528 and the A3558 cluster complexes provides informations on two different aspects on the radio galaxies inside them. On one hand, the central dominant radio galaxies give information on the activity state in the central dense environment of the galaxy clusters. On the other, tailed radio galaxies are tracers of the motion of the host galaxies within the clusters, which take into account also the bulk flow motion in the cluster weather. In this study, information coming from the radio band and the one provided by the X-ray emission complement each other. In the following discussion, after a first analysis of the physical parameters of the radio galaxies (section 6.1) we consider the two cluster complexes individually (sections 6.2 and 6.3), highlighting some differences.

6.1 Considerations on the physical parameters

From the spectral analysis performed in the chapter 5, we can make some considerations on the physical parameters of the radio galaxies studied here; they can be summarized as follows:

- the radio powers are typical of cluster galaxies (e.g. Parma et al. 1999), covering the range $22 \lesssim \log P_{1.4\ \mathrm{GHz}} \lesssim 25$ W Hz^{-1} (table 5.13). The brightest objects are associated with the BCGs of the A3528 complex, while the weakest are associated with the radio galaxies belonging to the A3558 complex;
- the average magnetic fields, calculated over the whole radio source volume and under the assumption of the equipartition, are of the order of few μG.

These values agree with literature works (e.g. Parma et al. 1999), and can be considered typical of cluster radio galaxies;

- the internal pressures are of the order of $10^{-12} \div 10^{-13}$ dyne cm^{-2}, consistent with earlier studies (e.g. Feretti et al. 1992). We found that the lowest values are associated with the less powerful radio galaxies, i.e. in the A3558 complex and the tailed radio galaxies in the A3528 complex. Again, the values reported here are averaged over the source volume.

On the basis of these values and the spectral shape, we estimated the radiative age of the radio galaxies of the sample. We found that it spans about one order of magnitude, from tens to hundreds Myr, in agreement with literature works on cluster radio galaxies (e.g. Murgia et al. 2011).

Eventually, we found a different behaviour between the two cluster complexes, in both morphology and activity state of the radio galaxies.

6.2 The A3528 complex

The BCGs in A3528S and A3532, namely J1254-2913 and J1257-3021 respectively, are the most interesting radio galaxies from a morphological and spectral point of view. At low frequencies, they are both characterized by two regions with substantially different properties, and which we termed *central* and *diffuse* region, which can be described as follows:

- the surface brightness of the central component is much higher than that of the diffuse one;

- the intensity contours show that the inner part of the diffuse regioncan be interpreted in terms of a wide-angle tailed morphology; further the diffuse emission is spread over a larger scale;

- the spectral analysis shows that the central region is globally active and young, while the diffuse region has very steep spectrum ($\alpha > 2$), which indicates an aged population of relativistic electrons.

In the light of these observational pieces of evidence, we suggest that J1254-2913 and J1257-3021 may be examples of restarted activity in radio galaxies.

On the contrary, the BCG in A3528N, J1254-2900, is a rather small (its linear size is approximately 30 kpc) active radio galaxy, which show the same double morphology at any frequency.

The tailed radio galaxies bear information on the dynamical state of the complex. The most intriguing tailed radio galaxy is J1254-2904, which shows three different structures characterized by different spectral slopes: a very compact core, observable at the highest frequency only (right panel in figure 4.6); a central active region, which emits at all frequencies; an aged diffuse region, visible only at low frequencies. The tailed morphology of J1254-2901 instead probably suggests an interaction with the BCG in A3528N, which is distorted at high frequencies, although projection effects can not be excluded.

The comparison between the tailed radio galaxies and the X-ray surface brightness distribution (figure 6.2) provides information on the role of the ICM in the A3528 system. The morphology J1254-2916 suggests a motion from the south-west to the north-east direction. On the contrary, J1254-2904 seems to point northward and its complex structure suggests a likely influence of the ICM between A3528N and A3528S on the radio galaxy. Such morphology agrees with the motion of the intracluster medium proposed by Gastaldello et al. (2003), as derived from X-ray observations. Indeed, the analysis of the surface brightness residuals suggests a motion from north-east to south-west and from north-west to south-east direction for A3528S and A3528N respectively. Moreover, the peculiar morphology of the diffuse emission of J1254-2904 agrees with the hypothesis of a post tidal interaction between the two subclumps, proposed by the authors, rather than the early merger one (Bardelli et al. 2001).

Other intriguing features are suggested by the analysis of the X-ray intensity contours of A3532 (figure 6.1). From XMM-Newton observation, three depressions in the surface brightness are visible, to the north-west, south-east and west directions. The overlay between the thermal and non-thermal emission (figure 6.1) suggests that two of them could be filled by the diffuse emission and by the tail of J1257-3021, while the westerward one may be a ghost cavity. However, since its large angular resolution (14”), XMM-Newton is not the best instrument to investigate these structures. Lakhchaura et al. (2013) analysed the Chandra image of this cluster and found that probably only the depression to the north-west direction is really a cavity. A careful re-analysus of the Chandra data will be carried out after the thesis work.

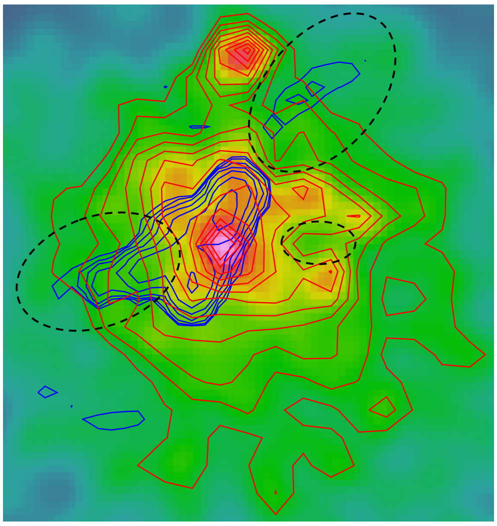

Figure 6.1: XMM-Newton image of A3532 (Gastaldello et al. 2003). The thermal intensity contours (red) are overlayed with the radio emission at 610 MHz (blue). Three depressions are suggested (black circles).

6.3 The A3558 complex

The cD radio galaxies of the A3558 cluster complex are very old. Indeed, we reveal no radio emission from the central dominant radio galaxy in A3562, which implies a completely dead radio source, while the one in A3558 has a radio spectrum with a progressive steepening, which is not fitted by simple aging models. Slee et al. (2001) suggested a modified KP/JP model for relic sources that takes into account both the aging of the earlier and the injection of a second population of electrons before the switch-off (KGKP and KGJP models, Kommissarov & Gubanov, 1994). We aim to try to fit the spectral data with these models in a future step. In contrast to these two BCGs, J1324-3140 in A3556 is characterized by a compact active central region, and two aged symmetrical lobes that reveal their presence only at low frequencies ($\nu < 610$ MHz). As for the BCGs in the A3528 complex, we suggest that it is a possible restarted radio galaxy.

The overlay between the thermal and non-thermal emission (figure 6.3) underlines that in radio band the complex is globally less active than the A3528 one. The BCG in A3562 is radio quiet, while the BCG in A3558 is a weak radio source. Furthermore, we want to stress the presence of a candidate relic found by Venturi et al. (in preparation) by plotting it on the XMM-Newton image. Its position is intriguing since it is located where major merging processes seem to have taken place; they deserve deep analysis.

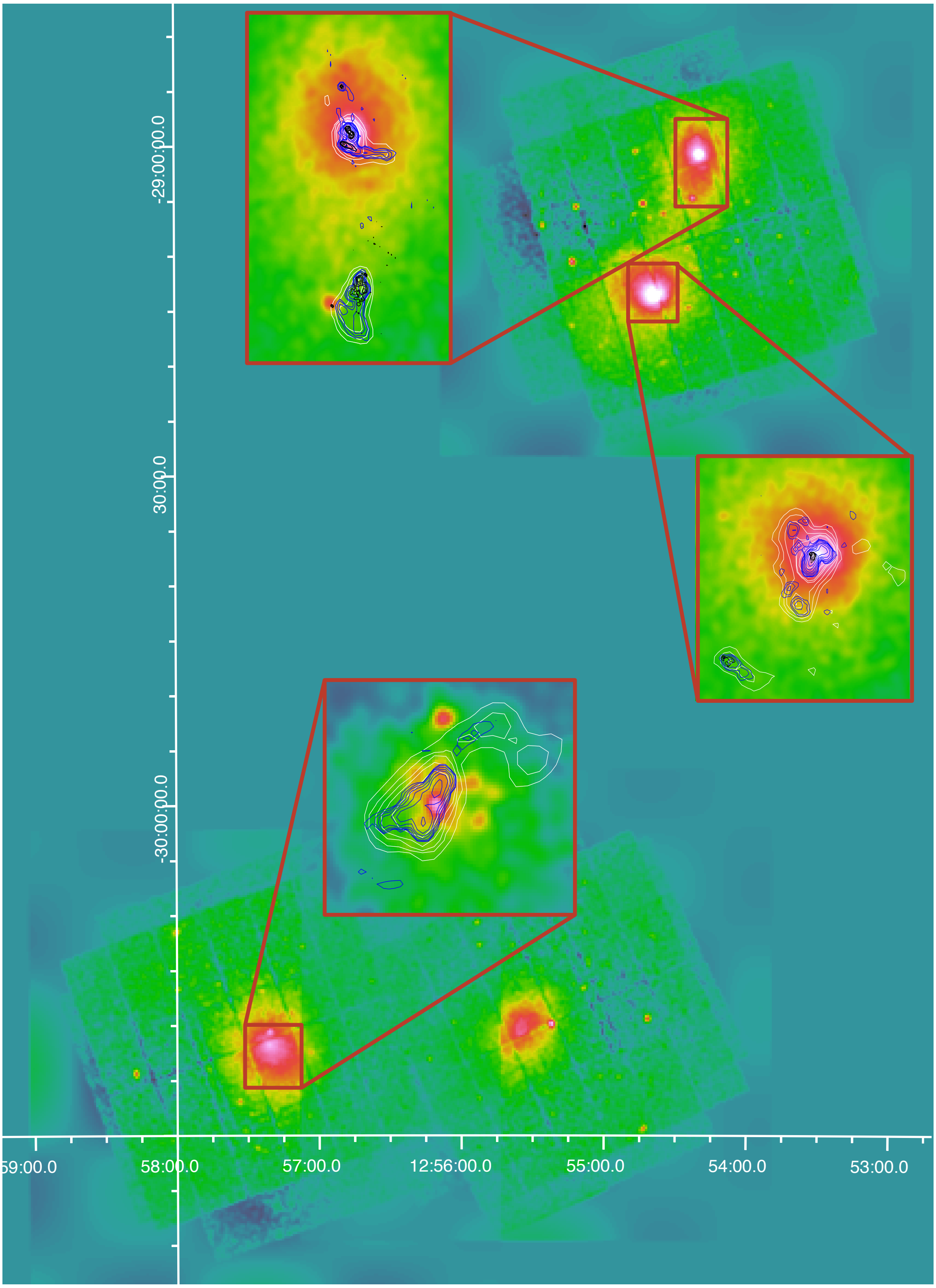

Figure 6.2: XMM-Newton image of A3528 complex (colours). From top to bottom: A3528N, A3528S, A3532 (left) and A3530 (right). In the red boxes there are enlargements on the cluster central regions. The radio contours are in white for the GMRT 235 MHz, in blue for the GMRT 610 MHz and in black for the VLA 8.4 GHz.

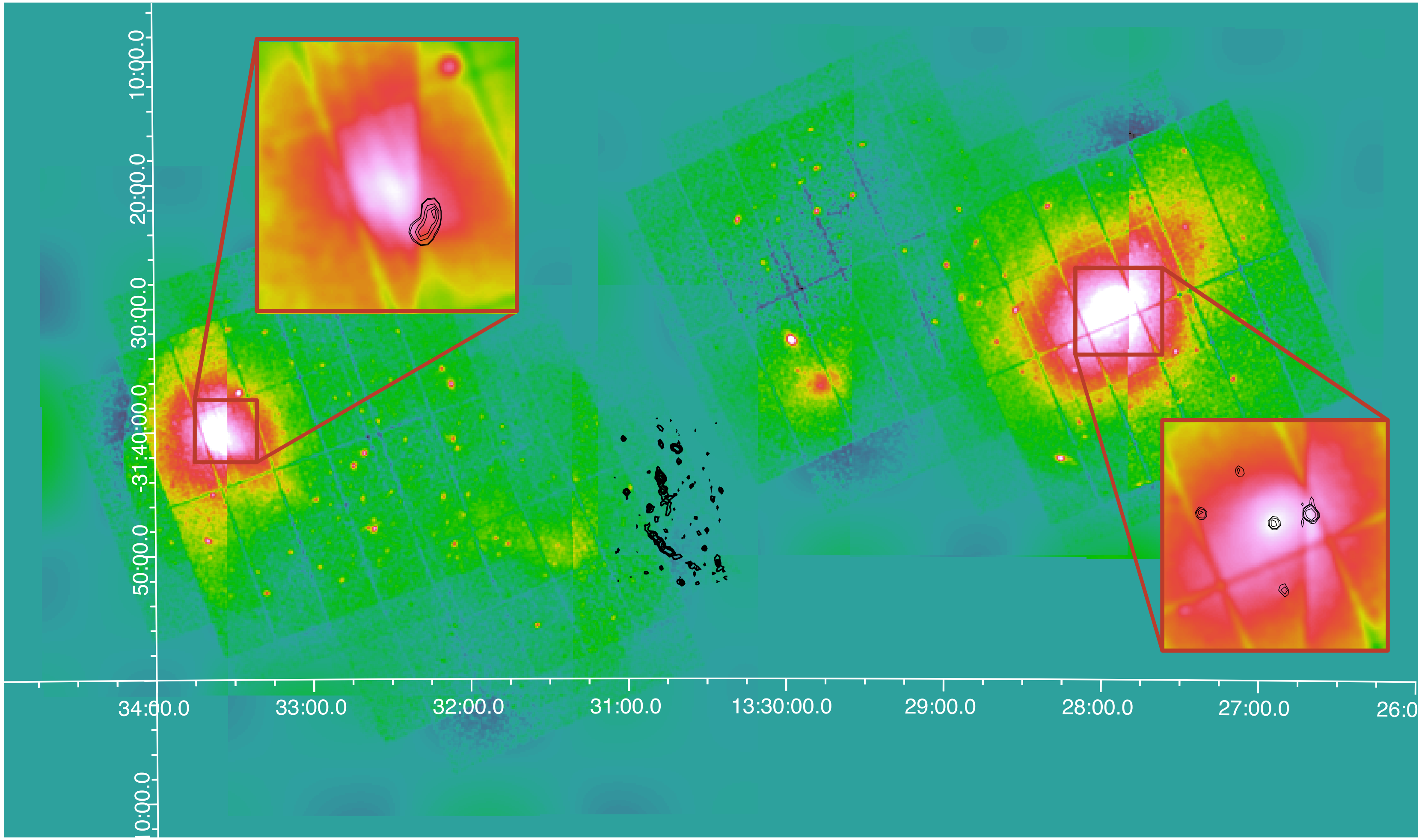

Figure 6.3: XMM-Newton image of A3562 (left), SC 1329-313 (the middle bright spot) and A3558 (right). In the red boxes there are enlargements on the cluster central region. We stress the presence of the serendipitous radio sources found in the westerward of A3562 (Venturi et al., in preparation). The radio contours are at 325 MHz.

6.4 Conclusions and future goals

The aim of this thesis was to study the radio properties of the radio galaxies in the A3528 and A3558 complexes and understand the origin and their different properties of the radio emission in the two complexes, both located in the very dense environment of the Shapley Concentration Core. Moreover, we investigated whether the environment could play a significant role in the observed differences. In this thesis, we drew our attention on the study of the extended radio galaxies.

We analysed GMRT low frequency data at 235 and 610 MHz complemented with propriertary and literature high frequency observations, to perform a spectral study over a wide frequency range, from 150 MHz to 8.4 GHz. Our sample consists of a total of ten radio galaxies, six of them located in the A3528 complex and the remaining four in the A3558 complex. Where possible, we separated the contribution of the central, compact emission from the extended one on a larger scale, either in the form of radio tails or diffuse morphology. We fitted the radio spectra and performed a study of the radiative age of the sources. We also made a qualitative comparison between the radio properties and the morphology of the X-ray emission as detected by XMM-Newton, which traces the ICM and bears information on the cluster dynamics. Finally we compared the overall properties of the radio galaxies whitin A3528 and A3558 complexes.

Our results can be summarized as follows:

- two BCGs in the A3528 complex (A3528S and A3532) show an active region which is surronded by extended steep-spectrum aged emission. We suggest that these could be two examples of restarted radio galaxies. On the contrary, the BCG in A3528N is a mini double radio galaxy which is in active phase.

- the BCGs in the A3558 complex show very different properties. The BCG in A3558 is weak and has very steep spectrum, suggesting that the radio emission is dying. The BCG in A3562 is radio quiet in all our dataset at any frequency. Finally, the BCG in A3556 shows signs of a possibly restarted activity, with a compact active nucleus and two steep spectrum lobes detected symmetrically from the nuclear emission.

- Two radio tails in A3528 complex (J1254-2904 and J1254-2916) are bearing valuable information on the dynamical history and present state of the system A3528N-A3528S. J1254-2904 shows three separate components of emisison (the core, the central region and the diffuse region) which trace a likely motion to the north. We propose that the radio plasma in this galaxy has been affected by the interaction with cluster weather in the ICM. The direction of the tail in J1254-2916 is consistent with the dynamical picture proposed by Gastaldello et al. (2003), i.e. gas motion from east to west. The third tailed radio galaxy, J1254-2901 in A3528N, is probably interacting with its nearby BCG, as suggested by its distorted morphology.

Recently, Kale et al. (2015) found that nuclear radio properties of BCGs are strongly dependent on the central properties of the host cluster and that the probability to find a radio loud AGN is higher in relaxed systems. According to that, we propose that the different AGN radio activity in these two complexes is related to their different merging stages.

In the A3528 complex the individual clusters have not crossed each other, and their nuclear regions have not been destroyed as yet. It is confirmed by the precence of cool-cores (figure 2.11, Gastaldello et al. 2003), indication of relaxed system. At the same time the gas has signature of tidal interactions, which affects the morphology of the extended more peripherical radio galaxies.

The A3558 complex is thought to have undergone a major distructive merger, particularly active in the region between A3562 and A3558, which has distrupted or at least quenched the radio emission propierties of the BCGs and has significantly reduced the AGN activity in this region. In agreement with the hypothesis of non-relaxed clusters, there is no evidence of cool-cores (figure 2.5, Markevitch & Vikhlinin 1997 and Ettori et al. 2000). A3556 does not seem to have been involved in this major merger event, and indeed its properties are similar to the clusters in the A3528 complex.

This thesis represents an intermediate step of a broader work that will be continued in next months.

From a radio point of view, a low resolution imaging of the GMRT dataset is needed to better characterize the substructures. These are the cases of the diffuse emission of J1254-2013 in the A3528S and J1257-3021 in the A3532 at 610 MHz, and the serendipitous radio sources found westerward of A3562 (see figure 2.7, Venturi et al., in preparation). Moreover, the Shapley Concentration Core will be observed at high frequency (1400 MHz) with the **ASKAP-EMU survey**, which combines an improvement in sensitivity (≈ 10 μJy/beam) and u-v spacing with large field of view capabilities ($5^\circ \times 5^\circ$), required to cover the whole complex. Among the others goals, the aim is to detect possible ultrasteep spectrum diffuse emission in the A3558 complex and extended low brightness emission around the central dominant galaxies of the clusters in the Shapley Concentration Core.

From an X-ray point of view, a deep analysis of the central regions of the galaxy clusters is essential to understand the interplay between the thermal and non-thermal emission. Hence, we aim to produce the residual image of surface brightness distribution of the intracluster gas in the A3528 cluster complex and compare it with the non-thermal emission of radio galaxies. Moreover, since in A3532 the XMM image suggests the presence of cavities, the following step is to analyse the available Chandra data (observation for 10 ks provided by Murray), whose small angular resolution could provide a better match for investigating the cluster substructures.

The preliminary results of this thesis have been presented in a poster at the fourth "Galaxy Evolution and Environment" international conference on November 30 and December 1-2 at Osservatorio Astronomico di Capodimonte (OAC) in Naples (Italy) with the title:

COSMIC DANCE IN THE SHAPLEY CONCENTRATION

Di Gennaro G., Venturi T., Dallacasa D., Bardelli S., Giacintucci S.

BIBLIOGRAPHY

Abell, G. O. 1958, ApJS, 3, 211

Abell, G. O. 1965, ARA&A, 3, 1

Abell, G. O. 1975, Stars and Stellar System IX: Galaxies and the Universe

Abell, G. O., Corwin, H. G. J., & Olowin, R. P. 1989, ApJS, 70, 1

Bahcall, N. A. 1977, ARA&A, 15, 505

Baldi, A., Bardelli, S., & Zucca, E. 2001, MNRAS, 324, 509

Bardelli, S., De Grandi, S., Ettori, S., et al. 2002, A&A, 382, 17

Bardelli, S., Zucca, E., & Baldi, A. 2001, MNRAS, 320, 387

Bardelli, S., Zucca, E., Malizia, A., et al. 1996, A&A, 305, 435

Bardelli, S., Zucca, E., Vettolani, G., et al. 1994, MNRAS, 267, 665

Bardelli, S., Zucca, E., Zamorani, G., Moscardini, L., & Scaramella, R. 2000, MNRAS, 312, 540

Bardelli, S., Zucca, E., Zamorani, G., Vettolani, G., & Scaramella, R. 1998, MNRAS, 296, 599

Bautz, L. P. & Morgan, W. W. 1970, ApJ, 162, L149

Bliton, M., Rizza, E., Burns, J. O., Owen, F. N., & Ledlow, M. J. 1998, MNRAS, 301, 609

Bock, D. C. J., Large, M. I., & Sadler, E. M. 1999, AJ, 117, 1578

Briggs, D. S. 1999, in Synthesis imaging in Radio Astronomy, ed. G. B. Taylor, C. L. Carilli, & R. A. Perley (ASP Conference Series), 11–36

Brunetti, G. 2002, arXiv:astro-ph/0207671

Brunetti, G., Cassano, R., Dolag, K., & Setti, G. 2009, A&A, 507, 661

Brunetti, G. & Jones, T. W. 2014, International Journal of Modern Physics D, 23, 1430007

Brunetti, G., Setti, G., & Comastri, A. 1997, A&A, 325

Brunetti, G., Setti, G., Feretti, L., & Giovannini, G. 2001, MNRAS, 320, 365

Burbidge, G. R. 1958, ApJ, 129, 841

Burns, J. O. 1998, Science, 280, 400

Byram, E. T., Chubb, T. A., & Friedman, H. 1966, Science, 152, 66

Cassano, R., Ettori, S., Giacintucci, S., et al. 2010, ApJ, 721, L82

Cassano, R., Gitti, M., & Brunetti, G. 2008, A&A, 486, L31

Cavaliere, A. & Fusco-Femiano, R. 1976, A&A, 49, 137

Cavaliere, A. & Fusco-Femiano, R. 1978, A&A, 70, 677

Chandra, P., Ray, A., & Bhatnagar, S. 2004, ApJ, 612, 974

Chiaberge, M., Gilli, R., Lotz, J. M., & Norman, C. 2015, ApJ, 806, 147

Colberg, J. M., White, S. D. M., Jenkins, A., & Pearce, F. R. 1999, MNRAS, 308, 593

Condon, J. J., Cotton, W. D., Greisen, E. W., et al. 1998, AJ, 115, 1693

Cornwell, T. 1999a, in Synthesis imaging in Radio Astronomy, ed. G. B. Taylor, C. L. Carilli, & R. A. Perley (ASP Conference Series), 151–170

Cornwell, T. 1999b, in Synthesis imaging in Radio Astronomy, ed. G. B. Taylor, C. L. Carilli, & R. A. Perley (ASP Conference Series), 187–199

Dallacasa, D., Feretti, L., Giovannini, G., & Venturi, T. 1989, A&AS, 79, 391

De Filippis, E., Schindler, S., & Erben, T. 2005, A&A, 444, 387

De Grandi, S. & Molendi, S. 2002, ApJ, 567, 163

Edge, A. C., Stewart, G. C., Fabian, A. C., & Arnaud, K. A. 1990, MNRAS, 245, 559

Eilek, J. A., Burns, J. O., O'Dea, C. P., & Owen, F. N. 1984, ApJ, 278, 37

Ettori, S., Bardelli, S., De Grandi, S., et al. 2000, MNRAS, 318, 239

Ettori, S., Fabian, A. C., & White, D. A. 1997, MNRAS, 289, 787

Fabian, A. C. & Nulsen, P. E. J. 1977, MNRAS, 180, 479

Fanaroff, B. L. & Riley, J. M. 1974, MNRAS, 167, 31P

Fanti, R. 1984, Clusters and Groups of Galaxy

Feretti, L. 2003, arXiv:astro-ph/0301576

Feretti, L., Giovannini, G., Govoni, F., & Murgia, M. 2011, in IAU Symposium, Vol. 274, Advances in Plasma Astrophysics, ed. A. Bonanno, E. de Gouveia Dal Pino, & A. G. Kosovichev, 340–347

Feretti, L., Giovannini, G., Govoni, F., & Murgia, M. 2012, A&A Rev., 20, 54

Feretti, L., Giovannini, G., Klein, U., et al. 1998, A&A, 331, 475

Feretti, L., Perola, G. C., & Fanti, R. 1992, A&A, 265, 9

Feretti, L. & Venturi, T. 2002, in Merging Processes in Galaxy Clusters, ed. L. Feretti, I. M. Gioia, & G. Giovannini (Kluwer Academic Publisher), 163–195

Fritz, G., D. A., Meekins, J. F., & Friedman, H. 1971, ApJ, 164, L81

Giacintucci, S., Markevitch, M., Venturi, T., et al. 2014, ApJ, 781, 9

Giacintucci, S. & Venturi, T. 2009, A&AP, 505, 55

Giacintucci, S., Venturi, T., Bardelli, S., Dallacasa, D., & Zucca, E. 2004, A&A, 419, 71

Giacintucci, S., Venturi, T., Brunetti, G., et al. 2005, A&A, 440, 867

Giacintucci, S., Venturi, T., Macario, G., et al. 2008, A&A, 486, 347

Gitti, M., Brighenti, F., & McNamara, B. R. 2012, Advances in Astronomy, 2012, 950641

Gitti, M., Brunetti, G., & Setti, G. 2002, A&A, 386, 456

Govoni, F. & Feretti, L. 2004, International Journal of Modern Physics D, 13, 1549

Gregorini, L., de Ruiter, H. R., Parma, P., et al. 1994, A&AS, 106

Hanami, H., Tsuru, T., Shimasaku, K., et al. 1999, ApJ, 521, 90

Jaffe, W. J. & Perola, G. C. 1973, A&A, 26, 423

Kale, R., Venturi, T., Cassano, R., et al. 2015, A&A, 581, A23

Kardashev, N. S. 1962, Soviet Ast., 6, 317

Kellermann, K. I., Sramek, R., Schmidt, M., Shaffer, D. B., & Green, R. 1989, AJ, 98, 1195

Komissarov, S. S. & Gubanov, A. G. 1994, A&A, 285

Kull, A. & Böhringer, H. 1999, A&A, 341, 23

Lakhchaura, K., Singh, K. P., Saikia, D. J., & Hunstead, R. W. 2013, ApJ, 767, 91

Lane, W. M., Kassim, N. E., Ensslin, T. A., Harris, D. E., & Perley, R. A. 2002, AJ, 123, 2985

Large, M. I., Mathewson, D. S., & Haslam, C. G. T. 1959, Nature, 183, 1663

Ledlow, M. J. & Owen, F. N. 1996, AJ, 112, 9

Mao, M. Y., Sharp, R., Saikia, D. J., et al. 2010, MNRAS, 406, 2578

Markevitch, M. 1998, ApJ, 504, 27

Markevitch, M. & Vikhlinin, A. 1997, ApJ, 474, 84

Mathews, W. G. & Brighenti, F. 2008, ApJ, 676, 880

Mazzotta, P. & Giacintucci, S. 2008, ApJ, 675, L9

McNamara, B. R. & Nulsen, P. E. J. 2007, ARA&A, 45, 117

Meekins, J. F., Fritz, G., Chubb, T. A., & Friedman, H. 1971, Nature, 231, 107

Melnick, J. & Moles, M. 1987, RMxAA, 14, 72

Merluzzi, P., Busarello, G., Haines, C. P., et al. 2015, MNRAS, 446, 803

Metcalfe, N., Godwin, J. G., & Peach, J. V. 1994, MNRAS, 267, 431

Miley, G. 1980, ARA&A, 18, 165

Miley, G. K., Perola, G. C., van der Kruit, P. C., & van der Laan, H. 1972, Nature, 237, 269

Murgia, M. 1999, PhD thesis

Murgia, M. 2001, PhD thesis

Murgia, M., Fanti, C., Fanti, R., et al. 1999, A&A, 345, 769

Murgia, M., Parma, P., de Ruiter, H. R., & Fanti, R. 2000, in Perspective on Radio Astronomy: Science with Large Antenna Arrays

Murgia, M., Parma, P., Mack, K. H., et al. 2011, A&A, 526, A148

Myers, S. T. & Spangler, S. R. 1985, ApJ, 291, 52

Napier, P. J. 1999, in Synthesis imaging in Radio Astronomy, ed. G. B. Taylor, C. L. Carilli, & R. A. Perley (ASP Conference Series), 37–56

O'Dea, C. P. 1984, PhD thesis

O'Dea, C. P. & Owen, F. N. 1985, AJ, 90, 954

O'Donoghue, A. A., Eilek, J. A., & Owen, F. N. 1993, ApJ, 408, 428

Pacholczyk, A. G. 1970, Radio astrophysics. Nonthermal processes in galactic and extragalactic sources

Parma, P., Murgia, M., de Ruiter, H. R., et al. 2007, A&A, 470, 875

Parma, P., Murgia, M., Morganti, R., et al. 1999, A&A, 344, 7

Plionis, M. & Valdarnini, R. 1991, MNRAS, 249, 46

Proust, D., Quintana, H., Carrasco, E. R., et al. 2006, The Messenger, 124

Quintana, H., Carrasco, E. R., & Reisenegger, A. 2000, AJ, 120, 511

Quintana, H., Melnick, J., Proust, D., & Infante, L. 1997, A&AS, 125

Quintana, H., Ramirez, A., Melnick, J., Raychaudhury, S., & Slezak, E. 1995, AJ, 110, 463

Randall, S. W., Clarke, T. E., Nulsen, P. E. J., et al. 2010, ApJ, 722, 825

Raychaudhury, S. 1989, Nature, 342, 251

Raychaudhury, S., Fabian, A. C., Edge, A. C., Jones, C., & Forman, W. 1991, MNRAS, 248, 101

Reid, A. D., Hunstead, R. W., & Pierre, M. M. 1998, MNRAS, 296, 531

Sakelliou, I. & Merrifield, M. R. 2000, MNRAS, 311, 649

Sarazin, C. L. 1986, X-ray Emission from Clusters of Galaxies (The American Physical Society)

Sarazin, C. L. & Bahcall, J. N. 1977, ApJ, 34, 451

Scaramella, R., Baiesi-Pillastrini, G., Chincarini, G., Vettolani, G., & Zamorani, G. 1989, Nature, 338, 562

Schindler, S. 1996, MNRAS, 280, 309

Shapley, H. 1930, Harward Coll. Obs. Bull, 874, 9

Slee, O. B., Roy, A. L., Murgia, M., Andernach, H., & Ehle, M. 2001, AJ, 122, 1172

Thompson, A. R. 1999, in Synthesis imaging in Radio Astronomy, ed. G. B. Taylor, C. L. Carilli, & R. A. Perley (ASP Conference Series), 11–36

Tully, R. B., Shaya, E. J., & Pierce, M. J. 1992, ApJS, 80, 479

Venturi, T., Bardelli, S., Dallacasa, D., et al. 2003, A&A, 402, 913

Venturi, T., Bardelli, S., Morganti, R., & Hunstead, R. W. 1997, MNRAS, 285, 898

Venturi, T., Bardelli, S., Morganti, R., & Hunstead, R. W. 1998, MNRAS, 298, 1113

Venturi, T., Bardelli, S., Morganti, R., & Hunstead, R. W. 2000, MNRAS, 314, 594

Venturi, T., Bardelli, S., Zambelli, G., Morganti, R., & Hunstead, R. W. 2001, MNRAS, 324, 1131

Venturi, T., Morganti, R., Bardelli, S., Dallacasa, D., & Hunstead, R. W. 1999, in Observational Cosmology: The Development of Galaxy Systems, Vol. 176, 256

Vettolani, G., Chincarini, G., Scaramella, R., & Zamorani, G. 1990, AJ, 99, 1709

Vikhlinin, A., Kravtsov, A., Forman, W., et al. 2006, ApJ, 640, 691

Wellington, K. J., Miley, G. K., & van der Laan, H. 1973, Nature, 244, 502

Zucca, E. & Bardelli, S. 2000, in Constructing the Universe with Clusters of Galaxies

Zucca, E., Zamorani, G., Scaramella, R., & Vettolani, G. 1993, ApJ, 407, 470

Zwicky, F., Herzog, E., Wild, P., Karpowicz, M., & Kowal, C. T. 1961-1968, Catalogue of Galaxies and Clusters of Galaxies